WIRELESS POWER TRANSFER USING OPEN-WIRE TRANSMISSION LINE COUPLING

by

Brian Vaughn

A Dissertation

Submitted to the Faculty of Purdue University

In Partial Fulfillment of the Requirements for the degree of

Doctor of Philosophy

Department of Electrical and Computer Engineering

West Lafayette, Indiana

December 2019

THE PURDUE UNIVERSITY GRADUATE SCHOOL

STATEMENT OF COMMITTEE APPROVAL

Dr. Dimitrios Peroulis, Chair

School of Electrical and Computer Engineering

Dr. Kevin Webb

School of Electrical and Computer Engineering

Dr. David Love

School of Electrical and Computer Engineering

Dr. Micheal Zoltowski

School of Electrical and Computer Engineering

Approved by:

Dr. Dimitrios Peroulis

This thesis is dedicated to my sister, Taryn Vaughn, my mother, Katrina Ray, and to my wife, Sara Vaughn. Thank you for always listening.

ACKNOWLEDGEMENTS

A special thanks to Professor Dimitrios Peroulis, whose guidance and understanding always kept me on track. The author would also like to thank Mark Hickle for his valuable advice and insight.

TABLE OF CONTENTS

LIST OF TABLES

LIST OF FIGURES

ABSTRACT

This dissertation presents and develops a novel method of wireless power transfer that relies on electromagnetic coupling from open-wire transmission lines instead of traditional methods. Wireless power transfer techniques are being rapidly pursued in research currently due to the potential utility of powering devices over the air instead of with direct electrical connections. Uses for such techniques include an array of applications from consumer electronics, to medical devices, to cars and UAVs. While conventional wireless power transfer techniques exist, it is shown here that open-wire transmission line methods present distinct advantages for certain applications. In particular, wireless power transfer using Goubau and twin-lead line architectures will be conceptualized and investigated in terms of their theory, design, and efficiency performance. Further, a circuit model theory will be developed in this work to provide a generalized formulation for open-wire-line wireless power transfer analysis. Additionally, receiver design techniques will be outlined and geometries based on metamaterial principles will be pursued in order to achieve receiver miniaturization and access the applications this affords.

1. INTRODUCTION

1.1 Overview

As of late, wireless power transfer techniques have garnered renewed and vigorous attention [1]-[3]. Such technologies have been shown to lend themselves well, in both execution and concept, to a wide array of applications from vehicle charging to medical implants to consumer electronics and wearables to Internet of Things and 5G [4]-[9] . The reason is simple; without wires, the connective orientational freedom afforded to powering applications increases markedly, especially for applications where power cables are unfeasible and batteries present significant limitations.

As a sub-field of electrical engineering, wireless power transfer is simultaneously very old and very young. In the late 1800's, Nikola Tesla was the first to lay the groundwork for and conceive the possibility of transmitting electric power wirelessly using the principles of electromagnetics [10]. Although his work did not lead to any immediate, widespread commercialization, it would become the basis for many near-field wireless power applications throughout the late 19th and 20th centuries. Additionally, as radio frequency (RF) and microwave techniques developed sufficiently in the mid 1900s, radiation-based WPT methods were introduced, creating a strategy that could allow for wireless power transmission at farther distances than what was possible with near-field structures [11]. It wasn't until 2007, however, when a team at the Massachusetts Institute of Technology revisited Tesla's principles to bring a technique called "highly-resonant coupling" to the forefront that WPT received its current surge of interest [12]. This technique demonstrated the feasibility of transferring power at mid-range (i.e., at a range on the same order of magnitude as 1 meter) non-radiatively.

The three techniques noted above, near-field, far-field, and resonant, make up the bulk of current WPT technologies and will be discussed more deeply in the following section.

1.2 Current Wireless Power Transfer Technologies

1.2.1 Near-Field Techniques

Near field WPT techniques are founded upon the near fields generated by capacitive or inductive elements coupling to other elements of the same type. For the inductive case, high- frequency magnetic fields from inductive coils present upon secondary coils, inducing an EMF via Faraday's law, and thus driving a current in the secondary coils, resulting in power transfer. For the capacitive case, the oscillating electric fields from the primary capacitive element induce charge motion on secondary elements, leading to power transfer in a similar (albeit dual) manner. The magnetic variant is the more adopted method by far due to its larger immunity to interference from surrounding objects, so we will focus on this type primarily [13]. This technique can result in quite high power transfer efficiencies, but only if the primary and secondary elements are very close together and well aligned (on the order of centimeters) [13]-[14]. The reason for this is that the near-field magnitudes falls off as a factor $1/r^2$, where r is the characteristic distance between the primary and secondary elements. This means that the field strength will be too low to facilitate effective power transfer at any distances exceeding a few centimeters. Fig. 1.1 illustrates this effect. When the Tx and Rx coils are placed very close together and are well aligned, the blue flux lines can couple to the receiver optimally and power transfer is high. However, if one of these conditions is not met, transfer efficiency drops dramatically. Because of this, while near-field techniques can indeed be used for high efficiency WPT, they are unsuitable for WPT at-range or across a wide area.

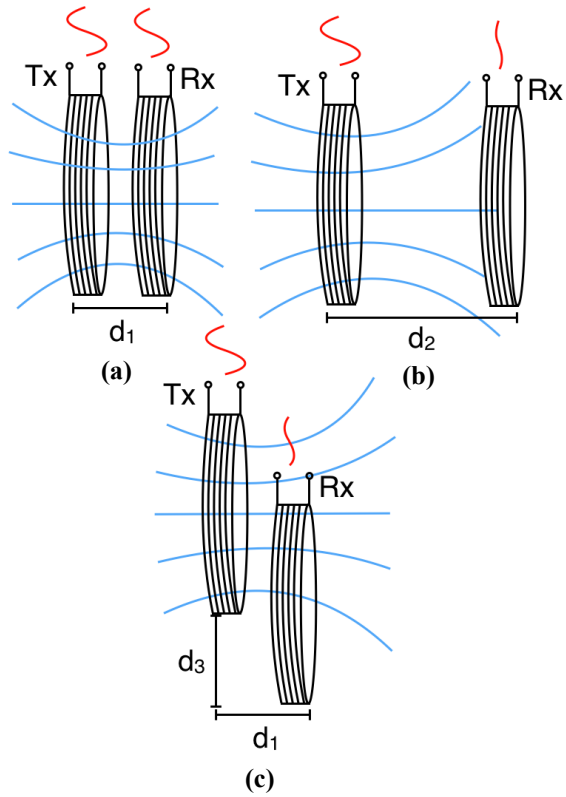

Fig. 1.1: Near-field coil WPT scenarios with (a) the receiver placed optimally placement with high power transfer, (b) the receiver placed too far away with low power transfer, and (c) the receiver misaligned with low power transfer.

1.2.2 Far-Field Techniques

The far-field WPT technique differs from the near-field method in that it does not involve the direct electromagnetic coupling of energy. In the near-field implementations, assuming loss-less cases, energy will not leave the source circuit unless there is a receiver to capture it. On the other hand, the far-field WPT technique transmits electromagnetic energy into space radiatively (usually with the use of a high-gain, directional antenna or an array), which is then captured by some receiving structure. This method has been in active research for the past several decades and is a primary long-distance candidate for beaming high levels of power or creating energy-harvesting networks for low-power electronics [15]-[16]. The advantage of this technique is that, as opposed to the near field case, the field magnitudes of far-fields fall-off as $1/r$ instead of $1/r^2$, meaning power can be transferred at much larger distances. This comes at a cost, however, in the form of the inverse square law, which manifests as a weakening power density as a function of the distance from the transmitter structure and leads to radiative path-loss [17]. While an inverse

relationship between distance and power transfer is to be expected, any power lost during radiative transmission is unrecoverable. Furthermore, using transmitter and receiver gain to overcome path-loss results in large antenna structures that cannot be applied to small electronics systems, and the required directionality lowers the locational freedom of the receiver [16]. Increasing the frequency alleviates the size issue, but exacerbates the path-loss at the same time. Fig. 1.2 shows a diagram of a far-field WPT and highlights that while energy can reach a far distance, much of it is lost on the way. Because of this, for applications requiring a larger area of effect for power transfer without substantial radiation loss, more appropriate techniques should be sought.

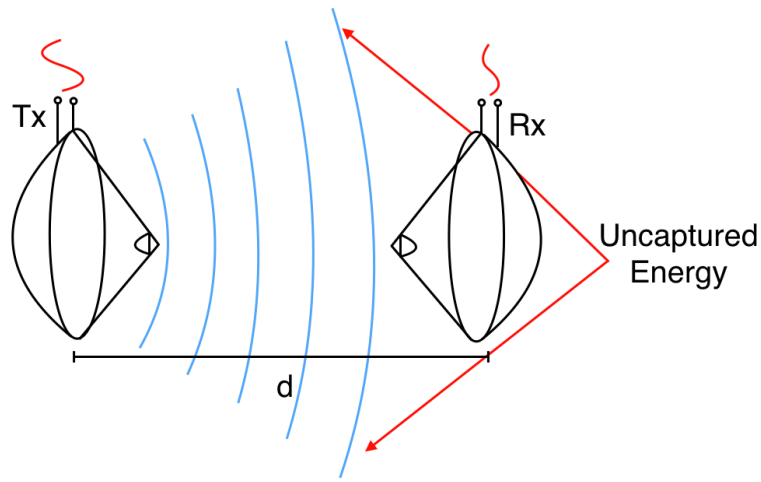

Fig. 1.2: Far-field WPT configuration with radiation loss noted.

1.2.3 Resonant Near-Field Techniques

Although the resonant near-field technique was originally developed by Nikola Tesla in the late 1800s, the method was not adopted by the WPT community at large until it was popularized by a team at MIT in 2007, who showed a system utilizing the technique that could power a lightbulb wirelessly from more than a meter away [10], [12]. This sparked a new era in WPT, where the coupling between transmitter and receiver circuits was enhanced by designing these structures to be resonators to move the technology into the mid-range (on the order of a meter). The inclusion of resonant elements in such systems serves to extend their range considerably, as the evanescent near-field energy can tunnel much farther distances under this circumstance. Indeed, this range extension is advantageous for mid-range WPT applications, but it comes with a signif-

icant drawback; the transmitter and receiver resonant frequencies must be tuned with a very high degree of precision for the technique to be effective. Furthermore, the resonator structures must be low-loss (high-Q) to facilitate efficient power transfer [12]. While systems with these quality factors and frequency precision can be created in a laboratory environment, the requirements this method dictates for farther transfer distances limit the mass production efficacy of the technique. In Fig. 1.3, several resonant WPT scenarios (where the resonators are created by connecting coils to parallel capacitors) are shown. Here, ω_1 and ω_2 are the resonant frequencies of the Tx and Rx resonators respectively. Note that the transfer efficiency can be high even though the transmitter-receiver distance is equal to d_2 from figure 1.1. However, In two scenarios, either the frequency or quality-factor qualification is not met and power transfer is compromised in the mid-range. Given this, it would be advantageous to develop a method with more lax design tolerances to account for the lack of flexibility the resonant near field technique presents.

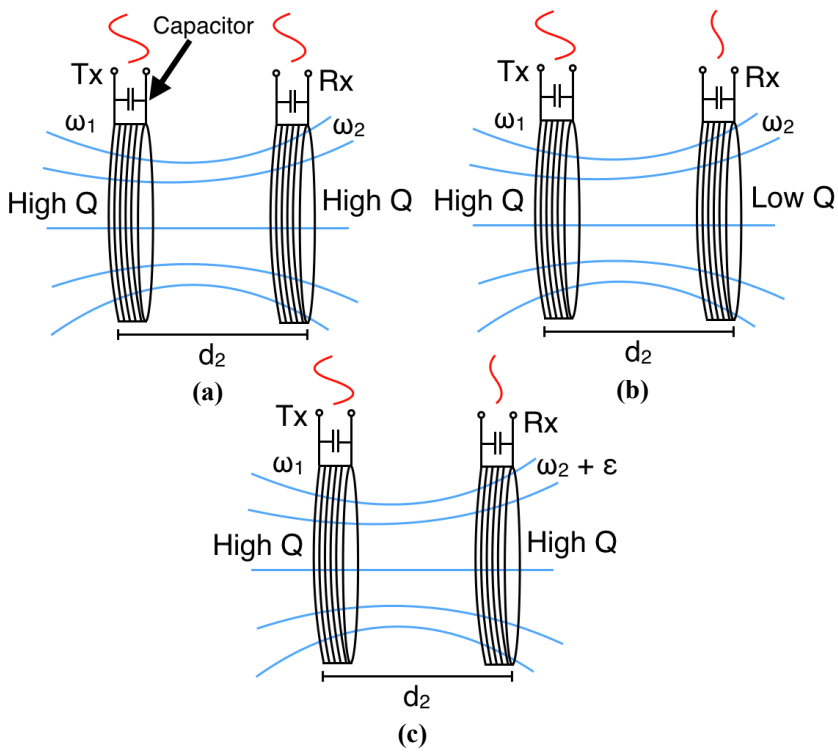

Fig. 1.3: Resonant coil WPT scenarios with (a) the receiver placed in the mid-range with optimal Q and tuning with high power transfer, (b) a lossy receiver low power transfer, and (c) a detuned receiver with low power transfer.

1.3 Open-Wire-Based Waveguide Structures

In the previous sections, the currently most-used WPT techniques were laid out and discussed. Here, we invoke a structure that has utility for WPT applications not presented by the methods above. This structure is the open-wire waveguide. In most transmission line structures, two or more conducting surfaces are placed in close proximity, and in the case of some line types, the signal path is shielded (e.g. coaxial, stripline, etc.) to prevent radiation loss. For open-wire structures, however, the lines consist of some unshielded configuration of wires suspended in space. The number of wires required to create such a line can be as low as one (this is the Goubau Line, to be discussed below). The reason such lines deserve attention as far as wireless power transfer is concerned is because, since the lines are unshielded, their fields extend to infinity (whether there is radiation or not). Furthermore, the field distributions of some of these lines are unique in that they can allow us to circumvent the limitations of near and far fields. These facts make open-wire structures candidates for WPT applications. Below, two classes of open-wire lines will be discussed.

1.3.1 Single-Wire Goubau Line

In 1899, Sommerfeld discovered a solution to the wave equation for the case of a single cylinder with finite conductivity and infinite length suspended in free space. What he found was that the geometry supports a propagating TM mode surface-wave with no cutoff frequency. In such a structure, the ground plane is effectively placed at infinity, meaning no physical current runs along the line since it has no return path (hence the term, “surface-wave”). In 1950, George Goubau expanded upon this derivation to conceptualize a design process for a transmission line utilizing only one wire [18]-[19]. This type of transmission line has been commonly named the Goubau line (GLine) as a result. As it turns out, this type of line lends itself to WPT applications. In particular, the field distribution of the GLine has been determined to have attractive qualities regarding WPT. These fields are presented below:

$$E_r = jA_i \frac{h}{\gamma_i} Z_1(\gamma_i r) e^{j(\omega t - hz)}, \tag{1.1a}$$

$$E_z = A_i Z_0(\gamma_i r) e^{j(\omega t - hz)}, \tag{1.1b}$$

$$H_\varphi = jA_i \frac{{k_i}^2}{\omega \mu \gamma_i} Z_1(\gamma_i r) e^{j(\omega t - hz)}, \tag{1.1c}$$

where A_i is the wave amplitude, h is the longitudinal propagation constant, k_i is the medium-dependent wavenumber, ω is the angular frequency, μ is the permeability, γ is a characteristic parameter defined as

$$\gamma_i = k_i^2 - h^2 \tag{1.2}$$

and the Z_0 terms are the cylindrical functions that describe the field radially (Bessel functions of the first kind inside the conductor and Hankel functions of the first kind outside it) [19]. In Fig. 1.4, these fields are visualized for a single-conductor geometry supporting fields propagating in the z-direction.

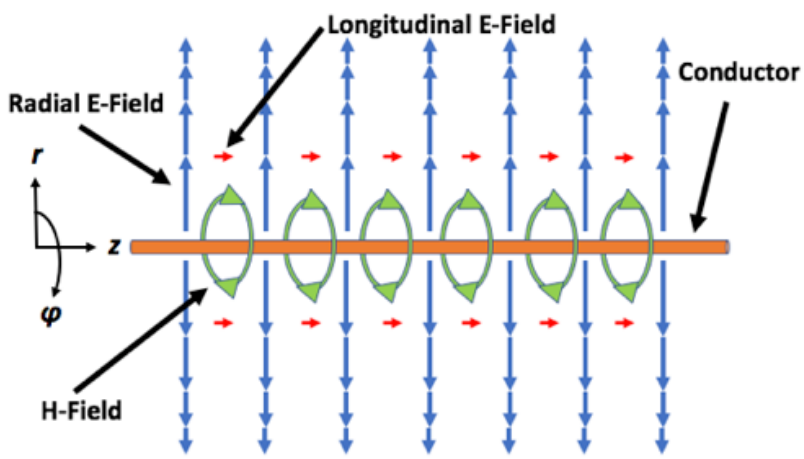

Fig. 1.4: GLine field distribution visualization.

While not obvious from inspection, two significant qualities of the GLine fields are evident from analysis. First of all, by taking the cross product of the E and H-fields outside the conductor, we may derive the Poynting vector, which is shown below:

$$\tilde{S} = E \times H^* = \frac{|A_o|^2 h k_o{}^2}{\omega\mu|\gamma_o|^2} |H_1(\gamma_o r)|^2 e^{2Im(h)z} \hat{z} + \frac{-j|A_o|^2 k_o{}^2}{\omega\mu\gamma_o{}^*} H_0(\gamma_o r) H_1(\gamma_o r)^* e^{2Im(h)z} \hat{r} \tag{1.3}$$

If this expression is evaluated numerically, it becomes apparent that the real part of the Poynting vector's z-component is far greater than the real part of the vector's r-component, i.e.,

$$\mathrm{Re}(\tilde{S}_z) >> \mathrm{Re}(\tilde{S}_r) \tag{1.4}$$

In fact, the z-component exceeds the r-component by many orders of magnitude when evaluated numerically and it disappears with distance (this will be elaborated on in Chapter 3). Therefore, although the line consists of only a single conductor that is unshielded, radiation is negligible for this line. This is supported by Maxwell's equations as well as intuition. From an intuitive stand-point, since there is no return path for current given that the "ground plane" is at infinity for the single wire line, no real current can flow. This is proven by Ampere's law, which only holds for the field distribution presented above if the real current within the conductor is zero. If there is no real current, then there is no radiation. This is the first significant quality of the GLine. The second is evident from an analytical analysis of the field variation with respect to radial distance from the center conductor (see Chapter 3 for more details). By examining the field variation with r in the regions of interest, it can be shown that the rate at which the field amplitudes decay with distance from the center conductor is $1/r$. This means that the GLine fields' radial fall-off rate is almost identical to that of radiative far-fields, which are also functions of $1/r$.

To summarize, the fields of the GLine do not radiate in the radial direction, but the field magnitudes decrease with distance at approximately the same rate as far-fields do, meaning that the GLine fields have the best qualities of both near-fields and far-fields without their drawbacks. Note, further, that these qualities are present without any resonant action along the waveguide. Because of this, the GLine serves as an acceptable candidate for WPT structures.

1.3.2 Twin-Lead Line

The twin lead transmission line is a well documented line topology, generally used for applications that favor balanced lines with high characteristic impedance [20]. While the general design of such lines is geared toward containing field energy as close to the line wires as possible, they may be designed such that their fields can reach farther away for coupling applications. A theoretical representation of the twin lead fields is described in eqn. 11.5.12 of [20] and a visualization of the fields propagating in the z-direction is shown in Fig. 1.5. While not obvious by inspection, the rate at which the fields fall off with distance from the wires is inversely proportional to the wire separation distance. However, this creates a trade-off, as increasing the wire separation too much leads to radiation loss and a breakdown of the theory (since the theoretical fields assume a quasi-static scenario, which is an invalid assumption if the wires are too far apart). Nevertheless, given the simplicity of this line and its implementation, along with the large length-wise coupling area it can provide, the twin-lead line is also a good candidate for transmission line WPT applications.

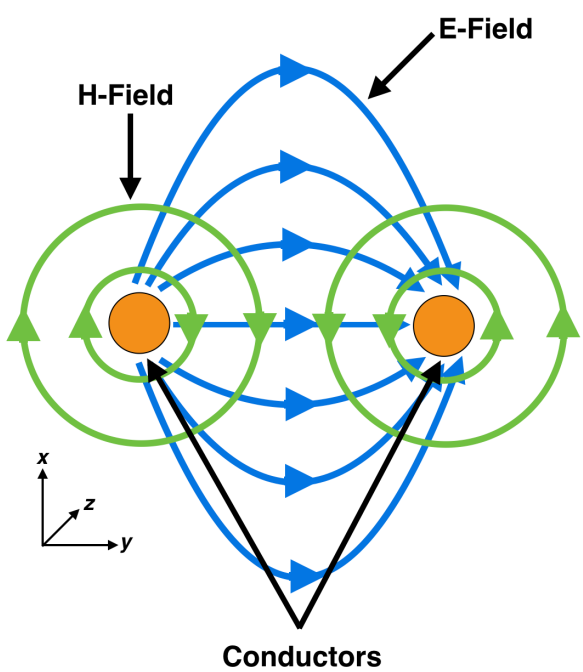

Fig. 1.5: Twin-lead field distribution visualization.

1.4 Wireless Power Transfer Considerations to be Addressed

Throughout this work, the open-wire lines (OWLs) of the previous section will be shown to address several key considerations in the WPT sphere. In particular, they present the following advantages when compared to the alternative techniques discussed thus far:

Advantages Over Near-Field Techniques

- There exist OWL field distributions that do not fall off in magnitude as $1/r^2$ like near-field distributions.
- OWLs can function in both the near and mid-range.
- OWL geometries lend themselves to area-of-effect (AoE) applications whereas near-field techniques are limited in terms of receiver position and orientation.

Advantages Over Far-Field Techniques

- OWL usable power is maximized since radiation loss is not inherent to the technique.
- Highly-directional field distributions are not required for OWLs.
- OWLs present potential for high-power applications without massive Tx and Rx structures.

Advantages Over Resonant Near-Field Techniques

- OWL techniques are not based on stringent resonant tuning.
- Q and frequency requirements are significantly more lax for OWLs.

Given these considerations, we may summarize the applications in which OWL techniques are more appropriate than the others discussed above:

Applications Where OWL Structures are Appropriate

- All near and mid-range applications that require an AoE.
- Applications that favor design flexibility and higher tolerances.
- Applications that demand modularity.
- Applications that favor design ubiquity.

Furthermore, and perhaps most importantly, the OWL systems described herein will be shown to support power transfer efficiencies high enough to make them competitive choices for the types of applications listed above. Because of this, it is clear that OWL structures deserve attention for the the roles they can play in WPT applications.

In the next chapter, the circuit theory of OWL WPT will be conceptualized in order to create a viable model for such systems.

2. OPEN-WIRE LINE WIRELESS POWER CIRCUIT MODEL

In order to conceptualize the design of an OWL WPT system, an appropriate circuit model should be created. This model must include an intuitive and useful interpretation of the OWL coupling mechanism and it must be usable to compute system characteristics such as input impedance and efficiency using measurable quantities. To do this, coupling circuit theory will be combined with the transmission line lumped-element model to derive an effective equivalent circuit. To begin, basic electric and magnetic coupling circuits will be summed-up and then they will be integrated into the lumped element model.

2.1 Electric and Magnetic Coupling Circuits

The coupling mechanisms between electromagnetic elements may be described in terms of either electric or magnetic coupling. Electric coupling occurs between capacitive elements and magnetic coupling occurs between inductive elements. We may model such couplings in terms of coupled capacitors and inductors. It should be noted that mixed coupling is also possible, wherein couplings between capacitive and inductive elements occur simultaneously, but we will not focus on this case in this work. Below, circuit models for coupled capacitances and inductances are shown:

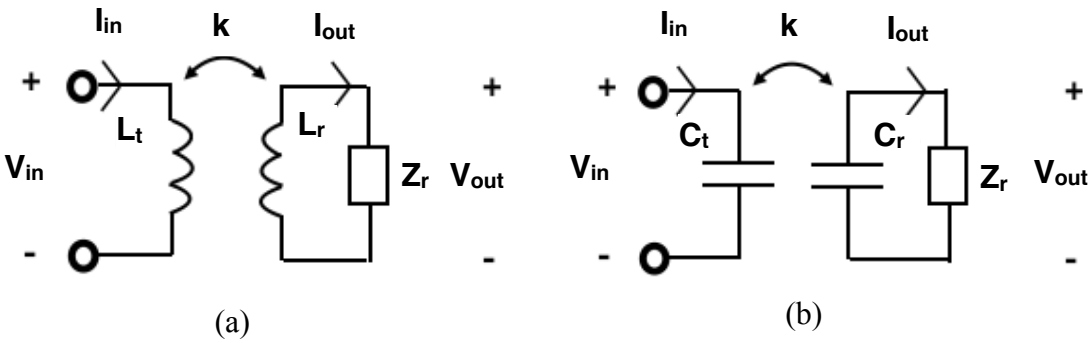

Fig. 2.1: (a) Inductive coupling circuit and (b) capacitive coupling circuit.

Notice that the diagrams above depict a parameter called "*k*". This parameter denotes the coupling strength between the coupled elements. With the circuits above, we may define the voltage and current relationships between the coupled elements using the following equations:

$$V_{out\_L} = I_{out\_L} Z_r \tag{2.1a}$$

$$I_{out\_L} = \frac{j\omega k\sqrt{L_r L_t}}{j\omega L_r + Z_r} I_{in} \tag{2.1b}$$

$$V_{out\_C} = \frac{-j\omega k\sqrt{C_r C_t}}{j\omega C_r + 1/Z_r} V_{in} \tag{2.1c}$$

$$I_{out\_C} = \frac{V_{out\_C}}{Z_r} \tag{2.1d}$$

Further detail may be found in [21]. With these relations, in can be shown that the input impedance Z_{in} for each circuit can be expressed as

$$Z_{in\_L} = j\omega L_t + \frac{\omega^2 k^2 L_r L_t}{j\omega L_r + Z_r} \tag{2.2a}$$

$$Z_{in\_C} = \left(j\omega C_t + \frac{\omega^2 k^2 C_r C_t}{j\omega C_r + 1/Z_r}\right)^{-1} \tag{2.2b}$$

Further, the power delivered to the output side of each circuit is

$$P_{out\_L} = \frac{1}{2} Re\left(\left|\frac{j\omega k\sqrt{L_r L_t}}{Z_r + j\omega L_r}\right|^2 Z_r^*\right) \tag{2.3a}$$

$$P_{out\_C} = \frac{1}{2} Re\left(\frac{\left|\frac{-j\omega k\sqrt{C_r C_t}}{j\omega C_r + 1/Z_r} V_{in}\right|^2}{Z_r^*}\right) \tag{2.3b}$$

This shows, as expected, that the power is directly proportional to the coupling strength. The impedance-matching requirements will be discussed further in later sections. In the next section, the coupling theory above will be applied to transmission lines to complete the OWL WPT circuit model.

2.2 Open-Wire Line Equivalent Circuit

To start, we will invoke the lumped element model for a standard transmission line as shown below:

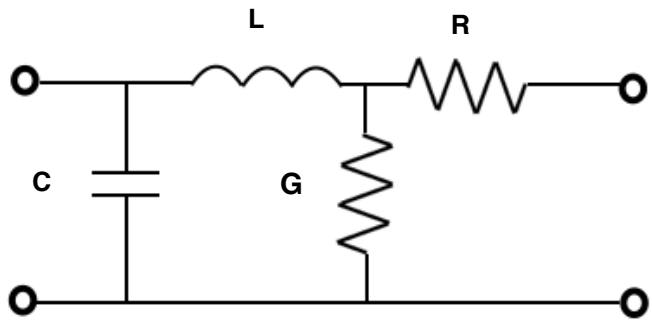

Fig. 2.2: Transmission line lumped element model.

In the above figure, the transmission line is modeled as a chain of inductances, capacitances, resistances, and conductances [22]. The parameters of the transmission line (the characteristic impedance Zo, the propagation constant γ, etc.) are defined in terms of these element values per unit meter. The values in question may be derived by examining the field distribution of the transmission line being analyzed. The most important elements for our purposes are the capacitances and inductances, as they provide an avenue for electromagnetic coupling. Specifically, referring the Fig. 2.1, the coupled elements on the LHS of the coupling circuits will come from the transmission line's intrinsic capacitance or inductance. In other words, when coupling transmission line (TLine) energy to an external circuit, the input side reactive element may be modeled as a portion of the TLine's capacitance or inductance. With this in mind, we may define the circuits for electric and magnetic OWL coupling as below.

2.2.1 Electric Coupling

Below, the full model of an OWL WPT system is given for the electric coupling case. The line is terminated with an arbitrary impedance Zterm and the line length is the sum of the electrical lengths θ1 and θ2. The receiver circuit is made up of a series combination of lumped elements tied to a receiver termination. This receiver model is valid for electrically short antennas, which will be used for reasons discussed in proceeding chapters. Finally, the coupling is accom-

plished by linking the receiver capacitance of the receiver to an effective transmission line capacitance C_t, which will be found using techniques discussed below.

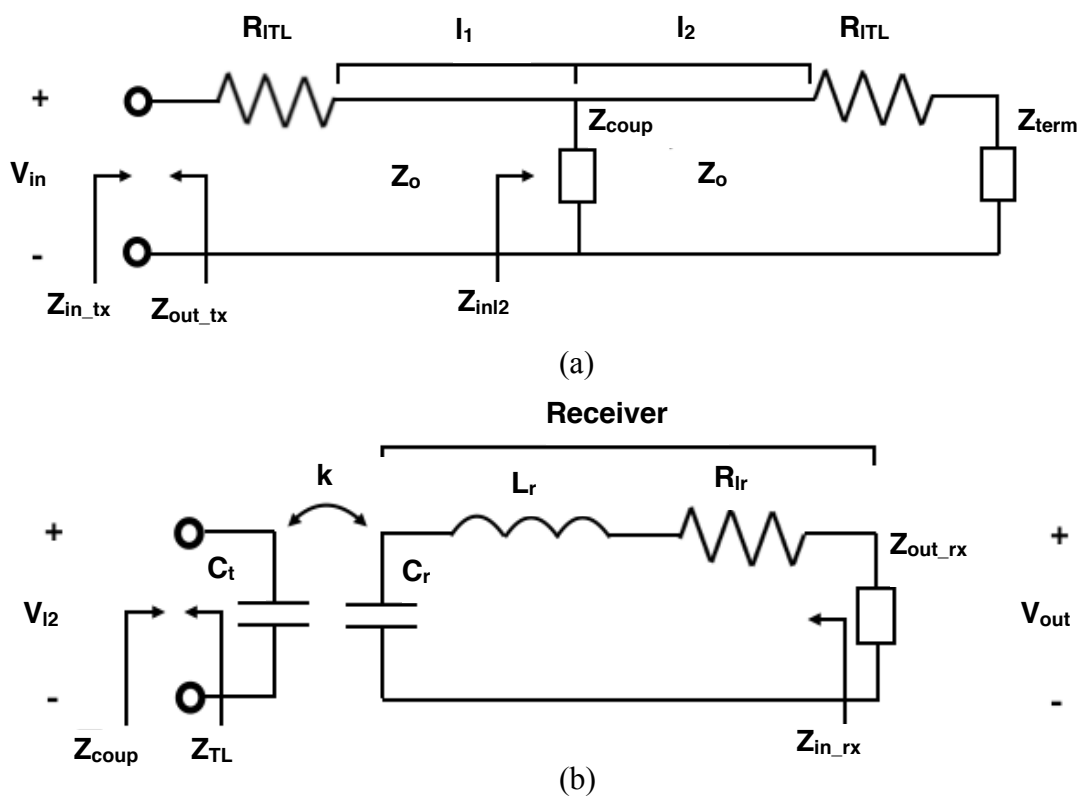

Fig. 2.3: (a) Electrically-coupled OWL WPT circuit model and (b) receiver equivalent coupling circuit.

Note that Z_{inl2} is an intermediate impedance used to simplify the circuit solution. Further, R_{lt} are loss parameters used to quantify the loss associated with feeding and terminating OWLs that have a usable coupling area. This mechanism will be discussed in more detail in the chapters pertaining to specific OWL architectures, but it is true that these losses are prevalent enough to be used in the general model. Using these parameters, the coupling circuit theory shown in the previous section, and transmission line circuit theory (assuming a lossless line), it can be shown that the input impedance looking into Port 1 of the line may be expressed as

where

$$Z_{in\_tx} = R_{lt} + Z_0 \left[\frac{Z_{inl2} + jZ_0 \tan \beta l_1}{Z_0 + jZ_{inl2} \tan \beta l_1}\right] \tag{2.4}$$

$$Z_{inl2} = \left[\left(Z_{coup}\right)^{-1} + \left\{ Z_0 \left[\frac{Z_{term} + R_{lt} + jZ_0 \tan \beta l_2}{Z_0 + j(Z_{term} + R_{lt}) \tan \beta l_2} \right] \right\}^{-1} \right]^{-1} \tag{2.5}$$

$$Z_{coup} = \left(j\omega C_t + \frac{\omega^2 k^2 C_r C_t}{j\omega C_r + Y_R} \right)^{-1} \tag{2.6}$$

$$Z_R = Z_{out\_rx} + j\omega L_r + R_{loss} \tag{2.7}$$

$$Y_R = \frac{1}{Z_R} \tag{2.8}$$

To take it a step further, we may invoke the TEM voltage and current solutions to Telegrapher's Equations to find the voltage across the capacitance C_t in terms of the voltage at the transmission line input as,

$$V_{l2} = \frac{(Z_{in\_tx} - R_{lt})(1 + \Gamma)V_{in}}{Z_{in\_tx}(e^{-j\beta l_1} + \Gamma e^{j\beta l_1})} \tag{2.9}$$

where

$$\Gamma = \frac{Z_{inl2} - Z_0}{Z_{inl2} + Z_0} \tag{2.10}$$

Using the coupling theory from Section 2.1, we may then derive the voltage across the receiver load as

$$V_{out} = \frac{Z_{out\_rx}(-j\omega k\sqrt{C_r C_t})V_{l2}}{Z_R(Y_R + j\omega C_r)} \tag{2.11}$$

With these expressions, we may find the power efficiency of the system by evaluating the following equation.

$$\eta = \frac{Re\left[\frac{|V_{out}|^2}{Z^*_{out\_rx}}\right]}{Re\left[\frac{|V_{in}|^2}{Z^*_{in\_tx}}\right]} = \frac{Re(Y^*_{out\_rx})}{Re(Y^*_{in\_tx})}\left|\frac{V_{out}}{V_{in}}\right|^2 \tag{2.12}$$

This allows us to define the efficiency of the system in terms of the coupling dynamics of the system. However, while most of the circuit parameters can be obtained through simple measurement, C_t, and k are less straightforward. To find these values, we will derive the system's Z-parameters, Specifically Z_{11} and Z_{21}. Both of these values may be derived by repeating the above analysis while treating Z_{out} as an open circuit. Doing this yields the following equations:

$$Z_{11} = R_{lt} + Z_0\left[\frac{Z'_{inl2} + jZ_0 \tan \beta l_1}{Z_0 + jZ'_{inl2} \tan \beta l_1}\right] \tag{2.13}$$

$$Z_{21} = -k\sqrt{\frac{C_t}{C_r}}\left[\frac{(1+\Gamma')(Z_{11} - R_{lt})}{(e^{-j\beta l_1} + \Gamma' e^{j\beta l_1})}\right] \tag{2.14}$$

where

$$Z'_{inl2} = \left[j\omega C_t(1-k^2) + \left\{Z_0\left[\frac{Z_{term} + R_{lt} + jZ_0 \tan \beta l_2}{Z_0 + j(Z_{term}+R_{lt}) \tan \beta l_2}\right]\right\}^{-1}\right]^{-1} \tag{2.15}$$

$$\Gamma' = \frac{Z'_{inl2} - Z_0}{Z'_{inl2} + Z_0} \tag{2.16}$$

For any 2-port network, these values may be obtained through measurement, leading to a system of two equations and two unknowns, which may be solved numerically in general, and analytically for special cases (as will be shown in Chapter 4). With this, the formulation for electric coupling is complete. In the next section, the process will be repeated for the magnetic coupling case.

2.2.2 Magnetic Coupling.

We may establish a model similar to the one shown in Fig. 2.3 for the magnetic case by substituting the TLine capacitive coupling for inductive coupling. This is shown in the figure below assuming an electrically-short magnetic receiver:

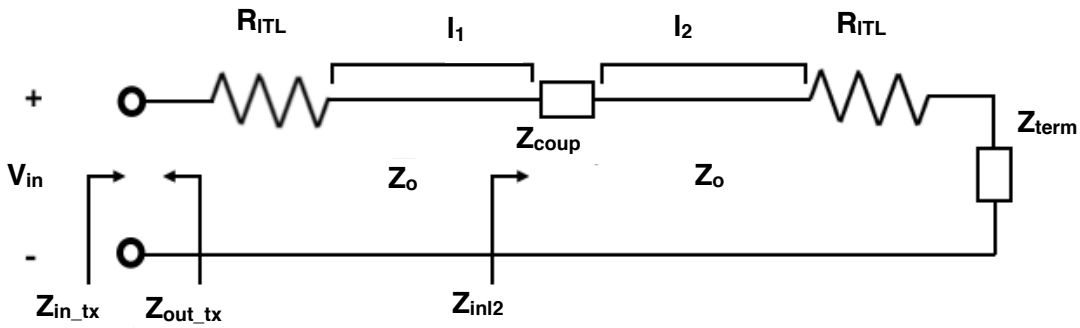

(a)

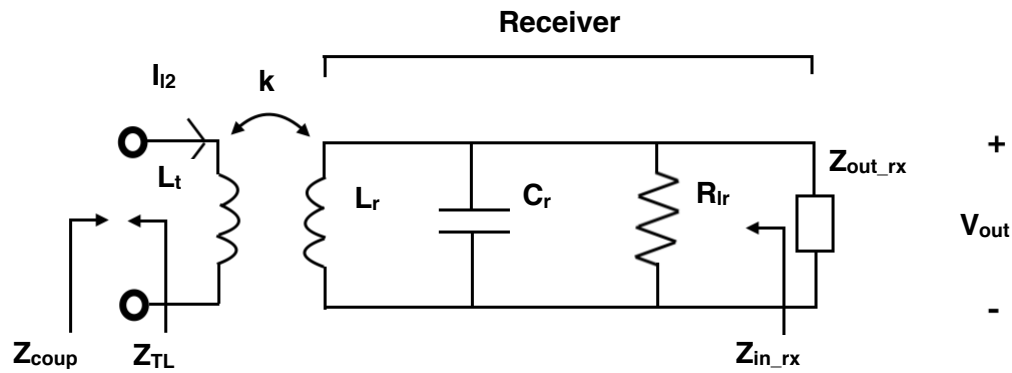

(b)

Fig. 2.4: (a) Magnetically-coupled OWL WPT circuit model and (b) receiver equivalent coupling circuit.

As before, we may derive the circuit input impedance using magnetic coupling and transmission line theory to obtain the following expression:

$$Z_{in\_tx} = R_{lt} + Z_0 \left[\frac{Z_{inl2} + jZ_0 \tan \beta l_1}{Z_0 + jZ_{inl2} \tan \beta l_1}\right] \tag{2.17}$$

where

$$Z_{coup} = j\omega L_t + \frac{\omega^2 k^2 L_r L_t}{j\omega L_r + Z_R} \tag{2.18}$$

$$Z_{inl2} = Z_{coup} + Z_0 \left[\frac{Z_{term} + R_{lt} + jZ_0 \tan \beta l_2}{Z_0 + j(Z_{term} + R_{lt}) \tan \beta l_2}\right] \tag{2.19}$$

$$Y_R = (Z_{out\_rx})^{-1} + j\omega C_r + (R_{loss})^{-1} \tag{2.20}$$

$$Z_R = \frac{1}{Y_R} \tag{2.21}$$

Proceeding along the same lines as the electric case analysis, the current presented across the terminals of L_t is given as

$$I_{l2} = \frac{(Z_{in\_tx} - R_{lt})(1 - \Gamma)V_{in}}{Z_{in\_tx}(e^{-j\beta l_1} + \Gamma e^{j\beta l_1})} \tag{2.22}$$

Γ is the same as in eqn 2.10. Using the current relationship between the coupled inductances, we may derive the output voltage in terms of the input voltage to be.

$$V_{out} = \frac{j\omega k\sqrt{L_r L_t} I_{l2}}{1 + j\omega L_r Y_R} \tag{2.23}$$

The efficiency of the system may be evaluated using eqn. 2.12. As before, we derive the circuit Z-parameters in order to be able to solve for L_t and k:

$$Z_{11} = R_{lt} + Z_0 \left[\frac{Z'_{inl2} + jZ_0 \tan \beta l_1}{Z_0 + jZ'_{inl2} \tan \beta l_1}\right] \tag{2.24a}$$

$$Z_{21} = \frac{j\omega k\sqrt{L_r L_t}}{1 + j\omega L_r (j\omega C_r + (R_{lr})^{-1})} \frac{(1 - \Gamma')(Z_{11} - R_{lt})}{(e^{-j\beta l_1} + \Gamma' e^{j\beta l_1})} \tag{2.24b}$$

where

$$Z'_{inl2} = j\omega L_t + \frac{\omega^2 k^2 L_r L_t}{j\omega L_r + (j\omega C_r + (R_{lr})^{-1})^{-1}} + Z_0 \left[\frac{Z_{term} + R_{lt} + jZ_0 \tan \beta l_2}{Z_0 + j(Z_{term} + R_{lt}) \tan \beta l_2}\right] \tag{2.25}$$

$$\Gamma' = \frac{Z'_{inl2} - Z_0}{Z'_{inl2} + Z_0} \tag{2.26}$$

With this, the magnetic coupling OWL WPT circuit model is concluded.

2.3 Receiver Parameters

In the sections above, it was stated that all the model parameters are know except for C_t, L_t, and k. However, C_r, L_r, and R_{lr} also deserve discussion. These are treated as knowns above, but must be measured from the receiver structures standalone input impedance (when not coupled to anything). For an electrically-short receiver, C_r or L_r may be inferred by noting the structure's reactance X or susceptance B at the frequency of operation ω, as well as the frequency ω_o where the reactance is 0 (i.e. the receiver's resonant frequency). With this information, using circuit theory, we can deduce that C_r or L_r may be found as

$$C_r = \frac{\omega^2 - {\omega_o}^2}{X\omega{\omega_o}^2}, \tag{2.27a}$$

$$L_r = \frac{\omega^2 - {\omega_o}^2}{B\omega{\omega_o}^2} \tag{2.27b}$$

L_r, then, is simply found using the relationship between C_r, L_r, and ω_o:

$$\omega_o = \frac{1}{\sqrt{C_r L_r}} \tag{2.28}$$

R_{lr} is simply the real part of the receiver impedance or the inverse of the real part of the receiver admittance at the operation frequency. Now that the receiver parameters have been established,

we may turn our attention to impedance matching considerations, which will be discussed in the next section.

2.4 Impedance Matching

From eqn 2.12, it can be seen by inspection that the efficiency values are strong functions of the output termination impedance of the receiver. This implies that from a matching perspective (assuming 50 Ω systems), there is an optimal matching scheme at both the circuit input and output to facilitate maximum power transfer. It would seem that the best strategy would be to use a conjugate matching scheme, as this is proven to yield maximum power transfer in conventional circuits. However, this is difficult to implement for this two port system, as the impedance looking into one port is dependent on the impedance looking into the other and vice versa, meaning the impedances must be formulated simultaneously. To get around this, once the Z-parameters are known, we may use numerical optimization techniques to calculate the impedance each port needs to see in order to maximize power transfer or compute the optimal conjugate match using the process detailed in [23]. In this work, we will choose the former option, as it allows us to place constraints on the available matching conditions and find an optimal match under those conditions. We will carry out this process using MATLAB, as well as the relationship between Z-parameters and S-parameters, which are given below [24]:

$$S_{11} = \frac{(Z_{11} - Z_{01}^{*})(Z_{22} + Z_{02}) - Z_{12}Z_{21}}{(Z_{11} + Z_{01})(Z_{22} + Z_{02}) - Z_{12}Z_{21}} \tag{2.29a}$$

$$S_{21} = \frac{2Z_{21}(R_{01}R_{02})^{1/2}}{(Z_{11} + Z_{01})(Z_{22} + Z_{02}) - Z_{12}Z_{21}} \tag{2.29b}$$

The algorithm employed in this work is a systematic search scheme in which every impedance combination of Z_{o1} and Z_{o2} within a specified range is evaluated and the optimal combination is selected and listed as an output. Alternatively, eqn. 2.12 may be used in the algorithm once the Ct and k parameters are deduced to obtain the same results. Since both ports of the circuit are associated with an impedance that is not 50 Ω, we will refer to the matching of this case as "two-sided" matching. This is not the only strategy that can be used, however. A "one-sided" matching

scheme wherein the receiver port is terminated with a set load may also be employed. In this case, the input impedance would be computed from eqn. 2.4 or 2.17 and this impedance would be used for matching. However, this scheme is not optimal for lossless matching networks; the optimal efficiency using a two-sided scheme will always be higher than the optimal efficiency of a one-sided scheme in the matching network has no losses. One the other hand, if matching network loss is introduced in both the input and output matching networks, a one-sided match may become preferable under certain conditions. In the next section, these conditions will be investigated.

2.5 One-Sided vs. Two-Sided Matching

Consider the coupled inductor circuit below:

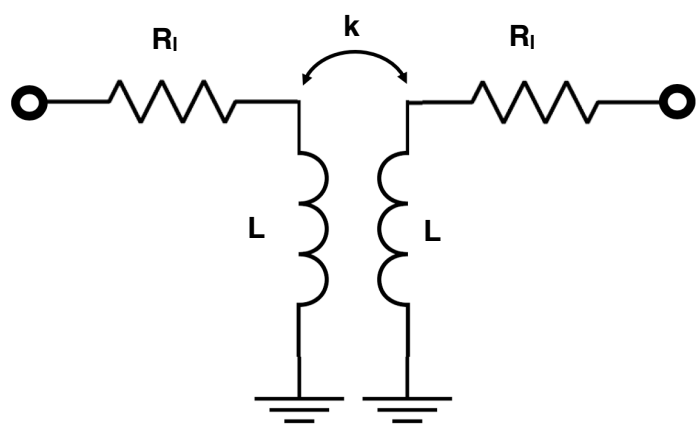

Fig. 2.5: Generic coupled inductor circuit.

Notice that there are resistors added to account for loss mechanisms in the circuit. For this system, let the reactance X and quality factor Q of each inductive element be defined as

$$X = \omega L \tag{2.30}$$

$$Q = \frac{X}{R_l} \tag{2.31}$$

Using the techniques discussed in the previous section (specifically the analysis in Section 2.1 and the MATLAB algorithm), we may compute the optimal Z_{o1} and Z_{o2} values for a two-sided matching scenario. We may also terminate the circuit with a set load and determine the resultant efficiency to obtain one-sided matching data. Under the assumption that a two-sided matching scheme requires two matching networks and a one-sided scheme only requires one, we can express the total efficiency for each scheme as follows:

$$\eta_{1\_side\_tot} = \eta_{IM}\eta_{1\_side} \tag{2.32a}$$

$$\eta_{2\_side\_tot} = \eta_{IM}^{2}\eta_{2\_side} \tag{2.32b}$$

Here, η_{1_side} and η_{2_side} are computed using eqns 2.3a and 2.12 with the respective matching conditions and η_{IM} is an arbitrary matching network efficiency value. To clarify, the equations above indicate that a one-sided match only needs to absorb the loss of a matching network at the input, whereas a two-sided match has to do so at both the input and output. For all possible iterations of the coupling circuit shown in Fig. 2.5, there is a η_{IM} value that will make $\eta_{1\_side\_tot}$ equal to $\eta_{2\_side\_tot}$. If η_{IM} is less than this "threshold" value, the one-sided match efficiency overtakes the efficiency advantage given by using a two-sided match. To illuminate this point, the η_{IM} threshold value is plotted below for different values of X, Q, and one-sided termination impedance Z_{out} (if a one-sided match is used, we may choose the value of Z_{out} and this affects where the threshold is):

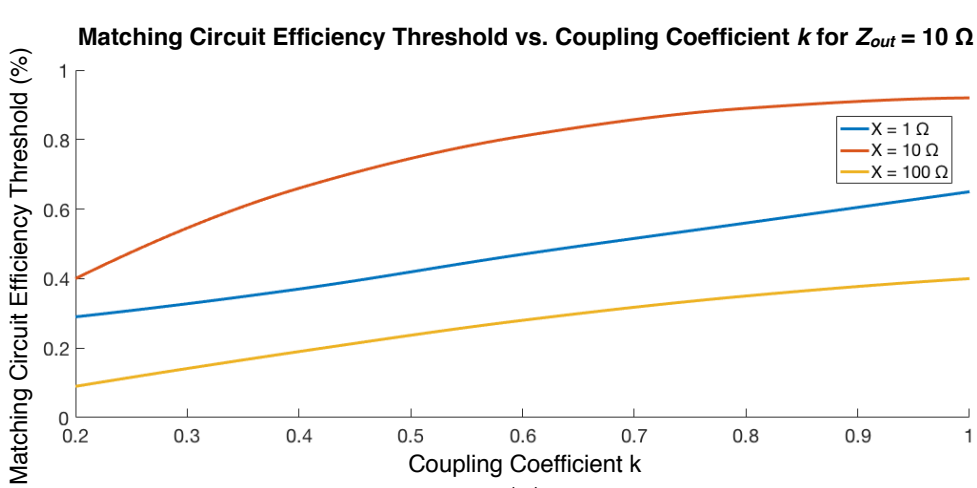

(a)

Fig. 2.6: Q = 10 matching circuit threshold efficiency as a function of coupling coefficient for (a) Z_{out} = 10 Ω, (b) Z_{out} = 50 Ω, (c) Z_{out} = 100 Ω, and (d) Z_{out} = 1000 Ω.

Fig. 2.6 continued

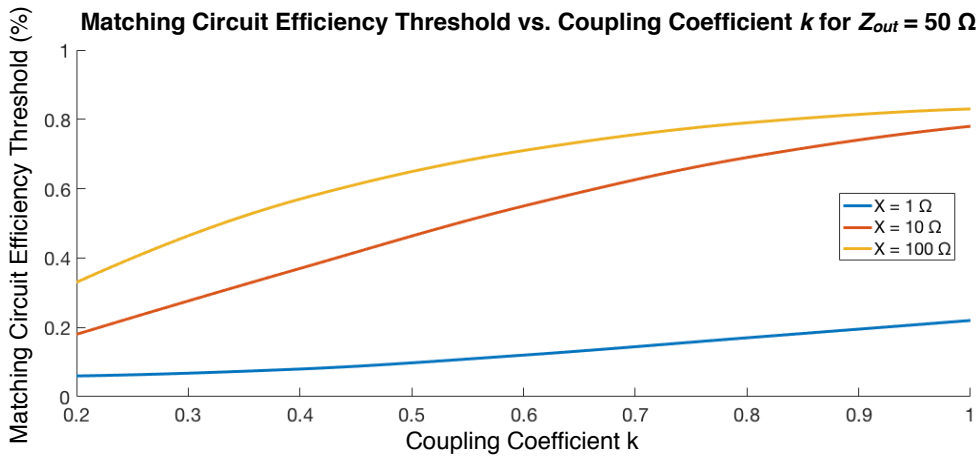

(b)

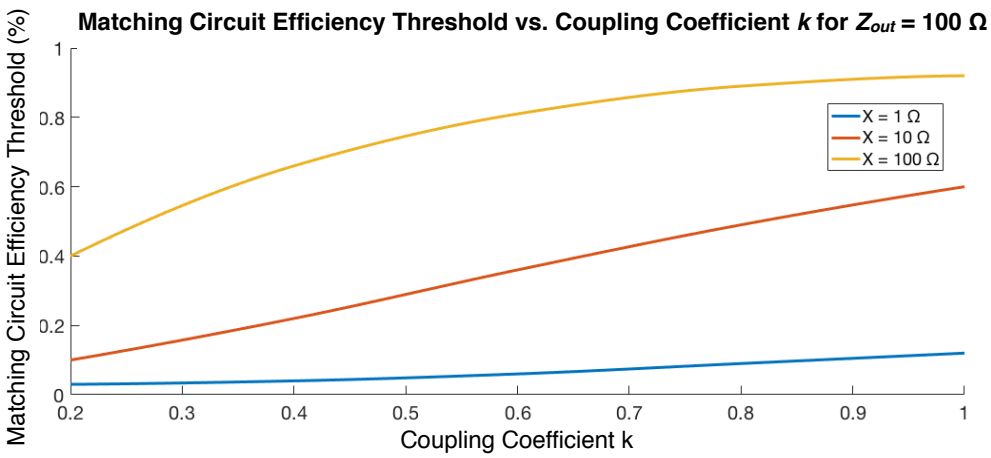

(c)

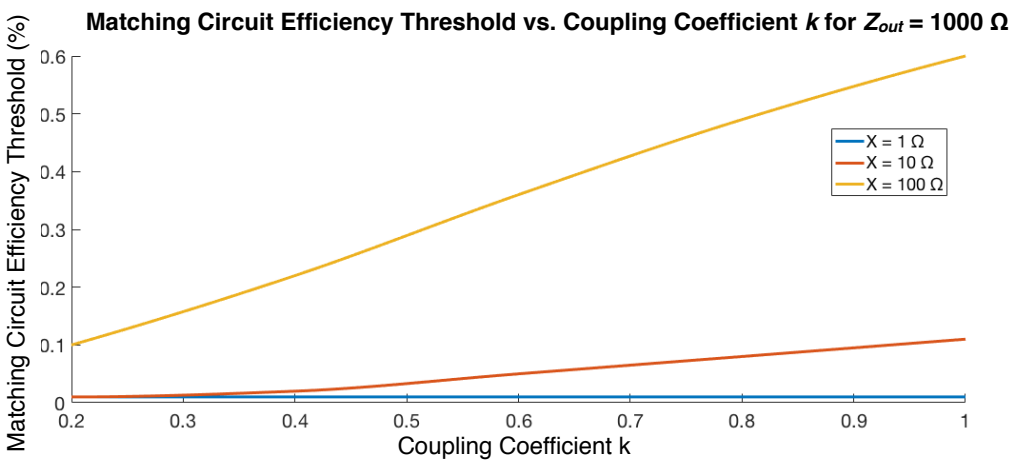

(d)

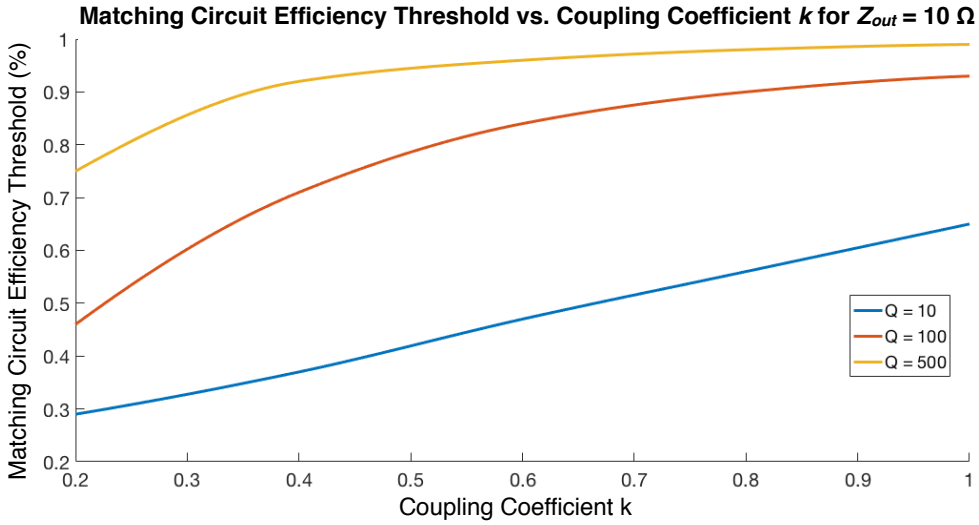

(a)

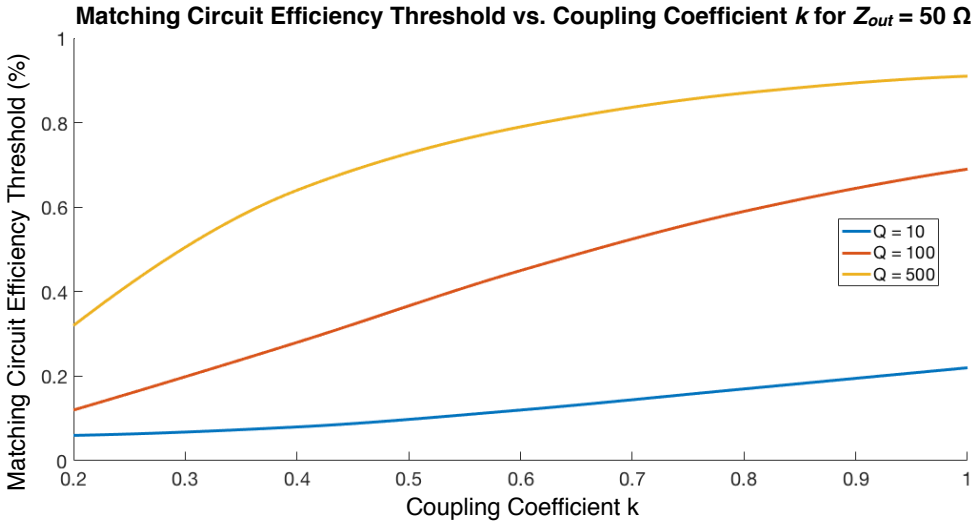

(b)

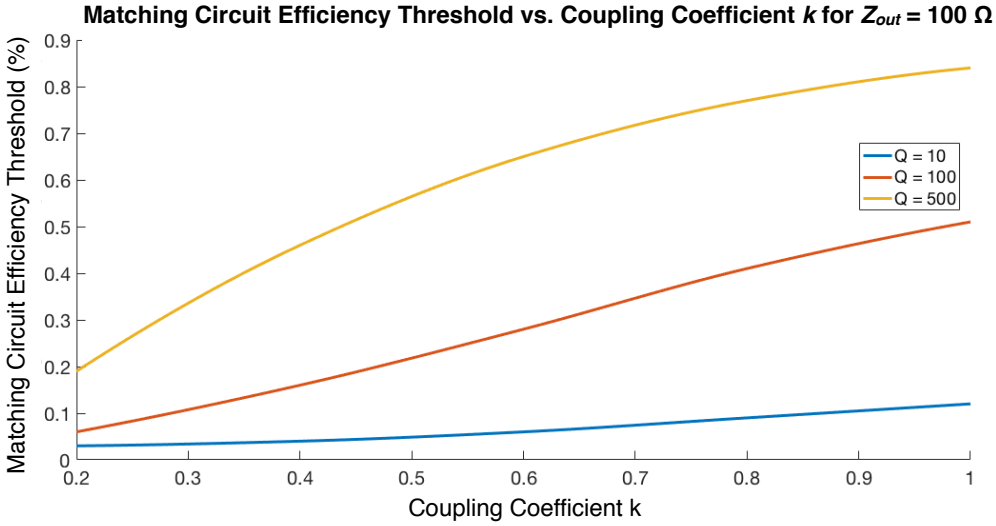

(c)

Fig. 2.7: X = 1 Ω matching circuit threshold efficiency as a function of coupling coefficient for (a) Z_{out} = 10 Ω, (b) Z_{out} = 50 Ω, (c) Z_{out} = 100 Ω, and (d) Z_{out} = 1000 Ω.

Fig. 2.7 continued

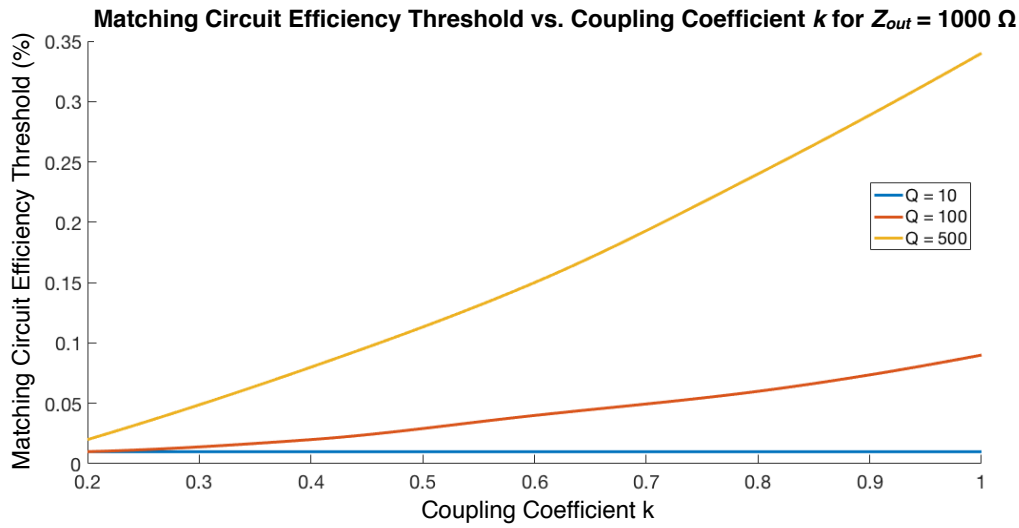

(d)

As can be seen from the figures above, the matching circuit efficiency threshold is directly proportional to the coupling coefficient. This is to say that a one-sided scheme is more likely to be optimal if the coupling coefficient is high since the matching network needs to be very efficient under this circumstance to justify a two-sided design. Conversely, for lower coupling, two-sided matching is clearly the optimal solution for all but very lossy matching network scenarios. That said, a higher Q also has the effect of raising the threshold. The effect of X is less straightforward, however. In Fig. 2.7a, it can be seen that the curve for X = 10 Ω has a higher threshold than the other curves. This is because, for this case, Z_{out} = 10 Ω is closer to the optimal two-sided matching solution when X = 10 Ω than it is for the other X values. In general, however, the threshold increases with higher Q and higher coupling strength. This study, therefore, injects an extra layer of consideration into the coupling circuit design process and gives rise to a rule of thumb: if the coupling is high and the loss low, for the sake of simplicity and efficiency, a one-sided match is likely preferable. On the other hand, for low coupling values and high loss, a two-sided matching is required. To switch gears back to the OWL WPT circuit model given in the previous sections, the next section will focus on a special case of the model that will be significant for the remainder of this work.

2.6 Short-Terminated Half-Wavelength Lines

Referring back to Fig. 2.3, consider the special case where $Z_{term} = 0$, $\theta_1 = n\pi/4$, and $\theta_2 = m\pi/4$, where m and n are odd integers. Under this circumstance,

$$Z_{\text{in\_tx}} = 2R_{lTL} + Z_o^2[j\omega C_t + \frac{\omega^2 k^2 C_r C_t}{j\omega C_r + Y_R}] \tag{2.33}$$

$$Z_{inl2} = [j\omega C_t + \frac{\omega^2 k^2 C_r C_t}{j\omega C_r + Y_R} + \frac{R_{lTL}}{Z_o^2}]^{-1} \tag{2.34}$$

$$\eta = \frac{\text{Re}(Y_{\text{out\_rx}}*)}{\text{Re}(Y_{\text{in\_tx}}*)} \left| \frac{Z_{\text{out\_rx}} Y_R \omega k \sqrt{(C_r C_t)} Z_o Z_{inl2}}{(Y_R + j\omega C_r)(Z_{inl2} R_{lTL} + Z_o^2)} \right|^2 \tag{2.35}$$

$$Z_{11} = 2R_{lTL} + j\omega C_t Z_o^2 (1 - k^2) \tag{2.36}$$

$$Z_{21} = Z_{11}\left(\frac{jkZ_o Z_{inl2}\sqrt{(C_r C_t)}}{Z_{inl2} R_{lTL} + Z_o^2}\right) \tag{2.37}$$

We may then use the Z-parameter expressions to determine the values of C_t and k analytically as

$$C_t = -j[\frac{Z_{11} - 2R_{lTL}}{\omega Z_o^2} - j\frac{C_r Z_{21}^2}{Z_o}] \tag{2.38}$$

$$k = \frac{-jZ_{21} C_r}{Z_o \sqrt{(C_r C_t)}} \tag{2.39}$$

This case is quite important for OWL WPT. As will be shown in later chapters, the case above presents optimal conditions for many OWL WPT systems, which is why its parameters were given here. In fact, this case will be used as a base design case for the rest of this work due to its utility. Again, this will be discussed further in the proceeding chapters.

2.7 Conclusions

In this chapter, the circuit model for an OWL WPT system was presented and solved, leading to a complete circuit theory approach to transmission line coupling. This chapter also investigated one-sided and two-sided matching techniques to present matching network design guidelines that will be used in the creation of practical systems. In the next chapter, the field theory of the GLine will be revisited and a much more in depth investigation of the field distribution will be conducted, culminating in an updated formulation for the GLine fields and transmission line parameters.

3. GOUBAU LINE FIELD DISTRIBUTION THEORY

In Section 1.3.1, the field distribution of the GLine mode was briefly discussed and several claims were made about this distribution. To show the validity of these claims and expand on the theory that has been presented in the literature, this chapter will be devoted to fully characterizing the GLine as a transmission line. This is important to do since the line has never been used for WPT before this work, and thus, several aspects of it have not been investigated until now. Furthermore, the presentation of the GLine theory presented in [19], while foundational and essential to this work, is outdated given current mathematical techniques and computational capabilities. As such, the mode theory of the GLine will updated as shown in the proceeding sections.

3.1 GLine Mode Solution

As stated in Chapter 1 and [19], the GLine fields constitute the solution to the Helmholtz equation for the case of an infinitely-long cylinder with finite radius and conductivity. They are restated here for convenience:

$$E_r = jA_i \frac{h}{\gamma_i} Z_1(\gamma_i r) e^{j(\omega t - hz)}, \tag{3.1a}$$

$$E_z = A_i Z_0(\gamma_i r) e^{j(\omega t - hz)}, \tag{3.1b}$$

$$H_\varphi = jA_i \frac{{k_i}^2}{\omega \mu \gamma_i} Z_1(\gamma_i r) e^{j(\omega t - hz)}, \tag{3.1c}$$

where h is the longitudinal propagation constant, γ is the radial wavenumber, ω is the radial frequency, A_i is the wave amplitude (where i denotes whether the field region is inside or outside the conductor), k_i is the total wavenumber, and $Z_n(x)$ is an nth order cylindrical function. Inside the conductor, $Z_n(x)$ is the Bessel function of the first kind and outside the conductor, $Z_n(x)$ is the Hankel function of the first kind. The following relations will also be restated:

$${k_o}^2 = h^2 + {\gamma_o}^2, \tag{3.2a}$$

$${k_c}^2 = h^2 + {\gamma_c}^2, \tag{3.2b}$$

where the "*o*" subscript denotes the region outside the conductor and the "*c*" subscript denotes the region inside the conductor. Note that, when the medium outside the conductor is a vacuum, the total wavenumbers are computed as

$$k_o = \omega\sqrt{\mu_0\varepsilon_0}, \tag{3.3a}$$

$$k_c = \omega\sqrt{\mu_0\varepsilon_c}, \tag{3.3b}$$

where

$$\varepsilon_c = \frac{\sigma}{j\omega} + \varepsilon_0 \tag{3.4}$$

and μ_0 and ε_0 are the permeability and permittivity of free space, respectively. To solve the mode, h, γ_o, and γ_c must be determined. By enforcing tangential E and H-field continuity at the conductor surface and applying appropriate cylindrical function approximations as was done in [19], we may obtain the following equations:

$$\xi ln\xi = \chi, \tag{3.5a}$$

$$\xi = (-j0.89\gamma r_w)^2, \tag{3.5b}$$

$$\chi = 2(0.89)^2 \frac{k^2 r_w}{|k_c|} e^{j3\pi/4}, \tag{3.5c}$$

$$\alpha = \arg(\xi), \tag{3.5d}$$

$$h = \left(k + 0.63\frac{|\xi|cos\alpha}{k{r_w}^2}\right) + j\left(0.63\frac{|\xi|sin\alpha}{k{r_w}^2}\right), \tag{3.5e}$$

where r_w is the conductor radius. Solving eqn. (3.5e) yields the propagation constant, and thus, the radial wavenumbers. However, this equation is transcendental in nature. This was circumvented in [19] by solving the equation graphically. Here, we will take a computational approach

by invoking the Lambert W function $W_k(z)$, which is the inverse function of ze^z, and thus satisfies the equations

$$W_k(ze^z) = z \tag{3.6a}$$

and

$$W_k(z)e^{W_k(z)} = z. \tag{3.6b}$$

With these definitions, it can be shown that

$$W_k(zlnz) = lnz. \tag{3.6c}$$

From here, we may write

$$\begin{aligned} W_k(\chi) &= W_k(\xi ln\xi) \\ e^{W_k(\chi)} &= e^{W_k(\xi ln\xi)} = \frac{\xi ln\xi}{W_k(\xi ln\xi)} \\ \therefore\ \xi &= e^{W_k(\chi)}. \end{aligned} \tag{3.7}$$

Here, k indicates the branch of W that is being evaluated [25]. It was found that the agreement between the formulation here and the one presented in [19] is maximized when $k = -1$, so that value of k will be used for all computations from here on. This agreement is expanded on further below. For the values of under consideration, we can expect that $\chi << 1$. Therefore, the Lambert W function may be expressed using the following asymptotic series expansion as below:

$$\begin{aligned} W_k(z) = \log z - 2\pi ik \\ - \log(\log z + 2\pi ik) \\ + \sum_{k=0}^{\infty}\sum_{m=1}^{\infty} c_{km}\,[\log(\log z \\ + 2\pi ik)]^m (\log z + 2\pi ik)^{-k-m}, \end{aligned} \tag{3.8}$$

where c_{km} are found using the Lagrange Inversion Theorem [25]-[26]. Alternatively, the function may be evaluated using iterative numerical techniques. With computational tools such as MATLAB (which have algorithms built into them to compute the function value), ξ may be readily calculated with high accuracy, allowing us to obtain the h and γ values. To confirm the validity of this approach and justify the selection of k, the following expressions from eqn. (12) of [19], which are derived in the appendix of [19] by starting from eqn. (3.5a) and invoking the small-angle approximation, will be considered for comparison:

$$|\xi| ln|\xi| = -|\chi|, \tag{3.9a}$$

$$\alpha = -\frac{\pi}{4}\left(1 - \frac{1}{ln|\xi| + 1}\right), \tag{3.9b}$$

$$\xi = |\xi| e^{j\alpha}. \tag{3.9c}$$

In [19], the above equations were used to plot the relationships between $|\chi|$, $|\xi|$, and α in order to solve eqn. (3.5a) graphically. While this approach is valid for certain ranges of , the derivations of eqns. (3.9a) and (3.9b) involve a second-order approximation (the small-angle approximation mentioned above). This approximation requires $|\xi|$ to be less than $1.1\text{x}10^{-4}$, and even at this threshold, while the error is small, it is not negligible. On the other hand, utilization of the Lambert W function requires no such approximation and thus yields a solution as accurate as the computation of the function is chosen to be. Nevertheless, with ξ computed numerically from eqn. (3.7) above, we may check the agreement between our quasi-analytical solution and the data presented in [19]. This is done by recreating Figs. 2 and 3 from [19] and incorporating the numerical data of this work into those plots for comparison. Fig. 3.1 illustrates this. Fig. 3.1a indicates strong agreement between the formulation of this work and the one in [19] when $|\xi|$ is small. However, as $|\xi|$ increases, magnitude deviations arise with maximal differences occurring when $|\xi|$ approaches the $1.1\text{x}10^{-4}$ threshold. Again, this is due to the weakening of the second-order approximation used to derive eqns. 3.9a and 3.9b. Nevertheless, the disagreement in Fig. 1a is within a 5% error margin for all values considered. At the same time, observing Fig.

3.1b. indicates very strong phase agreement for all values considered with a deviation of < 1% for both formulations. This indicates that eqn. (3.9b) is more weakly-coupled to the approximation than eqn. (3.9a) and further confirms the validity of the formulation presented here. Therefore, utilization of the k = -1 Lambert W function to solve the GLine mode is consistent with the theory established in [19], and since this technique does not require graphical treatment or additional approximations, it is the superior method for computing the GLine parameters (though it is noted that the formulation given in [19] was critical for developing the formulation of this work). With this, we may now solve the mode, Figs. 3.2-3.4 below show the computed values of γ_o, γ_c, and h:

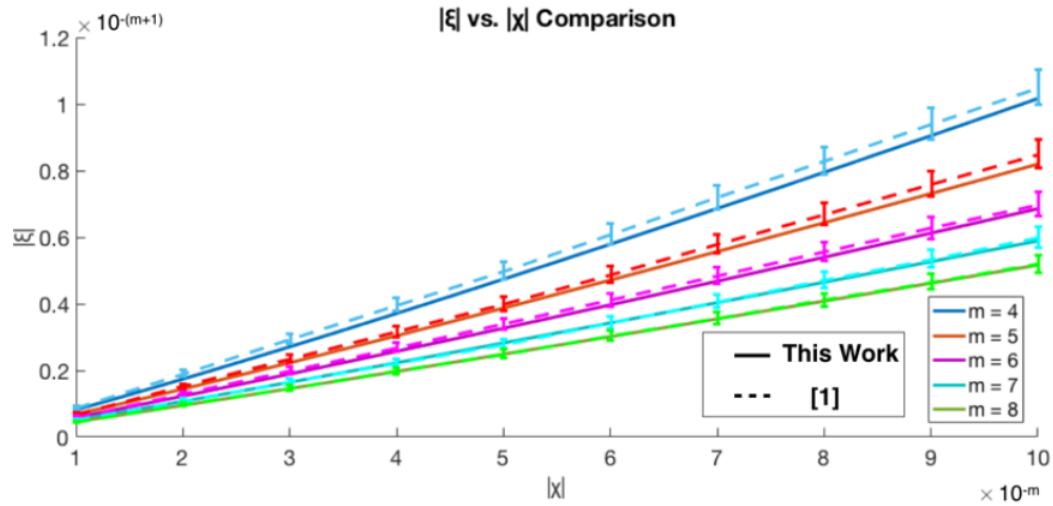

(a)

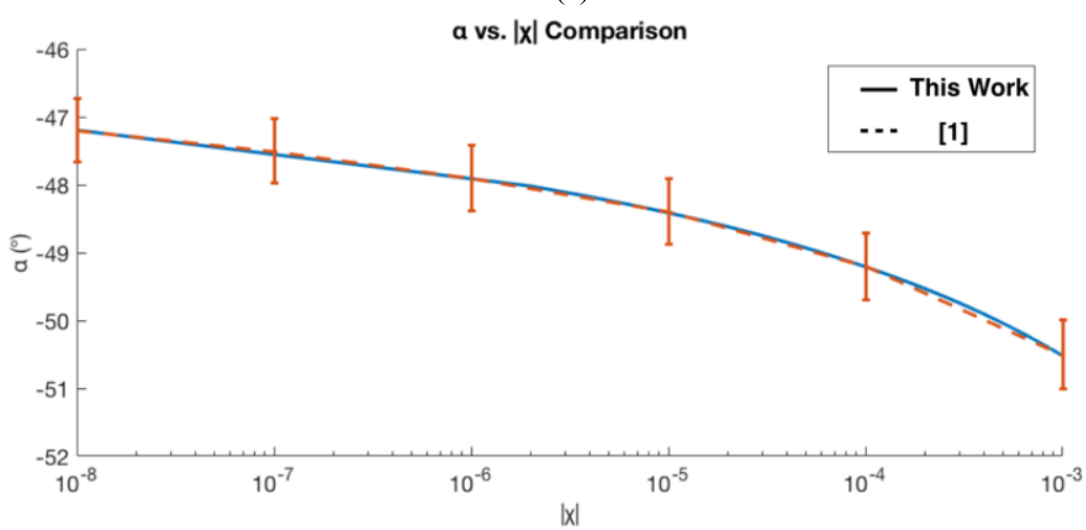

(b)

Fig. 3.1: (a) Relationship between and (b) relationship between and . Bars indicate a 5% error margin for (a) and a 1% error margin for (b) with respect to the values presented in [19].

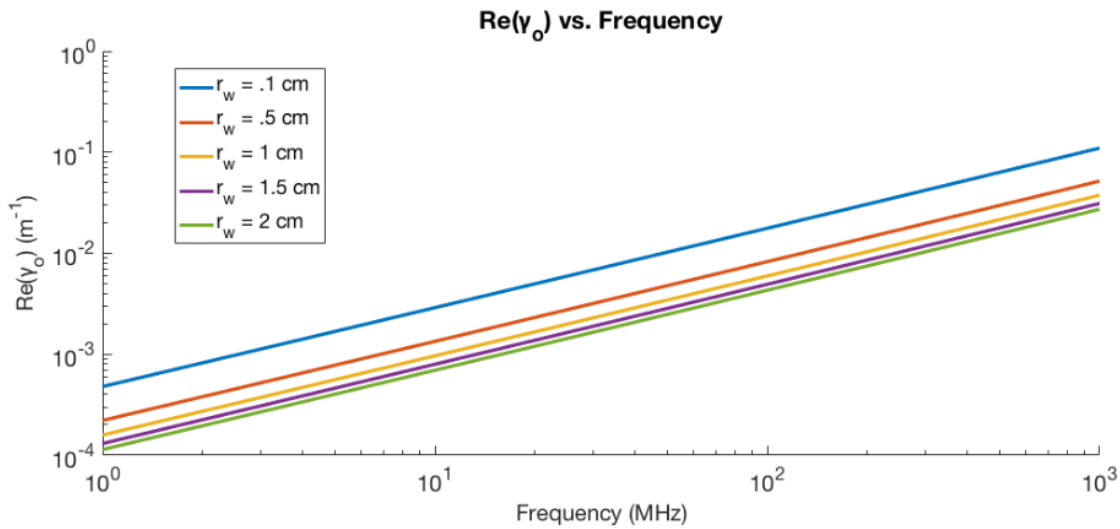

(a)

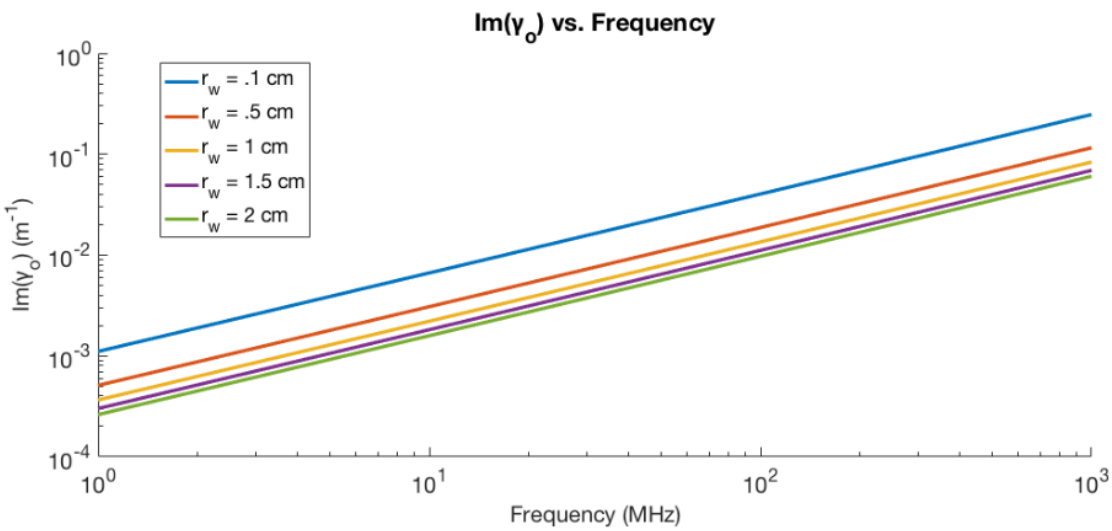

(b)

Fig. 3.2: Radial parameter γ_o (a) real part and (b) imaginary part as a function of frequency.

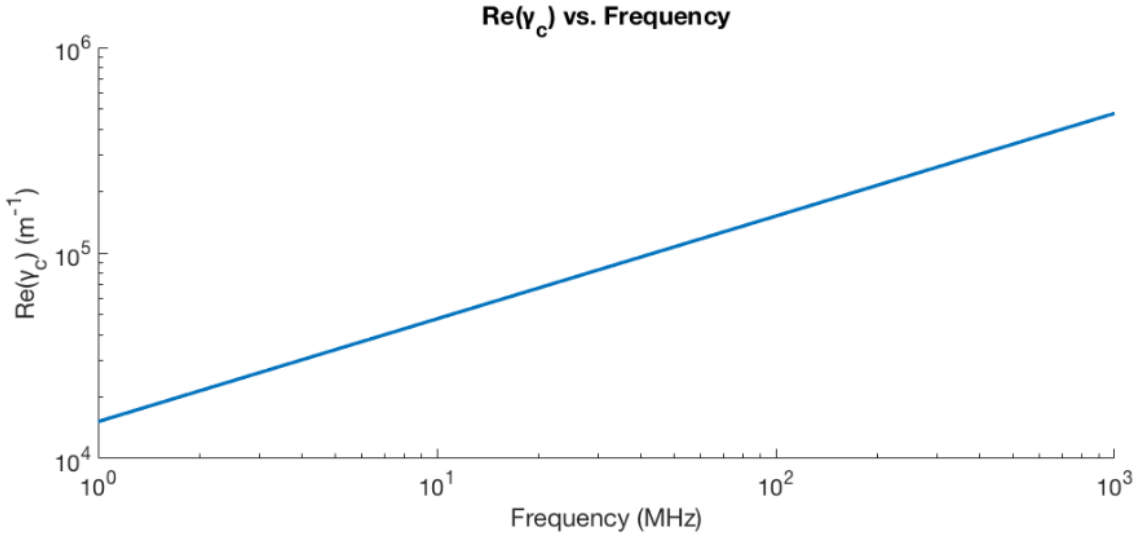

(a)

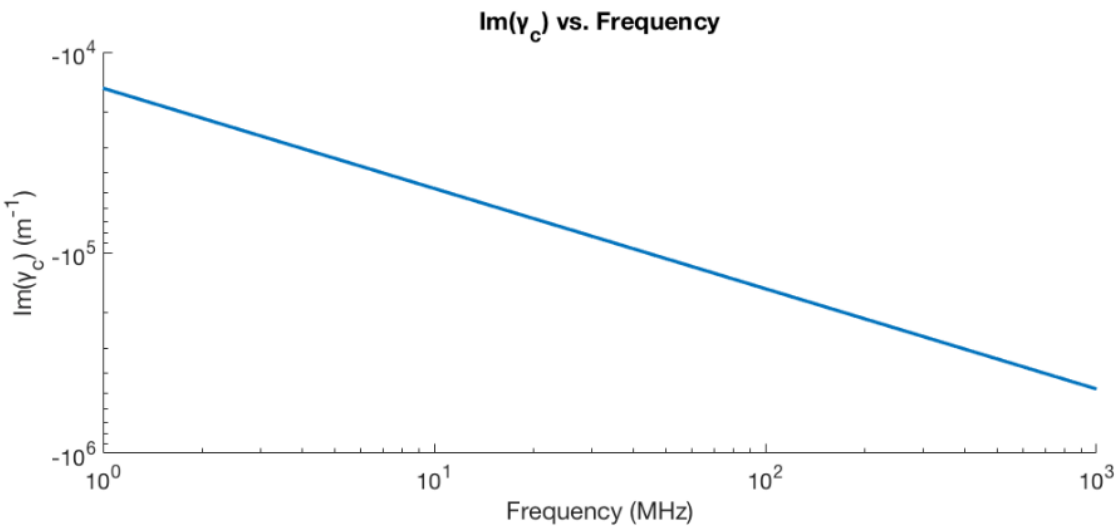

(b)

Fig. 3.3: Radial parameter γ_c (a) real part and (b) imaginary part as a function of frequency.

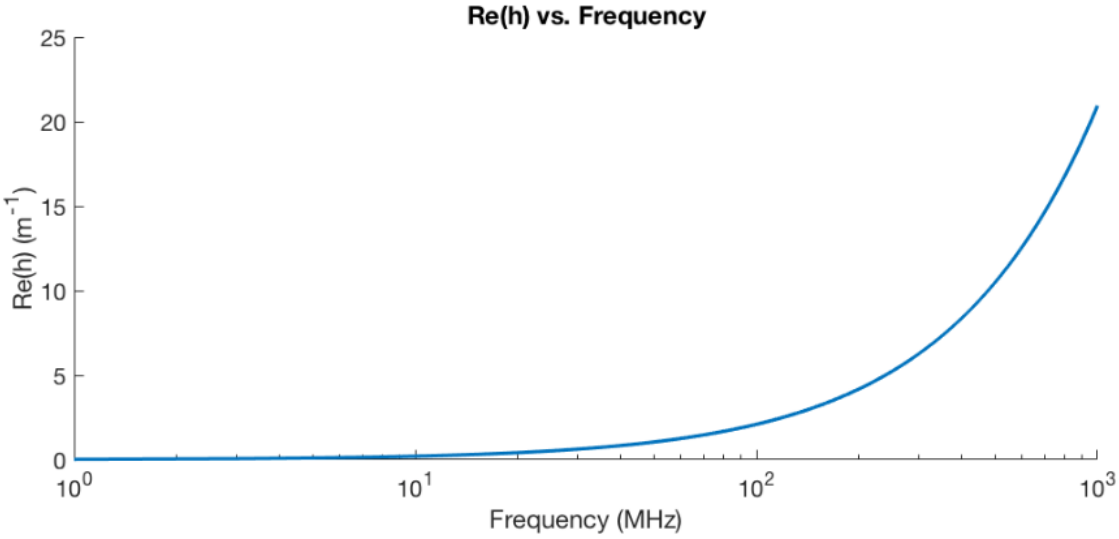

(a)

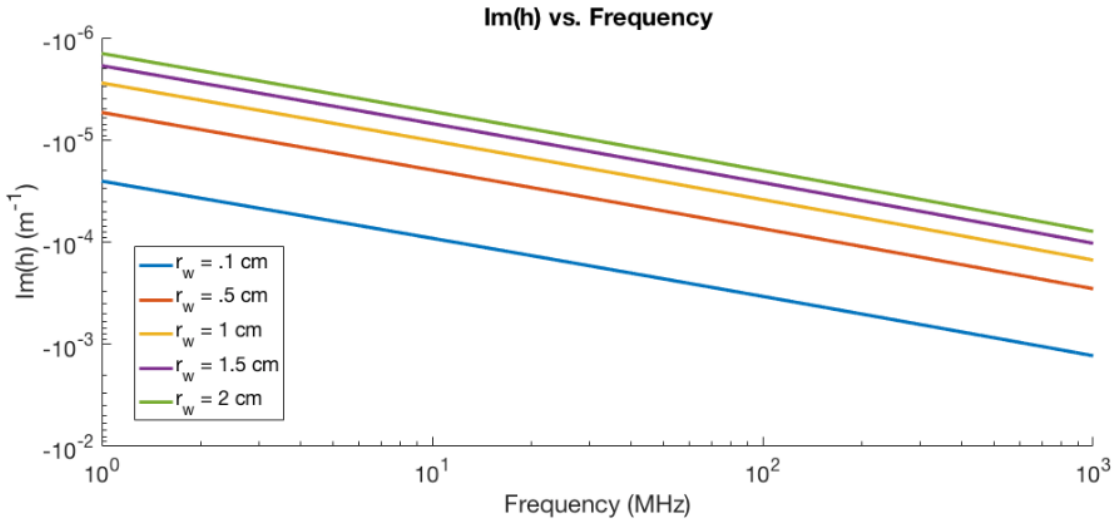

(b)

Fig. 3.4: Propagation constant *h* (a) real part and (b) imaginary part as a function of frequency.

As Fig. 3.4 shows, the imaginary part of h is small, meaning the line loss is also small, as will be shown in Section 3.4 below. Furthermore, γ_o also has a small magnitude, which results in a small argument for the Hankel functions in the field equations. This is an important characteristic, as will be shown in the next section. Note that γ_c and Re(h) are extremely weak functions of conductor radius, so only one curve is shown for these values in their respective plots. Furthermore, note that for all cases considered, , indicating that the longitudinal phase profile of the GLine mode is very similar to a plane wave traveling in free space.

3.2 GLine Field Fall-Off

During the derivation of eqn. (5) in [19], the first order Hankel function was represented by its asymptotic form, which is given below:

$$H_1^{(1)}(\gamma_o r) \approx -j\left(\frac{1}{\pi}\right)\left(\frac{2}{\gamma_o r}\right),\ \gamma_o r \ll 1. \tag{3.10}$$

Since γ_o is small, this form holds for relatively large values of r, meaning that we may effectively treat the radial E-field and azimuth H-field of the GLine as functions of $1/r$. This is significant for wireless power transfer applications, as radiative far-fields are used for longer range applications specifically because these fields also fall-off as $1/r$. GLine fields, however, are non-radiative, similar to the near-fields of electromagnetic structures. It should be noted, though, that the claim of non-radiation has yet to be verified mathematically. This will be done in the following discussions, but first, a formulation for the GLine power flow will be developed, as this will provide insight for both the GLine radiation and additional GLine characteristics. The following section details this formulation.

3.3 GLine Power Flow

From the frequency domain Poynting Theorem, the power density (W/m^2) of the line fields may be represented through the Poynting vector as

$$S = \frac{1}{2} Re(E \times H^*) = S_{in} + S_{out} + S_{rad}, \tag{3.11a}$$

$$S_{in} = \frac{1}{2} Re\left(\frac{|A_c|^2 h (k_c{}^*)^2}{\omega\mu|\gamma_c|^2} |J_1(\gamma_c r)|^2 e^{2Im(h)z}\right)\hat{z}, \tag{3.11b}$$

$$S_{out} = \frac{1}{2} Re\left(\frac{|A_o|^2 h k_o{}^2}{\omega\mu|\gamma_o|^2} |H_1(\gamma_o r)|^2 e^{2Im(h)z}\right)\hat{z}, \tag{3.11c}$$

$$S_{rad} = \frac{1}{2} Re\left(\frac{-j|A_o|^2 k_o{}^2}{\omega\mu\gamma_o{}^*} H_0(\gamma_o r) H_1(\gamma_o r)^* e^{2Im(h)z}\right)\hat{r}. \tag{3.11d}$$

Here, S_{in} corresponds to the longitudinal power flow inside the center conductor, S_{out} corresponds to the longitudinal power flow outside the center conductor, and S_{rad} corresponds to the radial power flow. To determine the power flow, the Poynting vector must be surface integrated as follows:

$$P = \frac{1}{2}\int S \cdot dS, \qquad dS = r d\varphi (dr\hat{z} + dz\hat{r}). \tag{3.12}$$

Therefore, the power flow of the GLine is represented as stated below:

$$P_{in} = \frac{1}{2}\int_0^{2\pi}\int_0^{r_w} Re\left(\frac{|A_c|^2 h (k_c{}^*)^2}{\omega\mu|\gamma_c|^2} |J_1(\gamma_c r)|^2 e^{2Im(h)z}\right) r dr d\varphi, \tag{3.13a}$$

$$P_{out} = \frac{1}{2}\int_0^{2\pi}\int_{r_w}^{\infty} Re\left(\frac{|A_o|^2 h k_o{}^2}{\omega\mu|\gamma_o|^2} |H_1(\gamma_o r)|^2 e^{2Im(h)z}\right) r dr d\varphi, \tag{3.13b}$$

$$P_{rad} = \frac{1}{2}\int_0^{2\pi}\int_0^{z_0} Re\left(\frac{-j|A_o|^2 k_o{}^2}{\omega\mu\gamma_o{}^*} H_0(\gamma_o r) H_1(\gamma_o r)^* e^{2Im(h)z}\right) r dz d\varphi, \tag{3.13c}$$

where r_w is the conductor radius and z_0 is the nominal GLine length (assuming a matched condition, the field solution is the same as the infinite length case). The exponential term in the longitudinal power expressions may be taken to be 1 since $Im(h)$ is small and there is no z differential in those integrals. Let us examine the longitudinal power flow first. The integral for the P_{out} component has closed forms similar to eqn. (19) of [19], which is restated here with z taken to be 0:

$$P_{out} = -\frac{1}{2} Re\{2\pi |A_o|^2 \sqrt{\frac{\varepsilon_o}{\mu_o}} \frac{hk_o}{|\gamma_o|^2 (\gamma_o{}^2 - \gamma_o{}^{*2})} \times (\gamma_o{}^* r_w H_1(\gamma_o r_w) H_0(\gamma_o r_w)^* - \gamma_o r_w H_1(\gamma_o r_w)^* H_0(\gamma_o r_w))\} \tag{3.14}$$

This may be readily calculated numerically. The P_{in} integral, on the other hand, presents a challenge due to the magnitude of γ_c in the Bessel function argument. Since the line conductivity is high, $Im(\gamma_c) >> 1$, which leads to computational overflow. To understand why, we invoke an integral representation of the Bessel function of the first kind:

$$J_1(\gamma_c r) = \int_{-\pi}^{\pi} e^{j(\gamma_c r \sin\tau - \tau)} d\tau \tag{3.15a}$$

$$= \int_{-\pi}^{\pi} e^{j(Re(\gamma_c) r \sin\tau - \tau)} e^{-Im(\gamma_c) r \sin\tau} d\tau \tag{3.15b}$$

By inspecting the kernel of the integral above, it is clear that if $Im(\gamma_c)$ is large and negative, the magnitude of the kernel will grow rapidly. To demonstrate this, let $\tau = \pi/2$ and $r = .01$. For a copper GLine at 100 Mhz, γ_c 1.52 x $10^5(1 - j)$, which means evaluating the integral would require computation of e^{1520}. Clearly, this evaluation is not possible for most computational hardware.

A question that naturally arises from this consideration is whether or not the fields can be worked with within the GLine conductor if they are effectively incalculable. In fact, the field magnitudes within the center conductor are comparable in magnitude to the fields outside the conductor, which are readily calculable. This is justified mathematically by enforcing the tangential E-field boundary condition at the conductor edge to relate the field amplitudes inside and outside the conductor as

$$A_c = A_o \frac{H_0(\gamma_o r_w)}{J_0(\gamma_c r_w)}. \tag{3.16}$$

This means that the fields within the center conductor are effectively normalized by the term . Since γ_c is large and complex, it can be shown that

$$\left|\frac{J_n(\gamma_c r)}{J_0(\gamma_c r_w)}\right| \leq 1, r \leq r_w, n = 0, 1. \tag{3.17}$$

All this is to say that the field magnitudes within the conductor never exceed the order of magnitude of the fields outside the conductor. The reason the inner fields still cannot be computed in a straightforward way, despite the considerations given above, is that the numerator and denominator of the ratio in eqn. (3.16) must be computed separately before they can be divided and there is no easily obtained expression that can circumnavigate this step.

This brings us back to the GLine longitudinal power flow formulation, which includes a Bessel function term with γ_c in the argument. Since is not obtainable in general, how is power flow to be calculated? To answer this question, we examine both the P_{in} and P_{out} kernals evaluated for $r = a$ and write

$$K_{in}^{r_w} = \frac{|A_c|^2 h(k_c{}^*)^2}{\omega\mu|\gamma_c|^2}|J_1(\gamma_c r_w)|^2, \tag{3.18a}$$

$$K_{out}^{r_w} = \frac{|A_o|^2 h k_o{}^2}{\omega\mu|\gamma_o|^2}|H_1(\gamma_o r_w)|^2. \tag{3.18b}$$

From eqn. (3.16) of this work and eqn. (4) of [19], we may express the P_{in} kernel as

$$\begin{aligned} K_{in}^{r_w} &= \frac{|A_o|^2 h(k_c{}^*)^2}{\omega\mu|\gamma_c|^2}\left|\frac{\gamma_c}{\gamma_o}\left(\frac{k_o}{k_c}\right)^2 H_1(\gamma_o r_w)\right|^2 \\ &=> K_{in}^{r_w} = \frac{(k_c{}^*)^2}{|k_c|^2}K_{out}^{r_w} \approx jK_{out}^{r_w}. \end{aligned} \tag{3.19}$$

$K_{out}^{r_w}$ is almost purely real, meaning that $K_{in}^{r_w}$ is almost purely imaginary. Therefore, $P_{in} \approx 0$ and its integral may be safely neglected.

Next, we will evaluate the radiated power by using the integral expression of P_{rad}. Note that there is no r differential in this integral, meaning that P_{rad} is apparently a function of r. In conventional radiation problems, the factor of r from the surface integral differential is mathematically canceled either from the algebra or the numerics of the problem. This is intuitive, as the surface of integration should not affect the total amount of power radiated. Here, however, this is not the case, as the value of the radiated power kernel varies with r. In fact, it can be shown that the following expression holds:

$$\lim_{r\to\infty} rH_0(\gamma_o r)H_1(\gamma_o r)^* = 0. \tag{3.20}$$

This is demonstrated by invoking the large argument asymptotic form for the Hankel function:

$$H_n{}^{(1)}(x) \approx \sqrt{\frac{2}{\pi x}} e^{j\left(x-\frac{n\pi}{2}-\frac{\pi}{4}\right)}, -\pi < \arg(x) < 2\pi. \tag{3.21}$$

With this expression, we may write

$$rH_0(\gamma_o r)H_1(\gamma_o r)^* \approx \frac{-2}{\pi} e^{-2rIm(\gamma_o)}. \tag{3.22}$$

Since $Im(\gamma_o) > 0,$ this expression approaches 0 as r approaches infinity. Therefore, no power is radiated from the system. The physical interpretation of this is that the Poynting vector directionality varies with r, and as r increases, the r-directed vector weakens until it disappears entirely, even though power flows outward closer to the conductor.

If one is unconvinced by this, it may additionally be shown that even if the maximum value of S_{rad} were taken to be its value for all space, the resultant radiated power would still be negligible compared to longitudinal power flow. To demonstrate this, let us consider a GLine with a radius of 1 cm operating at 100 MHz with a longitudinal power flow of 1 W. We may determine the corresponding A_o by setting P_{out} equal to 1, evaluating eqn. (3.14), and backing out what A_o must be. For this example, $A_o = 6.148 \times 10^{-4}$. Our goal is to find the hypothetical value of z_0 that will lead to a peak radiated power of 1 W. The integral for P_{rad} may be taken quite easily and set equal to 1 so that z_0 may be found. If this is done, it is revealed that z_0 must exceed 266

km before the "radiated power" reaches 1 W. With this, we may safely conclude that radiation from the GLine is negligible. In the next section, we will evaluate the physical current of the GLine and compare it to other line structures.

3.4 GLine Current

The GLine ohmic current may be evaluated by applying Ohm's Law:

$$J = \sigma E. \tag{3.23}$$

We are only interested in longitudinal current, as this is the current flowing down the line. As such, the current flow for the GLine can be expressed as

$$J_z = \sigma E_z = \sigma A_c J_0(\gamma_c r) e^{j(\omega t - hz)}, 0 < r < r_w. \tag{3.24}$$

Let *t* and *z* be equal to zero. To find the total ohmic current on the line, we take the surface integral:

$$I_z = \int_0^{2\pi} \int_0^{r_w} \sigma A_c J_0(\gamma_c r) r dr d\varphi. \tag{3.25}$$

It can be shown through the use of the Bessel function recurrence relations that

$$\int x J_0(x) dx = x J_1(x). \tag{3.26}$$

By invoking this fact, we may express the total ohmic current flow on the GLine as

$$\begin{aligned} I_z &= \frac{2\pi\sigma A_c}{\gamma_c} r_w J_1(\gamma_c r_w) \\ &= \frac{2\pi\sigma A_o}{\gamma_o} r_w H_1(\gamma_o r_w) \left(\frac{k_o}{k_c}\right)^2. \end{aligned} \tag{3.27}$$

One aspect of the GLine that merits discussion is its lack of return path current, given that the ground plane is effectively located at infinity. Since the GLine is a non-radiator, it must also be current neutral. To evaluate this condition, we must account for both the current inside the conductor and the displacement current outside the conductor. This displacement current is given as follows:

$$\begin{aligned} I_{dis} &= \int_0^{2\pi} \int_{r_w}^{\infty} j\omega\varepsilon_0 A_o H_0(\gamma_o r) r dr d\varphi \\ &= \frac{-j\omega\varepsilon_0 2\pi A_o}{\gamma_o} r_w H_1(\gamma_o r_w)\,. \end{aligned} \tag{3.28}$$

For all cases where the formulation detailed in Section 3.1 holds,

$$\begin{aligned} \frac{\sigma}{j\omega} &\gg \varepsilon_0, \\ \sigma &\approx j\omega\varepsilon_c. \end{aligned} \tag{3.29}$$

By taking this, enforcing H-field continuity at the conductor interface, and noting that

$$\frac{{k_i}^2}{\omega\mu\gamma_i} = \frac{\omega\varepsilon_i}{\gamma_i}, \tag{3.30}$$

it can be shown that

$$\begin{aligned} &\frac{2\pi\sigma A_c}{\gamma_c} r_w J_1(\gamma_c r_w) \\ &= \frac{j\omega\varepsilon_0 2\pi A_o}{\gamma_o} r_w H_1(\gamma_o r_w). \end{aligned} \tag{3.31}$$

Therefore,

$$I_z + I_{dis} = 0. \tag{3.32}$$

This means that, effectively, the displacement current outside the line is the “return current” that allows the line to attain current neutrality, but it does not have ohmic loss associated with it.

Next, we will compare the ohmic current flow on the GLine to that of an air-dielectric coax carrying the same longitudinal power. The coax is an intuitive choice for comparison given that the GLine is essentially a coax with its ground plane placed at infinity. Note that this analysis assumes TEM mode excitation only in the coax. The current and power flow of a coax, respectively, may be expressed as

$$I_{coax} = \frac{2\pi V}{\eta_0 \ln\left(\frac{r_o}{r_{in}}\right)},$$
$$P_{coax} = \frac{\pi V^2}{\eta_0 \ln\left(\frac{r_o}{r_{in}}\right)} \tag{3.33}$$

where V is the voltage between the inner and outer conductors, η_0 is the intrinsic impedance of free space, r_{in} is the inner conductor radius, and r_o is the outer radius. Since the coax has a 50 Ω characteristic impedance, if we let $r_{in} = r_w$, r_o is computed as

$$r_o = r_w e^{Z_0 2\pi/\eta_0}, \eta_0 \approx 120\pi, \tag{3.34}$$

where Z_0 is the coax characteristic impedance. By setting P_{coax} equal to 1 and solving for V, we may compare the currents on both the GLine and the coax. Through doing this and taking the ratio of the coax current magnitude to the GLine current magnitude, we find that the coax current is always larger than the GLine current. The current magnitude ratio is illustrated in Fig. 3.5 below for 50 Ω and 75 Ω lines when the inner conductor radius is .1 cm. We may also do this analysis for multiple characteristic impedances, as is shown in Section 3.8. For the 50 Ω case, the coax current exceeds the GLine current by a factor of 4 or more for all the considered frequency and inner conductor radius cases, which is a substantial difference. Note that the current ratio decreases as the coax characteristic impedance increase. This is expected since a coax with a larger outer radius is closer to a GLine in structure (neglecting higher-order modes, which are suppressed as $r \to \infty$).

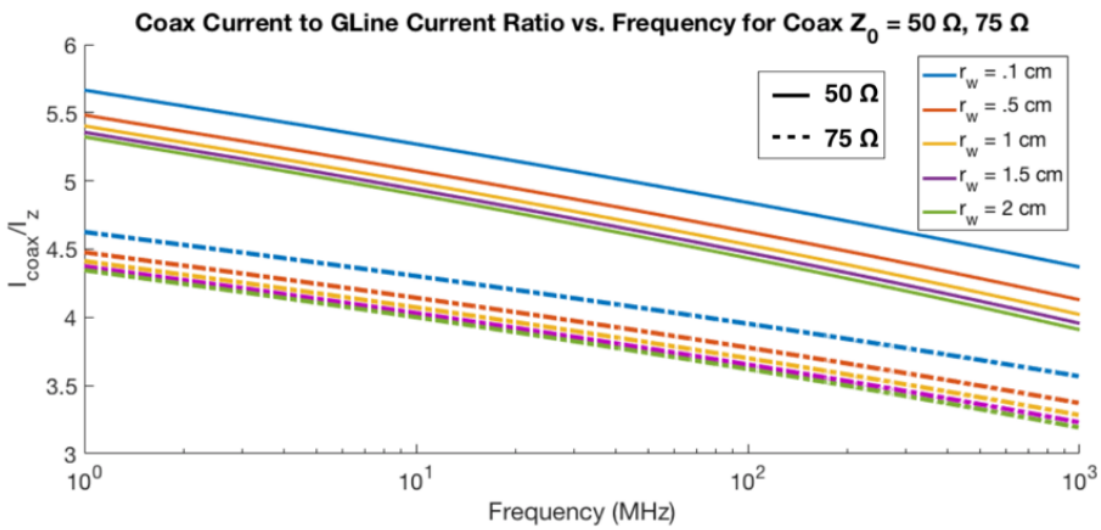

Fig. 3.5: Coax to GLine current magnitude ratio for 50 Ω and 75 Ω cables.

The primary takeaway of the treatment above is that the GLine carries substantially less physical current than a comparable coax with a useful design. Additionally, one other consideration strengthens this takeaway. The GLine has no physical return current since current neutrality is achieved with displacement current only. This effectively halves the would-be ohmic loss for the GLine, improving its loss performance further over the coax.

3.5 GLine Equivalent TEM Formulation

The transmission line parameters of a TEM waveguide are based on the voltage and current wave solutions to Telegrapher's Equations and are typically hinged on the lumped-element transmission line model. Our goal is to find the equivalent lumped-element values for the GLine in order to determine the line characteristic impedance, i.e., the ratio between the line's voltage and current waves. For the GLine, we may neglect R' and G' in the model above since the loss is so small. Therefore, the characteristic impedance can be expressed as

$$Z_0 = \sqrt{\frac{L'}{C'}} \tag{3.35}$$

where *L'* is the line's inductance per unit meter and *C'* is the capacitance per unit meter. It should be noted that the lumped-element transmission line formulation is only valid for a TEM structure, whereas the GLine is based on a fundamental TM mode. We may circumvent this by finding the GLine's equivalent coaxial cable representation. That is, for a given conductor radius, *a*, we will find the outer radius, *b*, that will form a coax with equivalent power flow characteristics to those of the GLine. We will show that this is a valid technique by proving that the effective *C'* and *L'* values of the GLine are equal to those of a coax with inner radius *a* and outer radius *b*. This is done below.

3.5.1 Capacitance Per Unit Meter

C' is defined by the following equation:

$$C' = \frac{Q'}{V_g} \tag{3.36}$$

where *Q'* is the equivalent charge per unit meter and V_g is the equivalent potential. To find the effective charge, we invoke the integral form of Guass' Law around the center conductor and write

$$Q' = \int_0^{2\pi} \varepsilon_0 E_r r d\varphi = \frac{j\varepsilon_0 2\pi A_0 h r H_1(\gamma_o r)}{\gamma_o}. \tag{3.37}$$

Note that the value of *r* is unspecified. For most conventional scenarios, multiplying *r* by the E-field while applying Gauss' Law yields an expression that is constant in *r*. For the values of *r* for which the Hankel function argument is small, the asymptotic form of the Hankel function of eqn. (3.10) suggests that the charge expression is indeed constant in *r* as well. However, it should be noted that as , this asymptotic form no longer applies. In fact, one may show using the large argument asymptotic form of eqn. (3.21) and L-Hopital's rule that

$$\lim_{r\to\infty} rH_1(\gamma_o r) = 0. \tag{3.38}$$

This means the GLine is effectively "charge neutral" according to Maxwell's equations, but it also calls into question the proper choice of r. Nevertheless, since γ_o is very small, the charge value is approximately constant for a wide range of r values exceeding thousands of meters. As such, let us assume that the effective TEM charge is the value found when that $\gamma_o r << 1$ such that

$$Q' \approx \frac{\varepsilon_0 4A_0 h}{{\gamma_o}^2}. \tag{3.39}$$

The effective voltage is found by taking the line integral of the radial E-field between 0 and b as follows:

$$\begin{aligned} V_g = \int_0^b E_r dr = \int_0^{r_w} jA_c \frac{h}{\gamma_c} J_1(\gamma_c r)\, dr \\ + \int_{r_w}^b jA_o \frac{h}{\gamma_o} H_1(\gamma_o r)\, dr. \end{aligned} \tag{3.40}$$

Using the derivative recurrence relations and negative order identities for cylindrical functions, it can be shown that

$$\frac{dZ_0(\gamma_i r)}{dr} = -\gamma_i Z_1(\gamma_i r). \tag{3.41}$$

Therefore,

$$\int Z_1(\gamma_i r) dr = -\frac{1}{\gamma_i} Z_0(\gamma_i r). \tag{3.42}$$

With this, we may write

$$\begin{aligned} V_g &= \left[-jA_c \frac{h}{{\gamma_c}^2} J_0(\gamma_c r)\right]_0^{r_w} + \left[-jA_o \frac{h}{{\gamma_o}^2} H_0(\gamma_o r)\right]_{r_w}^b \\ &= \frac{jA_o h H_0(\gamma_o r_w)}{{\gamma_c}^2 J_0(\gamma_c r_w)} - \frac{jA_o h H_0(\gamma_o r_w)}{{\gamma_c}^2} \\ &\quad + \frac{jA_o h}{{\gamma_o}^2}[H_0(\gamma_o r_w) - H_0(\gamma_o b)] \\ &\approx \frac{jA_o h}{{\gamma_o}^2}[H_0(\gamma_o r_w) - H_0(\gamma_o b)] \end{aligned} \tag{3.43}$$

We can justify neglecting the first two terms in the integration result since $\frac{1}{\gamma_c^2} << \frac{1}{\gamma_o^2}$. By assuming the value of b is such that $\gamma_o b << 1$ and invoking the small argument asymptotic form of the zero-order Hankel function given below,

$$H_0^{(1)}(\gamma_o r) = j\left(\frac{2}{\pi}\right)\ln(-j0.89\gamma_o r),\ \gamma_o r \ll 1, \tag{3.44}$$

the final TEM voltage expression becomes

$$V_g \approx \frac{A_o h}{{\gamma_o}^2}\left(\frac{2}{\pi}\right)\ln\left(\frac{b}{r_w}\right). \tag{3.45}$$

We may now evaluate the capacitance per unit length to derive the following expression:

$$C' = \frac{2\pi\varepsilon_0}{\ln\left(\frac{b}{r_w}\right)}. \tag{3.46}$$

Note that this expression is identical to the expression for the capacitance per unit length of a coaxial cable with inner radius r_w and outer radius b
as expected. Next, we will derive the equivalent inductance per unit meter.

3.5.2 Inductance Per Unit Meter

L' is defined by the following equation:

$$L' = \frac{\Phi'}{I_z} \tag{3.47}$$

where Φ' is the magnetic flux per unit meter and I_z is the line physical current. Φ' may be computed from the GLine H-field as follows:

$$\Phi' = \int_0^b \mu_0 H_\varphi dr$$

$$= \int_0^{r_w} jA_c \frac{{k_c}^2}{\omega\gamma_c} J_1(\gamma_c r)dr + \int_{r_w}^b jA_o \frac{{k_o}^2}{\omega\gamma_o} H_1(\gamma_o r)dr$$

$$\approx \frac{jA_o {k_o}^2}{\omega {\gamma_o}^2}[H_0(\gamma_o r_w) - H_0(\gamma_o b)] \tag{3.48}$$

$$\approx \frac{A_o {k_o}^2}{\omega {\gamma_o}^2}\left(\frac{2}{\pi}\right)\ln\left(\frac{b}{r_w}\right).$$

Using the small argument asymptotic form once more, I_z may be restated as

$$I_z = -I_{dis} \approx \frac{4A_o\omega\varepsilon_0}{{\gamma_o}^2}. \tag{3.49}$$

From here, we may compute the inductance per unit meter to yield the following expression:

$$L' = \frac{\mu_0 \ln\left(\frac{b}{r_w}\right)}{2\pi} \tag{3.50}$$

Once again, this expression is identical to that of a coax with inner radius r_w and outer radius b, proving the validity of the formulation.

3.5.3 Characteristic Impedance

We may now write an expression the GLine equivalent TEM characteristic impedance. Clearly, since both the capacitance and inductance expressions match those of a coaxial cable, the impedance expression will match as well. The characteristic impedance is thus described as below:

$$Z_0 = \frac{\eta_0 \ln\left(\frac{b}{r_w}\right)}{2\pi}, \tag{3.51}$$

where η_0 is the intrinsic impedance of free space. This brings us to the determination of b. As stated above, b is chosen such that the power flowing down the equivalent coax is the same as

the power flowing down the GLine. We may compute the power flow of our formulation through the following expression:

$$P_{eq} = \frac{1}{2} Re\left(V_g I_z^*\right) = \frac{4{A_o}^2 \omega \varepsilon_0 Re(h)}{\pi |\gamma_o|^4} \ln\left(\frac{b}{r_w}\right), \tag{3.52}$$

which implies that

$$b = r_w \exp\left(\frac{P_{eq} \pi |\gamma_o|^4}{4|A_o|^2 \omega \varepsilon_0 Re(h)}\right). \tag{3.53}$$

If we equate P_{eq} to P_{out} from eqn. (14) and define a new power term,

$$P_0 = \frac{P_{out}}{|A_o|^2}, \tag{3.54}$$

then b becomes

$$b = r_w \exp\left(\frac{P_0 \pi |\gamma_o|^4}{4\omega \varepsilon_0 Re(h)}\right). \tag{3.55}$$

With this, we may calculate the GLine equivalent characteristic impedance as a function of conductor radius and frequency. This is plotted in Fig. 3.6 below:

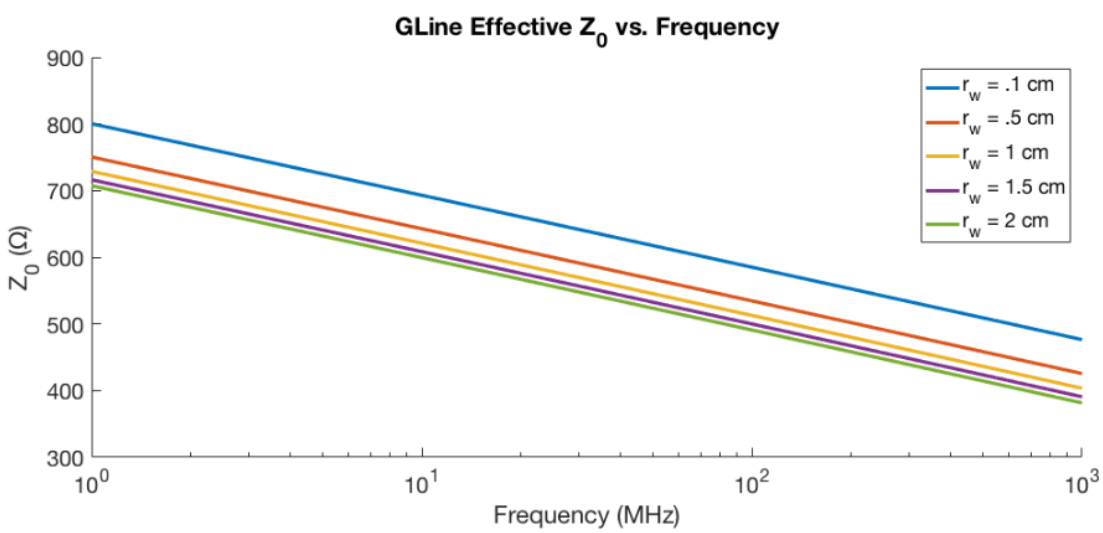

Fig. 3.6: GLine effective Z_0 as a function of frequency.

GLine signal attenuation may be characterized in two ways. The first is by observing the imaginary part of the GLine propagation constant h, which was computed in Section II. The second is to use the equivalent TEM formulation developed in Section IV to compute the attenuation constant α_g via the following equation:

$$\alpha_g = \frac{R_s}{2(2\pi r_w)Z_0}, \tag{3.56}$$

where R_s is the sheet resistance of the conductor expressed as

$$R_s = \sqrt{\frac{\pi f \mu}{\sigma}}, \tag{3.57}$$

and Z_0 is the characteristic impedance of the GLine computed from eqn. (3.51) [27]. In the figure below, both the imaginary part of h and are plotted as a function of frequency for several conductor radii. Note that the imaginary part of h and are approximately the same for all the cases above. This indicates that the TEM formulation for the GLine is self-consistent with the field solution. It also indicates that, while the current distribution within the GLine conductor cannot be computed exactly, we may assume that its decay is radially exponential. We may assume this because the equation for R_s is only valid under this assumption, and since there's agreement between the attenuation constants in Fig. 3.7, that means the current must decay approximately exponentially.

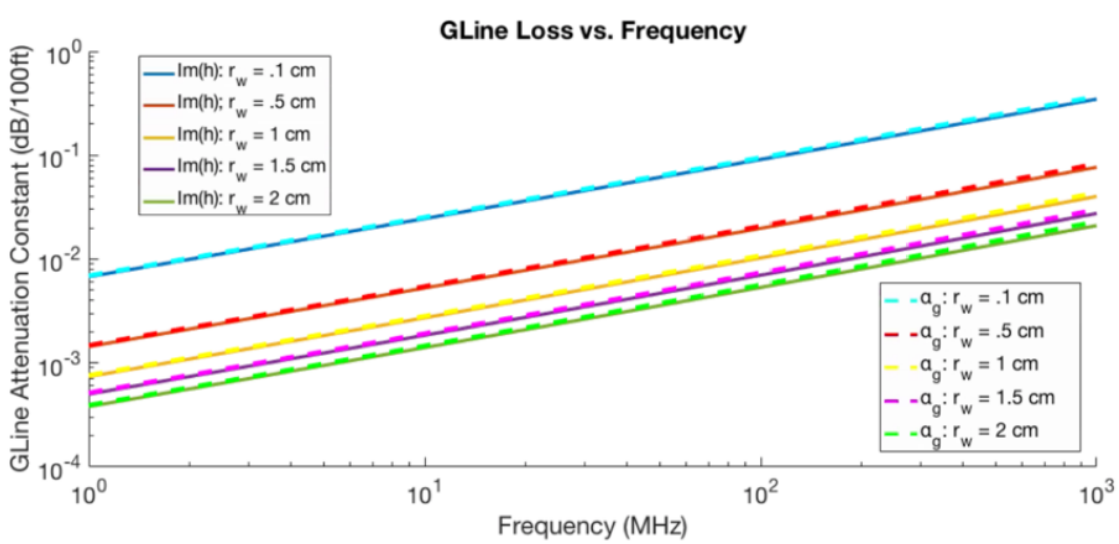

Fig. 3.7: GLine ohmic loss as a function of frequency computed from propagation constant and TEM formulation.

As an extra verification, we may compare the loss data obtained here to the loss data presented in [19]. In Fig. 3.8 below, Fig. 4 of [19] is recreated with the data of this work overlaid over the data of [19], presenting a comparison of the attenuation values for several GLine radii.

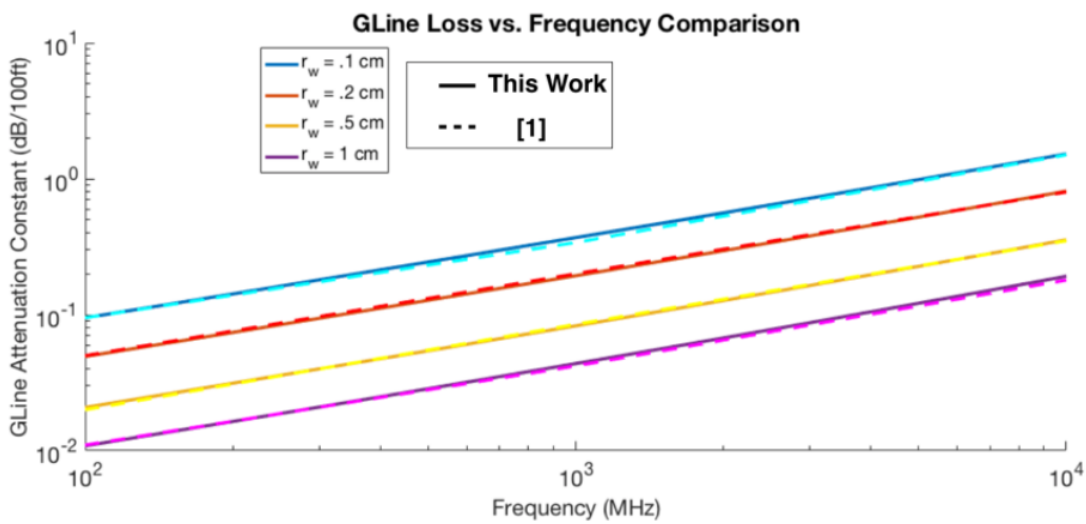

Fig. 3.8: Comparison of GLine attenuation data from this work and from [19].

As Fig. 3.8 indicates, there is very strong agreement between the computed attenuation values of this work and the data shown in Fig. 4 of [19], again validating the formulation presented here. Note that the frequency range in Fig. 3.8 is 100 MHz to 10 GHz, as opposed to the 1 MHz to 1 GHz range shown in previous plots.

Now that the GLine loss has been computed, it may be compared to the loss of a comparable coaxial cable. If the coax dielectric is air, the attenuation is a product of ohmic loss only. With this, we may express the coax attenuation constant α_c as follows:

$$\alpha_c = \frac{R_s}{2Z_0}\left(\frac{1}{(2\pi r_{in})} + \frac{1}{(2\pi r_o)}\right), \tag{3.58}$$

where r_{in} and r_o are defined as in eqn. (3.34). In Section 3.8, several plots are given to show the ohmic loss of the coaxial cable as a function of frequency and inner conductor radius for an air dielectric cable. From this data, it is clear that the loss of the GLine is substantially smaller than

that of the coax for all cases. This property is a product of the large GLine characteristic impedance coupled with the fact that the GLine contains no ohmic current return path. For direct comparison, the GLine loss for a .1 cm inner conductor radius is plotted next to the coax loss of 50 Ω and 75 Ω cables with the same inner conductor radius and an air dielectric.

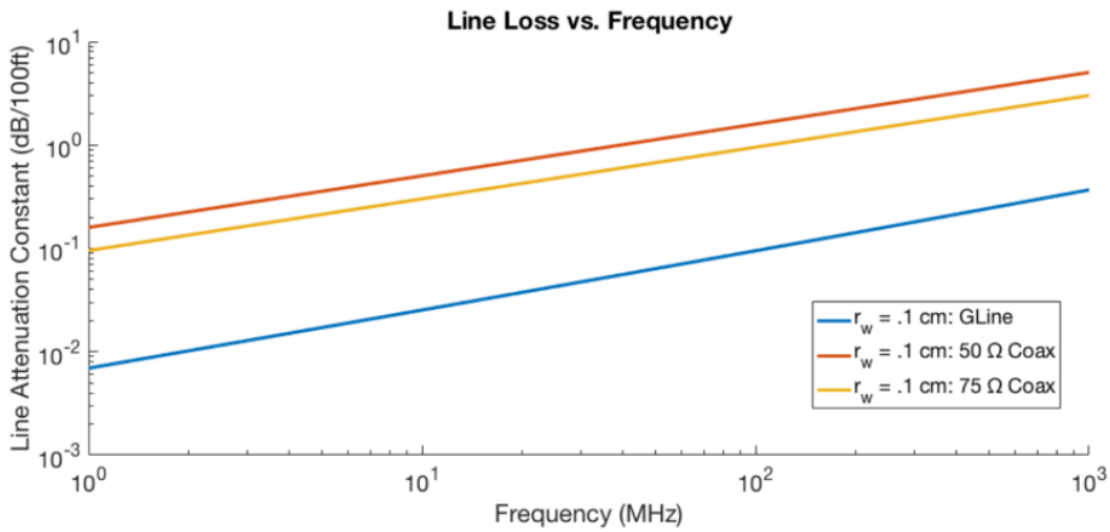

Fig. 3.9: Comparison of GLine attenuation to coax attenuation for 50 Ω and 75 Ω lines.

From Fig. 3.9, it is clear that the ohmic loss on the GLine is substantially less than that of a coax, which is justified by the lower GLine current magnitude coupled with the fact that the GLine has not current return path. Indeed, this property is quite advantageous and signifies the GLine's potential utility as a transmission line.

3.7 Guide Wavelength and Velocity

The GLine wave phase and group velocities velocity may be determined for the real part of the propagation constant using the following relations:

$$v_{phase} = \frac{\omega}{Re(h)}, \tag{3.59a}$$

$$v_{group} = \left(\frac{dRe(h)}{d\omega}\right)^{-1}. \tag{3.59b}$$

These velocities, normalized by the vacuum speed of light, are plotted in Fig. 3.10. As this plot indicates, both the phase and group velocities of the GLine wave are approximately the speed of light when the center conductor is bare.

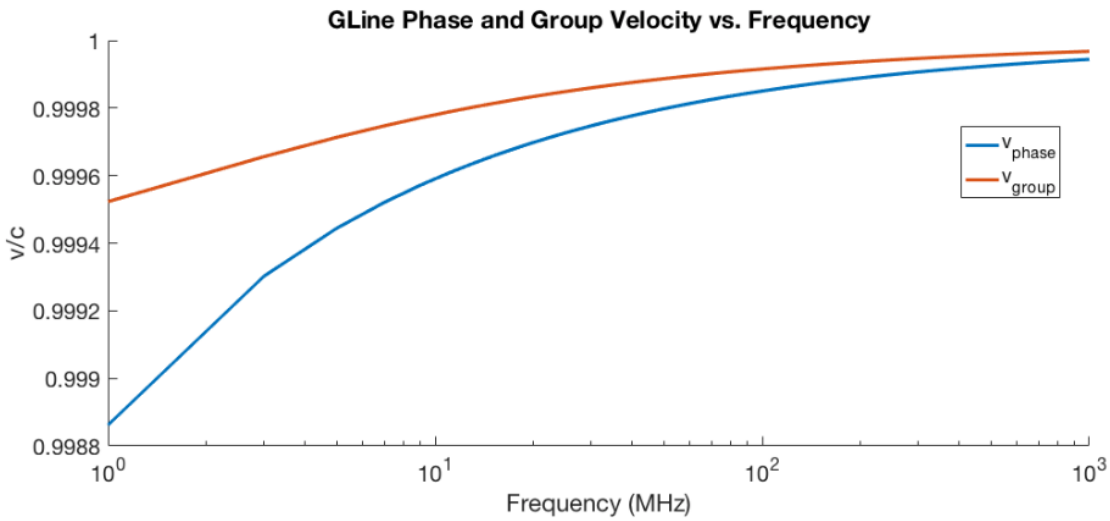

Fig. 3.10: GLine phase and group velocities as a function of frequency.

The guide wavelength is defined in terms of the real part of the longitudinal propagation constant and can be expressed as follows:

$$\lambda_g = \frac{2\pi}{Re(h)}. \tag{3.60}$$

Using this equation, we may plot the GLine's guide wavelength normalized by the free space wavelength as a function of frequency. This is done in Fig. 3.11 below:

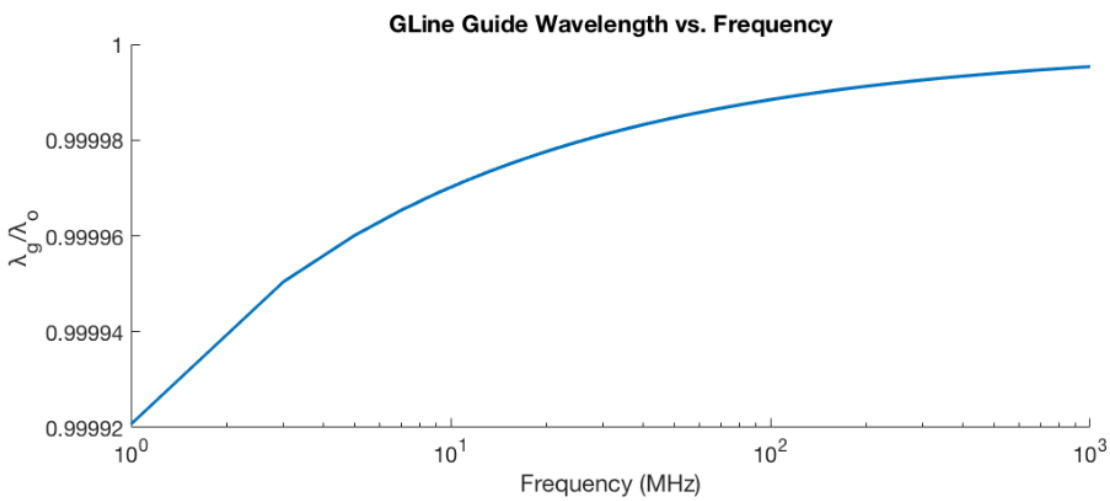

Fig. 3.11: GLine guide wavelength as a function of frequency.

As expected, there is very little deviation between the guide wavelength and the free-space wavelength, meaning the GLine electrical length may be treated identically to electrical length in free space.

3.8 Additional Current and Loss Comparison Data

In this section, a more comprehensive dataset for comparison the current and loss characteristics of the GLine to those of coaxial cables is given. Namely, the ratio of GLine ohmic current to the Ohmic current of a coax with the same inner conductor radius is presented, as well as the attenuation is dB/100ft of a signal carried by the GLine versus a signal carried by comparable coaxial cables. This data is shown in the figures below:

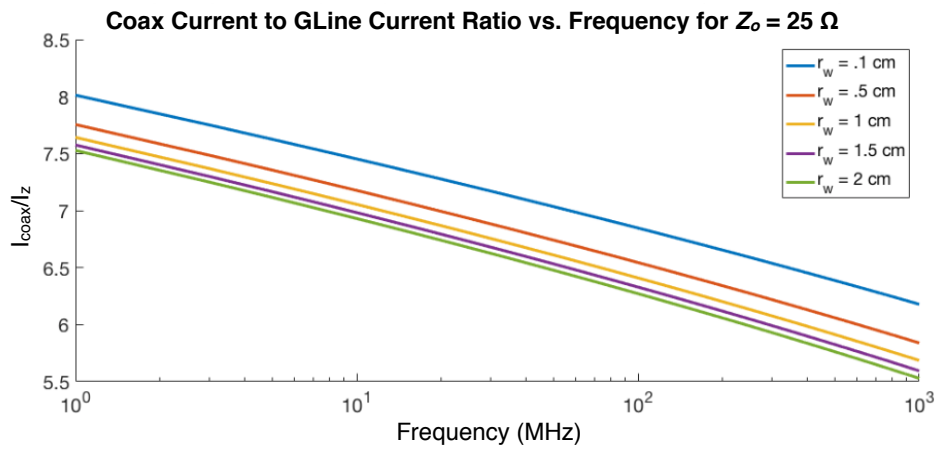

(a)

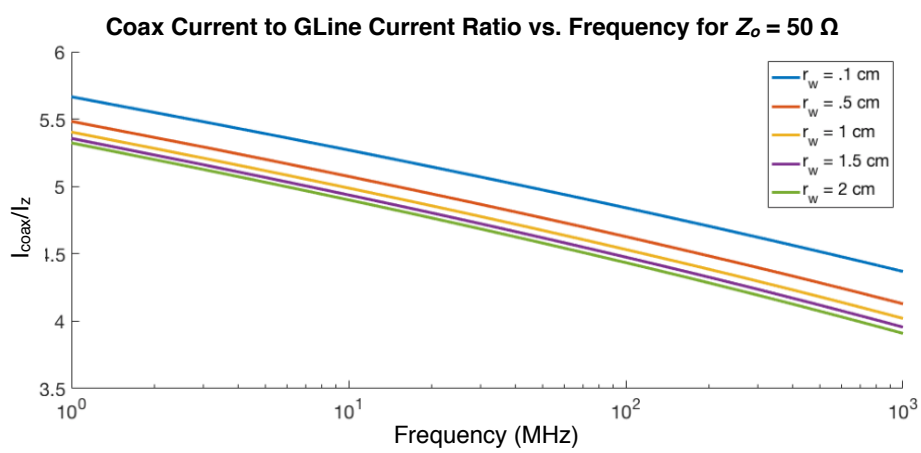

(b)

Fig. 3.12: Ratio of GLine ohmic current to coax current for a coax Z_0 of (a) 25 Ω, (b) 50 Ω, (c) 75 Ω, (d) 100 Ω, (e) 125 Ω, and (f) 150 Ω.

Fig. 3.12 continued

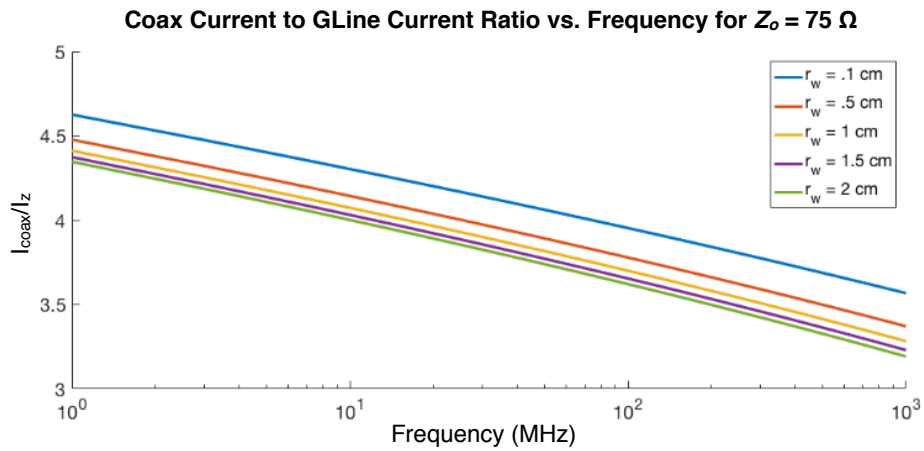

(c)

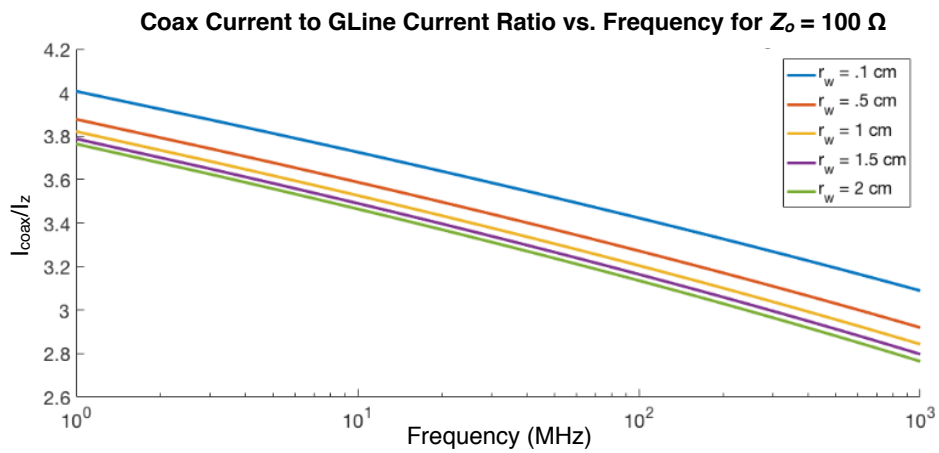

(d)

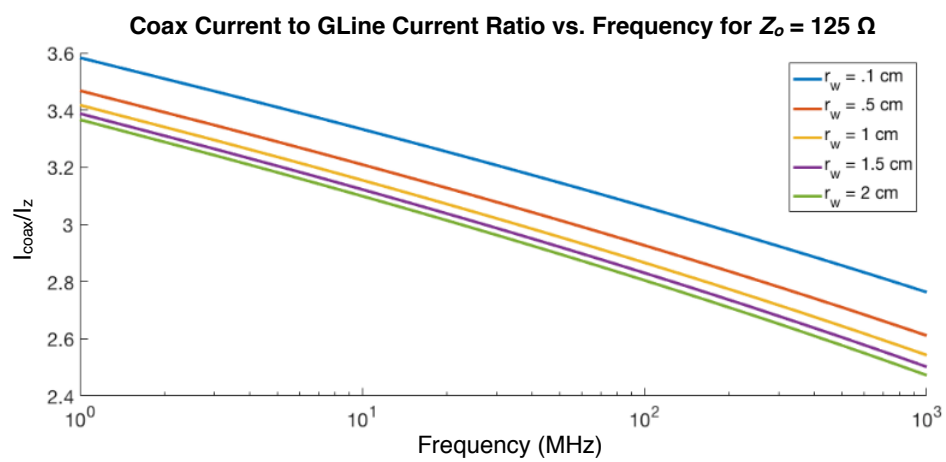

(e)

Fig. 3.12 continued

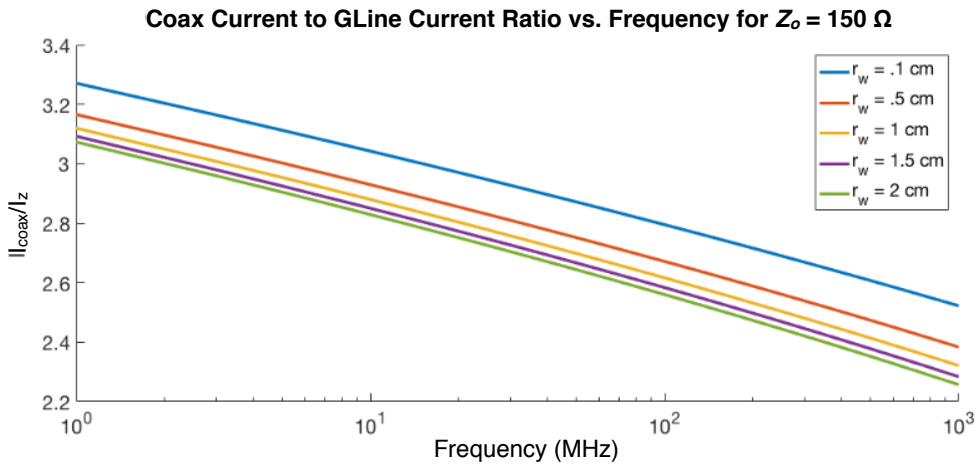

(f)

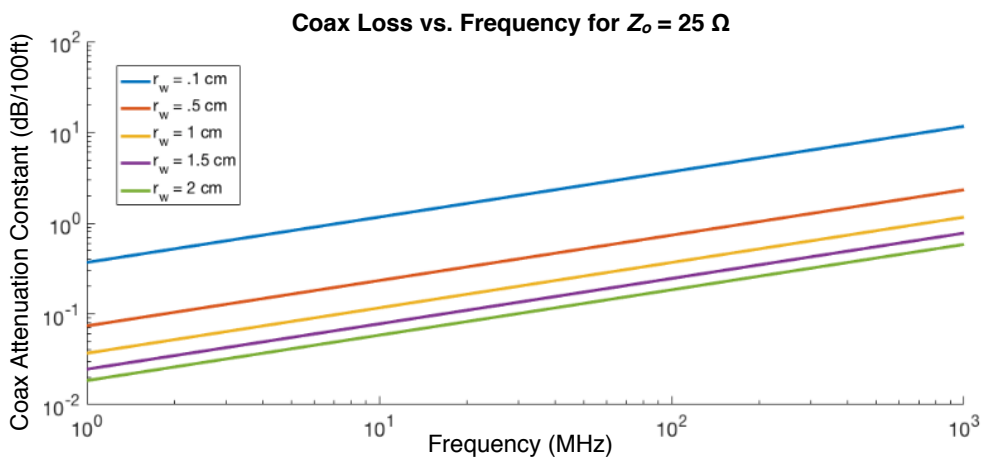

(a)

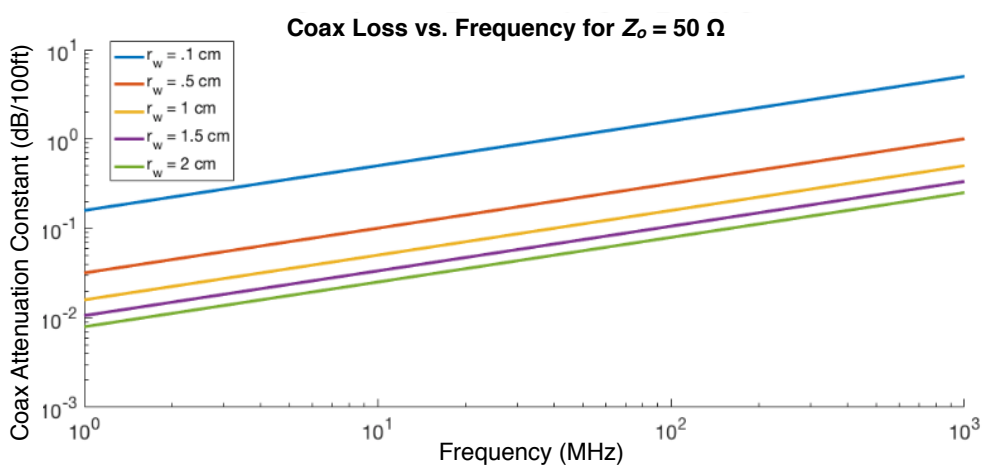

(b)

Fig. 3.13: Air-dielectric coax attenuation constant for a coax Z_0 of (a) 25 Ω, (b) 50 Ω, (c) 75 Ω, (d) 100 Ω, (e) 125 Ω, and (f) 150 Ω.

Fig. 3.13 continued

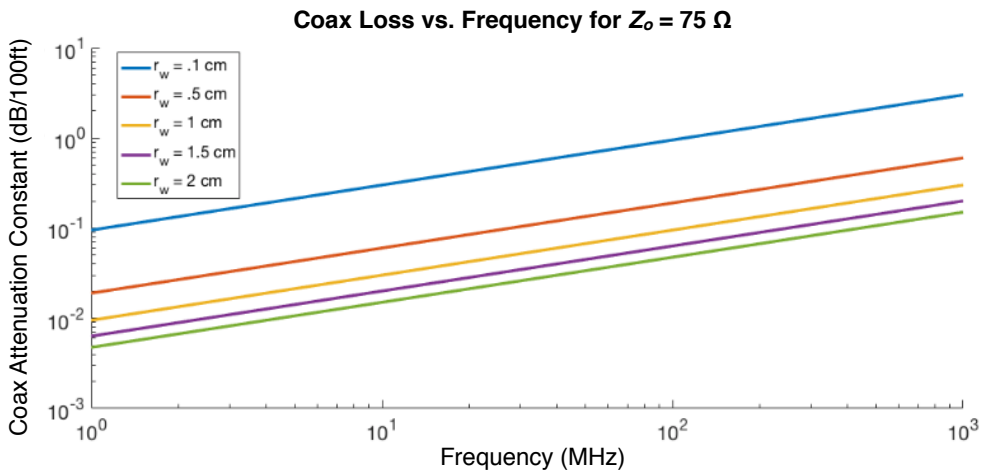

(c)

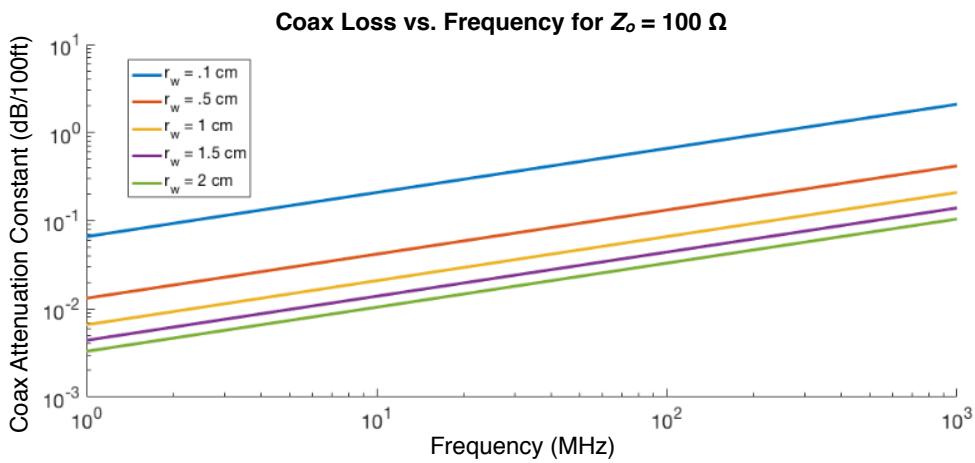

(d)

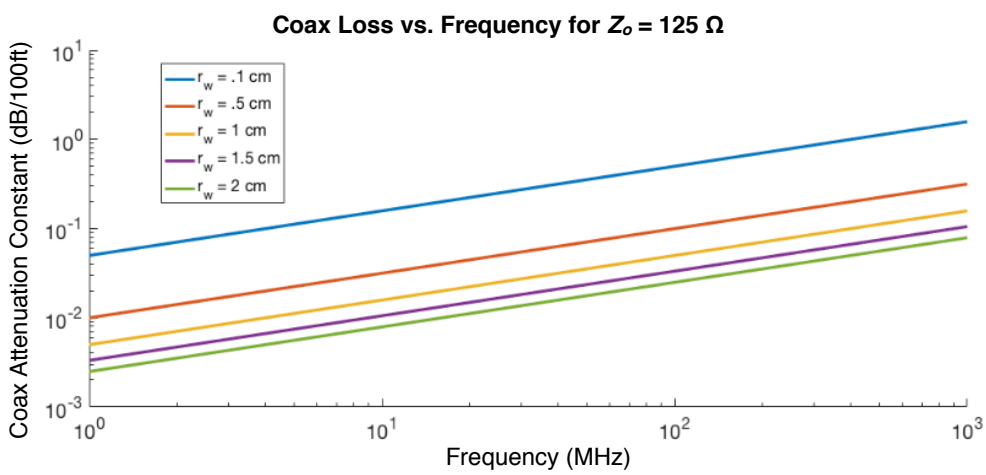

(e)

Fig. 3.13 continued

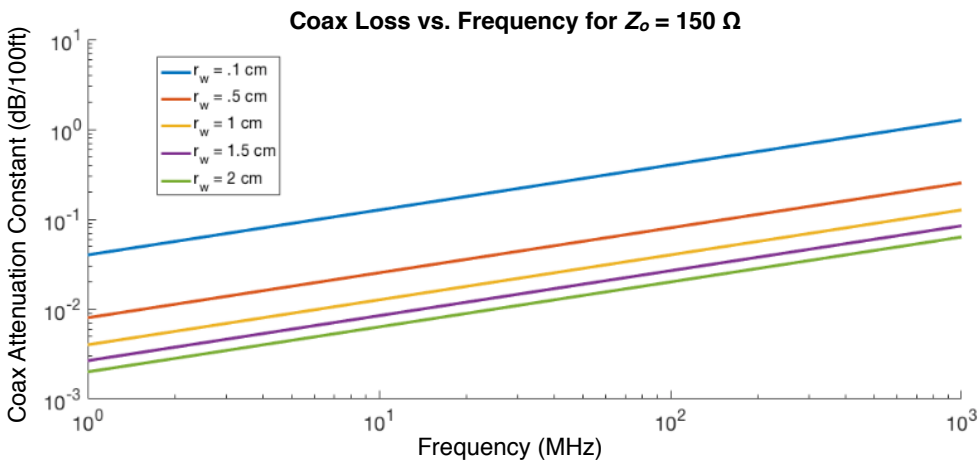

(f)

3.9 Conclusions

In this work, the GLine's computational modal solution and favorable properties were established and justified. It was shown mathematically that fields fall-off as 1/r and that the mode is non-radiative. The GLine ohmic current was also discussed as well as an equivalent TEM formulation that can be used to compute its effective characteristic impedance and loss properties. Furthermore, all of this was done using a superior computational method compared to the one used previously. With this, it is clear that the GLine is deserving of use in transmission line applications. In the next chapter, the presentation of the GLine's first application to the WPT regime will be given.

4. FIRST-GENERATION GLINE WIRELESS POWER SYSTEM

In this chapter, the first GLine WPT system detailed in [28] will be discussed. It will begin by laying out the the design a GLine-Based WPT transmitter, and follow with the considerations of the receiver used when testing the prototype. Finally, the performance metrics of the system, which operated at 80 MHz, will be presented and discussed.

4.1 Transmitter Design

While the geometry of the GLine is simple in concept, exciting the TM mode on the single wire from the TEM mode of the input presents complication. This is because the signal has to transfer from a structure with a ground path in close proximity to the signal path (assuming a conventional transmission line feed) to a structure with no ground path at all. A transition structure is necessary to facilitate this. From here in, these transitions will be referred to as "launchers". There are several types of launcher options for exciting the GLine TM mode, including the planar launcher, the conical launcher, and the quarter wave coax [19], [29]-[30]. The only launcher to be considered herein is the planar variety, as it is the simplest to implement and has the smallest longitudinal profile (the longitudinal direction is the axis of the line center conductor). The GLine transmitter prototype discussed in this chapter consists of two planar launchers affixed to the ends of a conducting cylinder. Below, a model generated in ANSYS HFSS is illustrated.

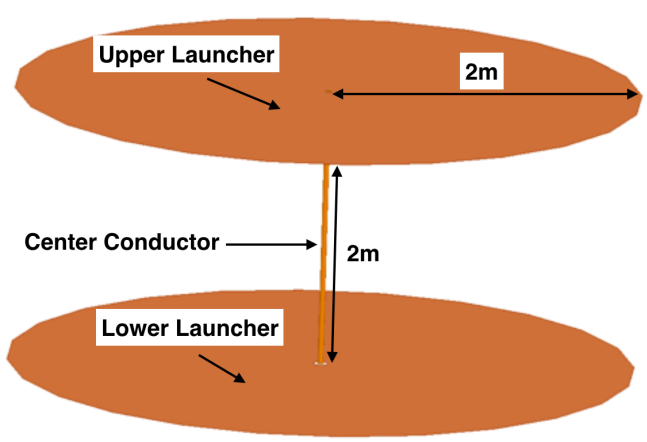

Fig. 4.1: GLine transmitter model.

The launchers in the design pictured above play two roles; field launching and field containment. Eqns 1.1a-1.1c describe a wave propagating in the z-direction, but this is for the case of an infinitely-long cylinder. For practical application, the fields must be terminated at some point. This termination can be either resistive or reactive in nature. However, resistive terminations contribute unnecessary loss to the system which can compromise power transfer efficiency. Furthermore, the termination structure must be such that most of the field energy (which extends out to infinity) is not lost at the termination interface. With these considerations in mind, a short termination was chosen for this design. Because a short is a reactive extreme, no power incident on the termination launcher is dissipated and most of it is reflected back down the line. There is, however, still field scattering at the launcher interface since its size is finite and the GLine fields extend to infinity. The larger the launcher, the more the fields are contained. This factor also plays into the selection of a short termination as opposed to an open one. A short termination forces a null E-field boundary condition on the launcher interface, which reduces launcher scattering loss considerably. If the line length is chosen such that the E-field at the input launcher interface is also forced to zero, then the loss on the GLine due to scattering will be minimized. It should be noted that such a length would technically be a “resonant” length, but the coupling to the receiver to be discussed below is not resonant in nature. In fact, any other length could be chosen if higher degrees of scattering loss can be tolerated or circumvented and the GLine transmitter would still function as normal. This means that choosing a “resonant” line length is incidentally advantageous from a scattering perspective, but is not a stark requirement for the system to function well, and detuning from the frequency at which the line is resonant does not compromise the system performance.

A consequence of having a reactive termination is the generation of a standing wave distribution on the line. If the termination is a reactive extreme, then the standing wave will consist of a distribution of E-field and H-field peaks and nulls along the line that are 90° out of phase. This is important for receiver placement, as if a receiver is purely electric or magnetic in nature, it cannot be placed in a position where the respective E-field of H-field is null. To demonstrate an example standing wave distribution, in the following figure, the standing wave distribution along the GLine is pictured for a line that is 1.5 wavelengths long with a short termination:

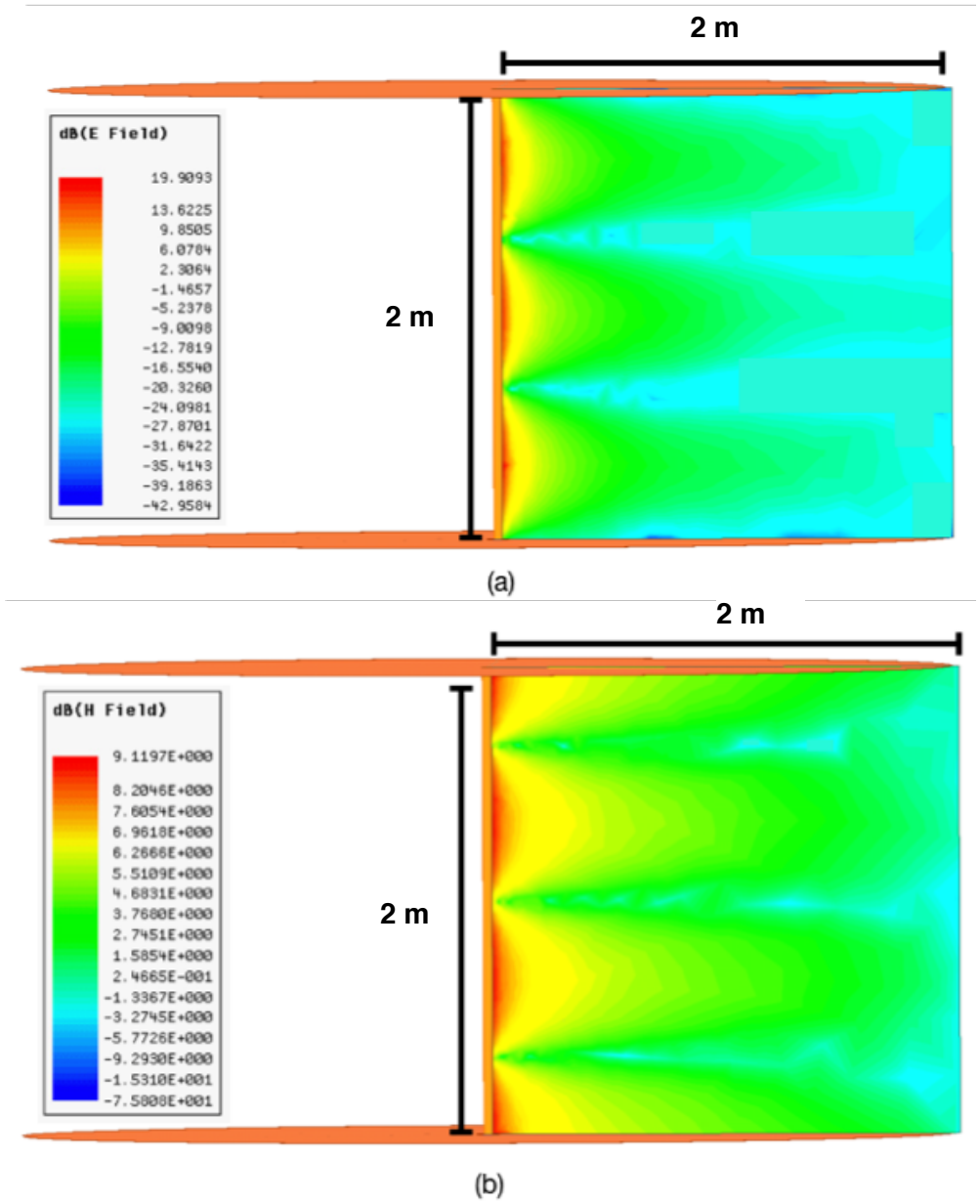

Fig. 4.2: (a) Shorted GLine transmitter radial electric field magnitude distribution with 225 MHz, 1 mW incident power. (b) Shorted GLine azimuth magnetic field magnitude distribution with 225 MHz, 1 mW incident power.

As can be seen in Fig 4.2, the E-field is zero at the launcher interfaces and maximized halfway up the line. Because of this, the standing wave nature of the design needs to be considered when designing the line dimensions.

From the transmitter depictions above, it can be seen that the launcher area is quite large, creating concerns about the practicality of a real implementation. However, this concern can be alleviated by integrating the transmitter structure into the room it is placed in. That is, by embedding the lower launcher into the floor and the upper launcher into the ceiling, the larger launcher area can be effectively ignored. Furthermore, the center conductor need not be placed in the middle of the room and the launchers need not be made up of solid discs, but can be implemented using wire meshes instead (this particular point is expanded upon in Section 5.7 in the next chapter). Below, a mock-up of the GLine transmitter room integration concept is shown.

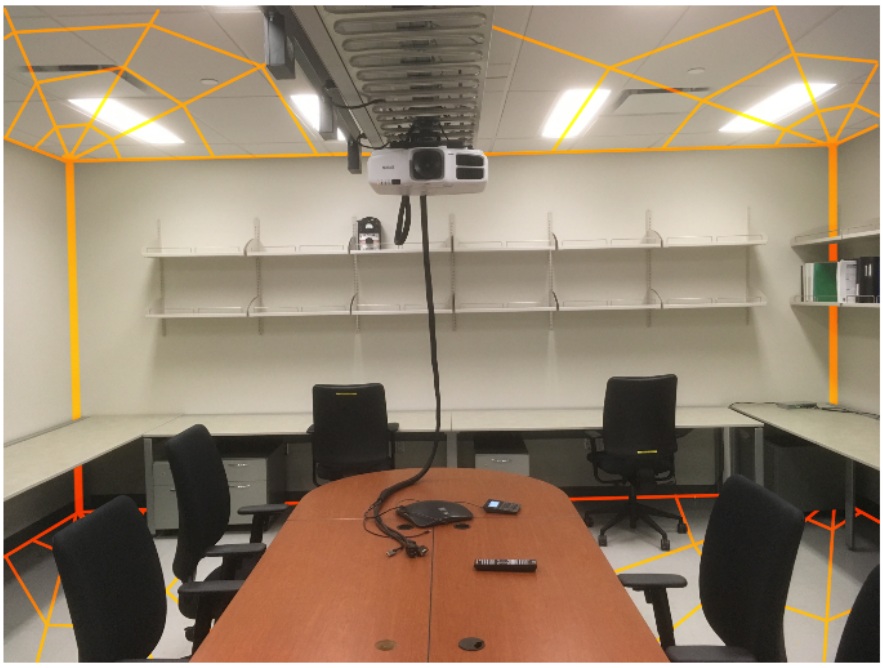

Fig. 4.3: Conceptual drawing demonstrating how two GLines could be placed at the two corners of the room. The figure displays the ground planes as wire meshes.

For the purposes of practical implementation, the setup in the figure above would be sought. For proof-of-principle, however, the lower level design shown in Fig. 4.1 will be investigated. In the next section, the receiver design choices for the first GLine prototype will be discussed.

4.2 Receiver Design

The receiver for this prototype was chosen to couple off of the GLine electric fields only since, given the termination, line dimensions, and chosen frequency of operation (which is 80 MHz, a choice that will be detailed below when the system results are discussed), an electric field peak would be present approximately halfway up the line (this was the desired receiver position.) To facilitate electric coupling, the directionality of the receiver's excited current distribution must align with the GLine's radial field polarization (note that, if evaluated, the longitudinal z-directed E-field is orders of magnitude weaker than the radial E-field in the GLine distribution solution). The simplest structure that would accomplish this would be a wire dipole, which served as the foundation for this system's receiver. However, a receiving antenna with a wider coupling area would be able to collect more energy from the GLine field. With this in mind, a bowtie-like structure was devised, which can be thought of as a cluster of wire dipoles with common terminals to increase coupling strength. This receiver is illustrated below:

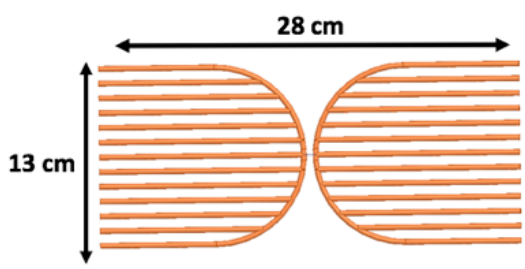

Fig. 4.4: Wire bowtie antenna receiver topology.

Note that at 80 MHz (at which the free-space wavelength is 3.75 m), this receiver is electrically short. This is by design, as electrically large receivers become their own local scatterers in the presence of GLine fields, which reduces efficiency. On the other hand, the receiver should not be too electrically short, as a highly reactive receiver is difficult to match to efficiently and the reduced coupling area harms efficiency. In the next section, the impedance-matching network design will be discussed.

4.3 Impedance-Matching

In order to direct power efficiently from the transmitter to the receiver, transmitter input and receiver output impedance matching networks are required. Without them, the majority of the incident power on the input or output interfaces will be reflected. Since the transmitter and receiver are coupled electromagnetically, their input impedances are dependent on the receiver position. For this system, the matching circuits were static, meaning that the matching could only me optimized for one position and frequency. In this case, the chosen position was for the receiver to be placed halfway up the line in the longitudinal direction and 0.5 m away from the center conductor in the radial direction (this will be illustrated in the next section). Once a position is chosen, impedance matching circuits are derived by extracting the Z-parameters from the system (by treating the system as a two-port network) and using numerical optimization code as well as the relationship between Z-parameters and S-parameters to back out the impedances that the transmitter input and receiver output should be matched to. This technique derives the system's ideal "output impedances", i.e., the impedances the transmitter input and receiver output should see looking outward. The matching circuits then match nominal 50 Ω impedances to these output impedances. To do this, simple LC matching circuits were used. In the next section, the results of the first GLine prototype will be discussed.

4.4 System Results

A GLine transmitter prototype with a launcher radius of 2 m was constructed. The launchers were crafted using cardboard sheets with copper foil affixed to them. The center conductor had a length of 2 m and a radius of 2 cm. A receiver was placed on a 1 m tall stand and positioned 0.5 m away from the center conductor. Impedance-matching (IM) parameters were computed using the optimization technique discussed above and LC matching circuits were placed at the transmitter input and receiver output. The frequency of operation was 80 MHz, meaning the line was approximately a half-wavelength long. This was the frequency around which the scattering loss of the system was minimized when a short termination (which was implemented by taping the copper foil on the upper launcher to the center conductor) was used. The input was implemented

by soldering the center probe of an SMA connector to a small sheet of copper foil and wrapping it around the center conductor of the GLine, while soldering the SMA ground to the copper surface of the lower launcher. Below is a block diagram of the system as well as an image of the measurement setup.

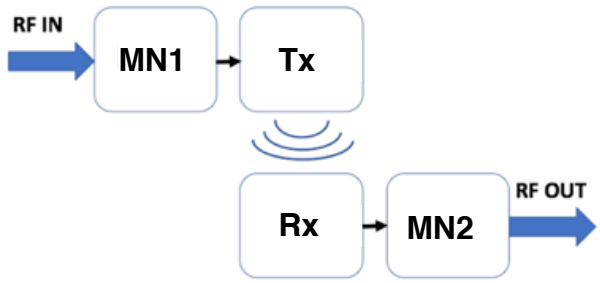

Fig. 4.5: WPT block diagram.

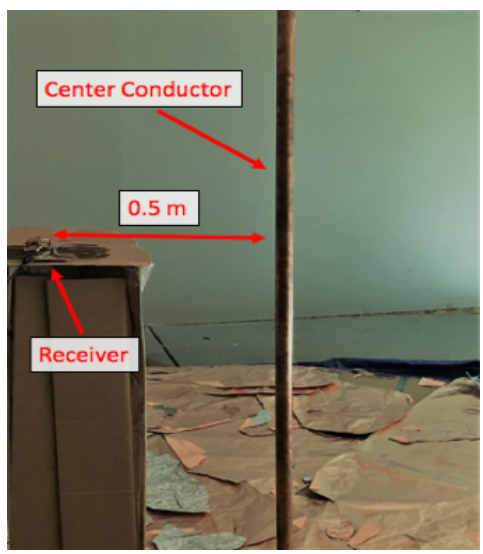

Fig. 4.6: GLine experimental setup.

The prototype performance was measured by extracting the S_{21} of the system (where port 1 is the transmitter input and port 2 is the receiver output). The S_{21} value is defined as the "RF efficiency", i.e., the efficiency of the RF signal from the transmitter's IM network input to the receiver's IM network output. Below are the simulated efficiency results of the built system, as well as the measured performance.

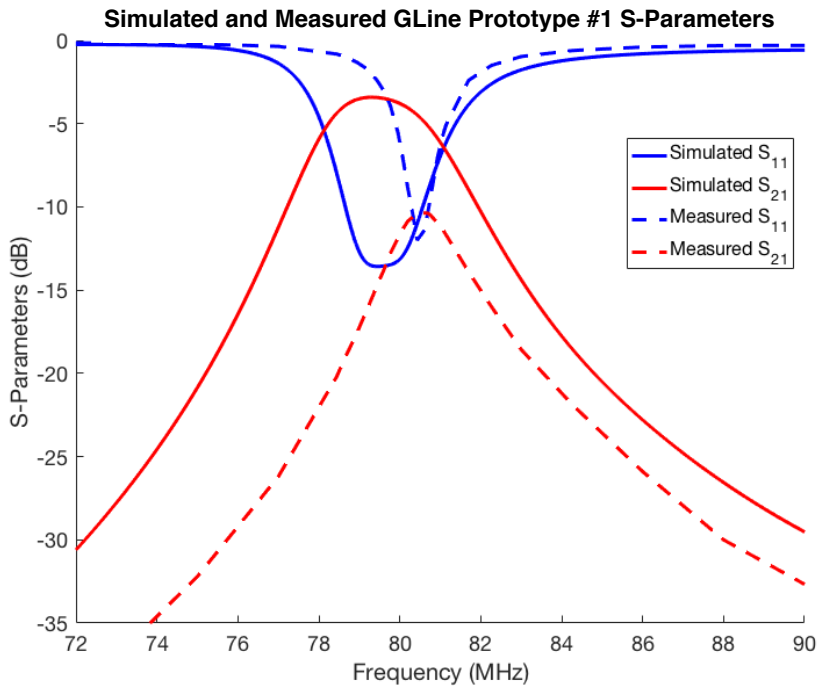

Fig. 4.7: Simulated and Measured GLine system S-parameters.

From the figures above, it can be seen that there is substantial degradation between the simulated and measured performance. This is for a number of reasons. Firstly, the simulated launchers were modeled as flat, solid copper discs, whereas the constructed system's launcher were made of cardboard and thus was subject to bending. This meant that the upper launcher was not flat like the ideal case, and thus reflected a significant deal of energy out of the transmitter area. Secondly, the receiver joints were soldered together to create the desired antenna shape, but the wires were thicker than many conventional wire antennas, and this thickness (which was chosen to facilitate greater current excitation) made soldering difficult, as it was challenging to heat the wire surface through enough to melt the solder and create good joints. Because of this, each solder joint was non-negligibly lossy, reducing the system efficiency. Finally, the copper foil sagged in places on the upper launcher, and was not as even as it would have ideally been overall. This exacerbated scattering issues. Despite this, however, the prototype served as a sufficient proof-of-concept experiment for the GLine WPT system, and indicated enough merit to continue development.

4.5 Conclusions

In this chapter, the first prototype of the GLine WPT system was defined and discussed. Using this system an RF efficiency of 10% at 80 MHz was achieved from a receiver positioned .5 m away from the center conductor of the prototype, marking a viable proof-of-concept design. In the next chapter, an improved, more in-depth prototype will be evaluated.

5. SECOND-GENERATION GLINE WIRELESS POWER SYSTEM

This chapter will discuss the second GLine prototype conceptualized in [31]. The principles of its design were nearly identical to those of the first prototype, but, as is shown below, its implementation was significantly superior. The structure of this chapter will follow that of the one previous, with a discussion of the transmitter design, followed by the receiver and IM networks. The chapter will conclude with the second prototype results, which contain performance metrics more varied than than the system response of one receiver at one position. In particular, multiple receivers at multiple positions were measured and a rectification block was also incorporated into system. This will be discussed more in detail below.

5.1 Transmitter Design

For the second prototype, instead of cardboard, plywood was chosen as the material with which to construct the GLine launchers, which were still designed to be planar. Additionally, a wooden frame was constructed to keep the upper launcher well-supported and level. Copper foil was still used to make the launcher surfaces conductive. The height of the launcher was 2 m like the first prototype, but the launcher radius was reduced to 1.22 m due to space constraints. Below, the second transmitter prototype is illustrated:

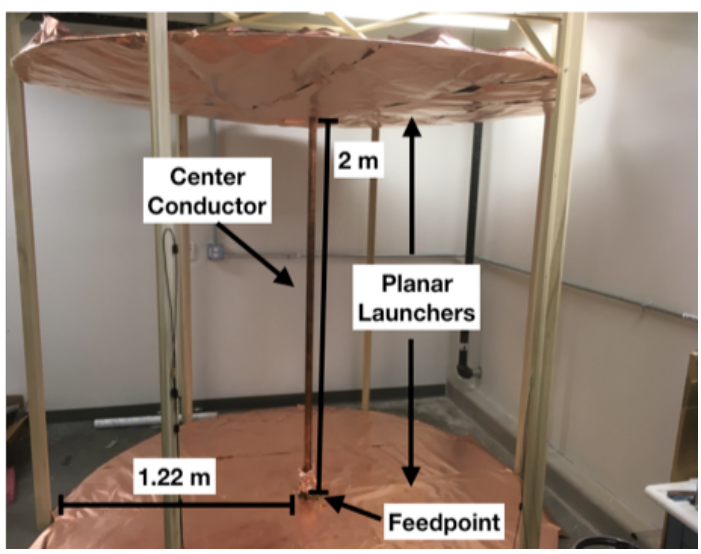

Fig. 5.1: Updated GLine transmitter prototype.

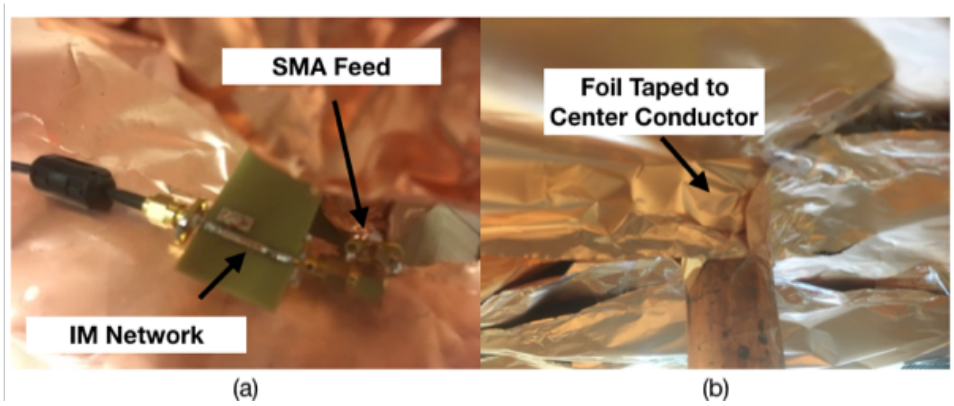

Fig. 5.2: (a) Updated GLine transmitter feed and (b) short implementation.

It should be noted that there is a cluster of copper foil wrapped around the bottom of the center conductor. Doing this was found to reduce losses by limiting the radiation due to the modal transformation from TEM to TM (it is not immediate; there is a region near the launcher interface where the wave is not fully TEM or TM). It should also be noted that the launcher surfaces are more uniform and less rough than those of the first prototype. As a side note, the wooden frame should not affect the GLine performance according to simulation. The GLine input and short were implemented the same way here as in the first prototype.

5.2 Receiver Design

The bowtie-shape idea behind the first prototype's receiver was kept for this one, but the implementation was changed from a wire design to a planar one. This removed the solder joint issue noted in the previous chapter, as well as added surface area for current excitation. Furthermore, given the choice of substrate, using a planar design allows for more tight impedance control, which is helpful for impedance-matching. Again, the the receivers here were designed to couple electrically to the GLine and will be placed roughly halfway up the line as before (though the frequency of operation was changed for this prototype as will be detailed below). The following figure shows the design for the primary receiver antenna used in the second prototype system:

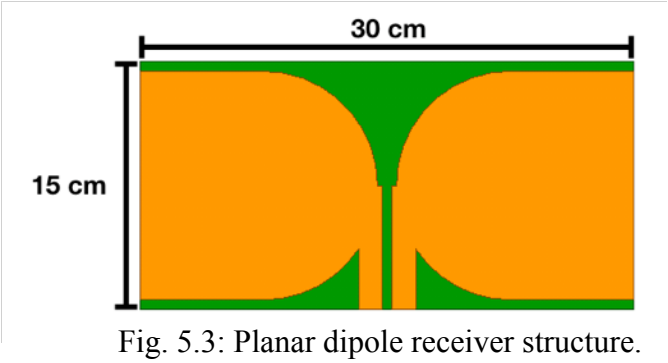

Fig. 5.3: Planar dipole receiver structure.

Note that the antenna is only one layer and the underside has no copper.

5.3 Impedance-Matching

The method discussed in the previous chapter was used to generate impedance matching circuits for this prototype, though more emphasis was placed on choosing high-Q components (particularly inductors) to minimize IM network loss. Additionally, another technique for designing IM networks was also utilized wherein, instead of designing the networks simultaneously, the networks were created sequentially. Specifically, the input impedance of the receiver was matched to 50 Ω by itself with no transmitter coupling and then placed in the position within the transmitter where optimum coupling is to be obtained. Then, the input impedance of the transmitter input is measured while the receiver is in position and terminated with a 50 Ω load. This input impedance is then matched to 50 Ω, completing the IM network design. Often, this method and the optimization method yield similar results, though the former is simpler and the latter is more general. It will be specified which method is used for which experiment when the second prototype results are discussed. For reference, the optimization will be called IM method #1 and the method detailed in this section will be IM method #2. Note LC matching networks were the chosen circuit topology for this prototype as before.

5.4 Rectification

For this prototype, a rectification block was included to create a usable DC output from the GLine system. The rectifier consisted of a low-pass filter (to suppress harmonic reflections from

diode non-linearity), a half-wave rectification bridge, and impedance-matching circuitry. The design is examined in more detail in [32].

5.5 System Results

The measurement procedure for this prototype was very similar to that of the last one, except the system was optimized for a 233 MHz frequency of operation instead of 80 MHz (as the second prototype transmitter response was superior at that frequency than at 80 MHz) and substantially more data was taken. Particularly, instead of taking data for one point only, efficiency data was gathered for a range of distances from the center conductor. Additionally, multi-receiver experiments were run and the entire area around the center conductor was utilized to show the cylindrical symmetry of the system (which is apparent from the field equations). In the following sub-sections, the results of all the second prototype experiments will be presented.

5.5.1 One-Receiver Data

The receiver structure pictured in Fig. 5.3 was fabricated on 1 mm thick FR4 substrate and positioned halfway up the line as before. This time, however, the distance between the center conductor and receiver was swept from .25 m to 1 m. Below, the measurement setup for the one-receiver experiment is shown. Note that the coaxial cables were calibrated out of all measurements.

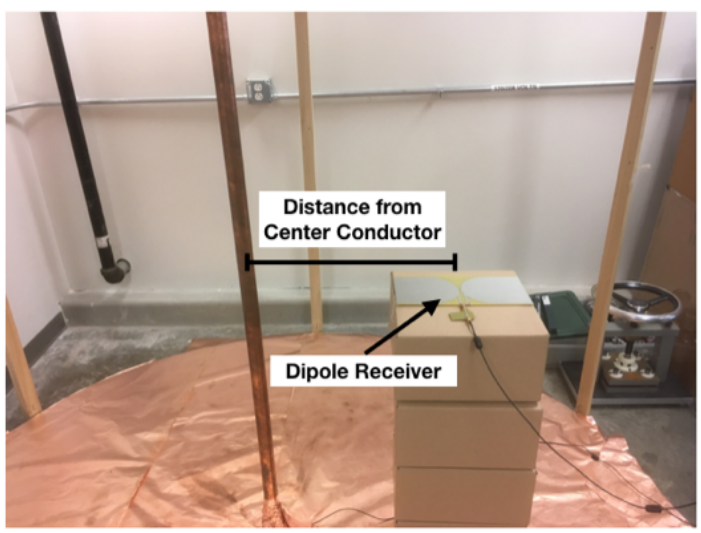

Fig. 5.4: One receiver measurement setup.

Again, after the IM networks were designed (here, they were optimized for a 233 MHz signal at a position that is .5 m away from the line center conductor), the transmitter input and receiver output were connected to a VNA through coaxial cables such that the RF efficiency could be extracted. With the receiver positioned halfway up the line, the RF efficiency was measured at distances ranging from .25 m to 1 m. While the system was optimized for 233 MHz signals, the performance was also measured at multiple other frequencies around 233 MHz. Note that the orientation of the receiver antenna as shown in Fig. 5.4 was kept constant; this alignment was necessary to couple off of the GLine radial fields. Using the simulated Z-parameters of this setup, the system's C_t and k parameters (refer back to eqns. 2.37 and 2.38 in Chapter 2) were deduced as a function of the receiver's radial distance. These parameters are shown in Fig. 5.5. In Fig. 5.6, the RF efficiency data for the single receiver measurements is shown. The data on the plots is compared to the performance of the system simulated in ANSYS HFSS. As can be seen from the efficiency data, the measured RF efficiency falls off monotonically with distance, but stays above 30% for a 233 MHz signal at distances smaller than ~.6 m. At .5 m the RF efficiency is 35% for a 233 MHz excitation. It should be noted that the measured efficiency values are consistently lower than the simulated ones. This is primarily due to launcher surface non-idealities, as well as the effects of the surrounding environment imposing on
the GLine's scattering profile (wall and pipes are well within a wavelength of the transmitter).

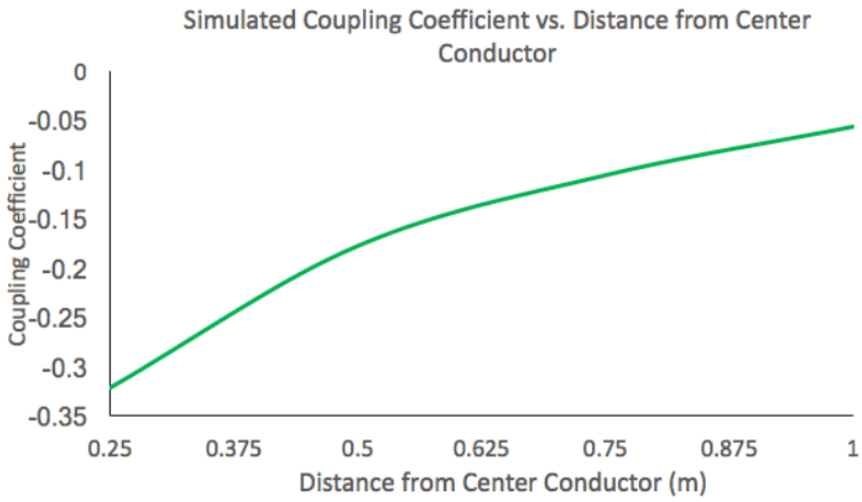

(a)

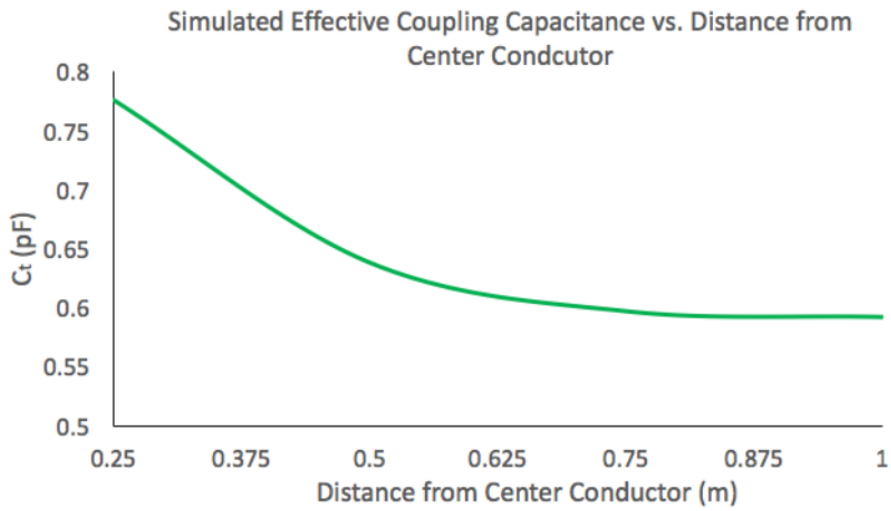

(b)

Fig. 5.5: (a) One-receiver simulated k as a function of radial distance and (b) simulated C_t as a function of radial distance.

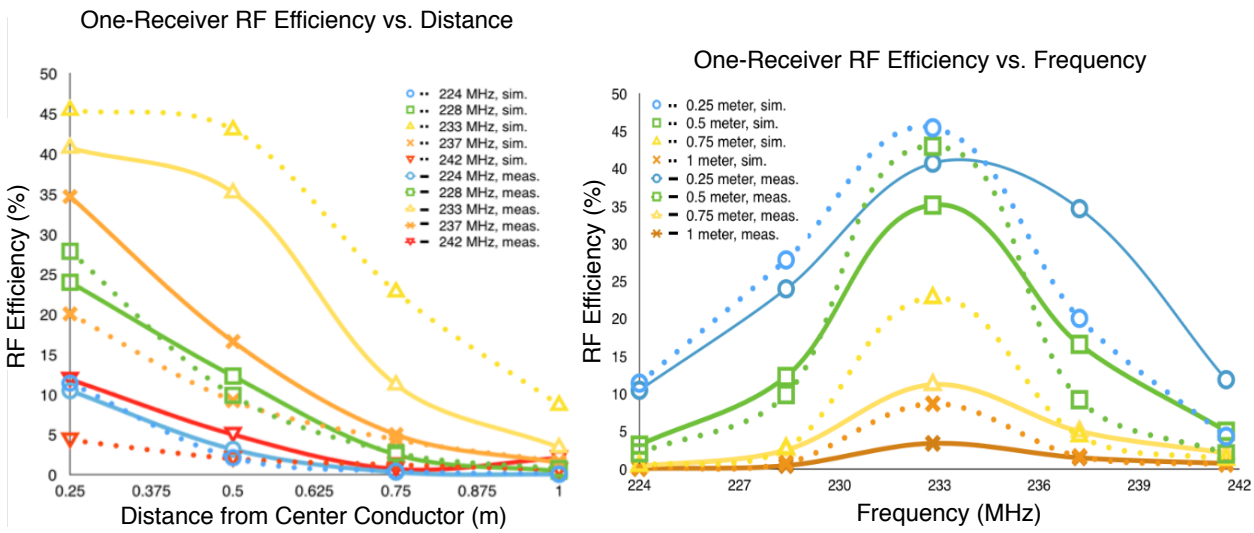

(a) (b)

Fig. 5.6: One-receiver simulated and measured RF efficiency as a function of (a) frequency and (b) distance.

Next, a set of tests were conducted that utilized the rectifier to generate a usable DC output. To do this, the coaxial cable that connects to the input of the GLine was connected to a signal generator and amplifier, and the output coaxial cable was connected to the rectifier through an RF coupler. The coupler sampled the rectifier input signal and ran it to a power meter such that the rectifier incident power could be determined. The coaxial cables were calibrated out of these measurements. Once the necessary connections were made, the overall system power efficiency (the efficiency from the transmitter input to the rectifier load) was measured for various input powers, receiver positions, and excitation frequencies. Below are plots describing these results, as well as a plot detailing the measured power efficiency of the rectifier by itself when an input signal is connected to it directly. From Fig. 5.7b, it can be seen that the system efficiency reaches 26% when the receiver is placed .5 m away from the center conductor and the incident power is optimal for a 233 MHz signal. This is consistent with the RF efficiency and rectifier efficiency (35% and 75% respectively) for this case.

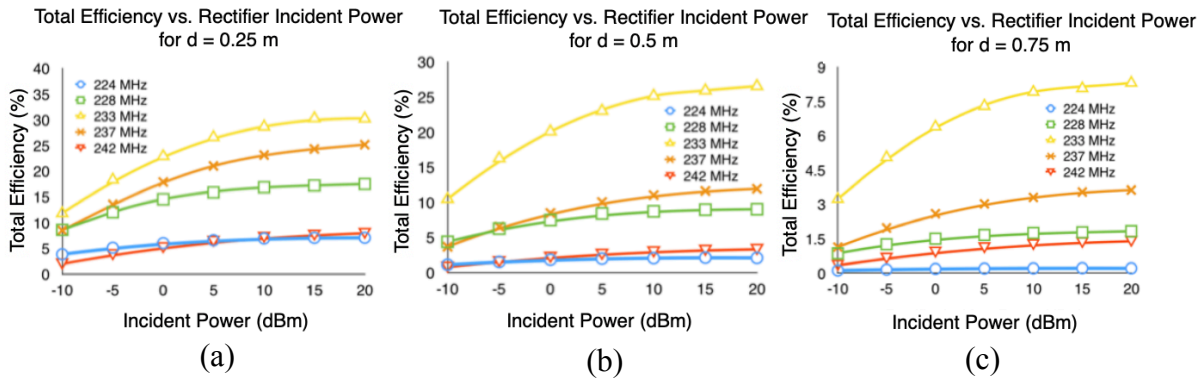

(a) (b) (c)

Fig. 5.7: One-receiver GLine system measured total efficiency for 0.25 m (a), 0.5 m (b), and 0.75 m (c) distances.

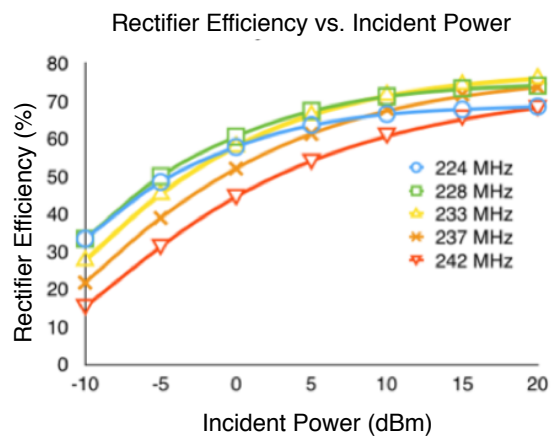

Fig. 5.8: Rectifier measured efficiency data.

This data indicates that the GLine system is feasible to generate useful levels of power at the load output of a receiver.

5.5.2 Two-Receiver Data

To further demonstrate the GLine's utility, a second receiver was measured simultaneously with the one discussed in the section above. This receiver had a structure identical to the first, but the substrate was constructed on 1.27 mm thick Rogers 5880LZ. It's own IM network was also created and optimized for a distance of .5 m away from the center conductor at 233 MHz. In addition to showing two-receiver functionality, the two-receiver tests were also designed to demonstrate the cylindrical symmetry performance of the GLine transmitter. This was done by sweep-

ing the azimuth angle θ of one receiver while keeping the other stationary with each receiver at a set distance from the center conductor. The figure below illustrates the measurement setup for the two-receiver/rotational symmetry experiment:

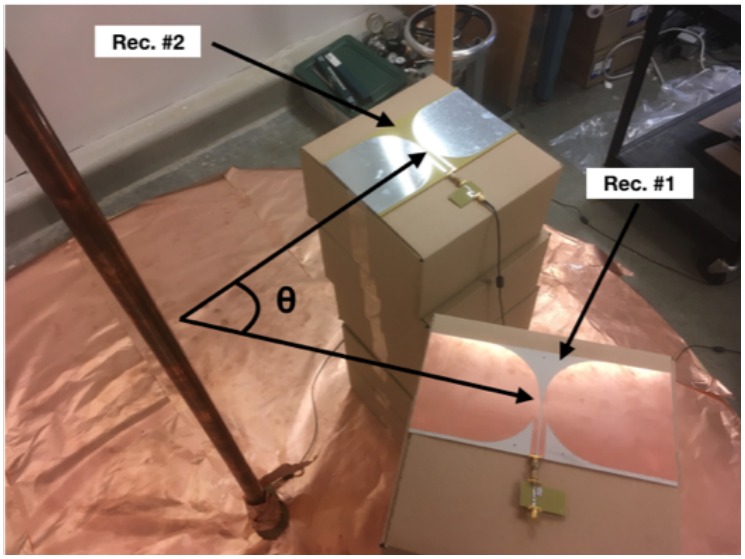

Fig. 5.9: Two-receiver measurement setup.

For each measurement case, the individual RF efficiency of each receiver was determined by measuring the S-parameters between the transmitter input and the output of one receiver while the other was terminated with a 50 Ω load. Note that the transmitter IM network was the same for these tests as it was for the one-receiver case. Two sets of data were gathered for these tests. The first set details the individual receiver efficiency data when the rotation angle θ is locked at 90° and the input frequencies and receiver distances from the center conductor are swept. The second set keeps the frequency at 233 MHz and sweeps the rotation angle of receiver #1 (the Rogers substrate receiver; see figure above) for different receiver distances from the center conductor, noting the individual RF efficiency of each receiver as well as the power split ratio between them (i.e., how much of the total power delivered to both receivers was devoted to each one individually). Note that both receivers are kept at the same distances from the center conductor at all times. Below, the results for the two-receiver tests are shown.

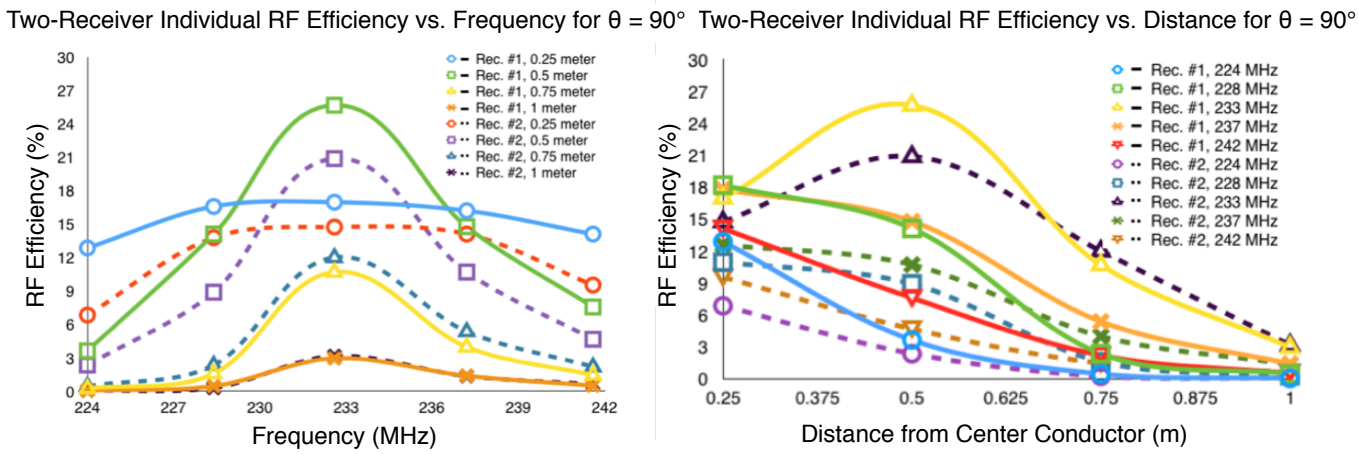

(a) (b)

Fig. 5.10: Two-receiver efficiency with respect to (a) frequency and (b) distance for θ = 90°.

From Fig. 5.10b, it can be seen that the total combined efficiency of the receivers approaches 48% when both are positioned .5 m away from the center conductor at 233 MHz. Note also that the efficiency is actually lower when the receivers are placed closer than this to the transmitter center. This is because, when the receiver antennas are close to the center and each other, there is significant cross-coupling between all three, which detunes the system impedances. This happens for the one-receiver case as well, but the increase coupling has a larger effect than the detuning does for that case, as opposed to here. If closer distances are desired, it is possible to tune the IM networks accordingly, but since all of the IM networks were optimized for a .5 m distance, the above behavior was observed.

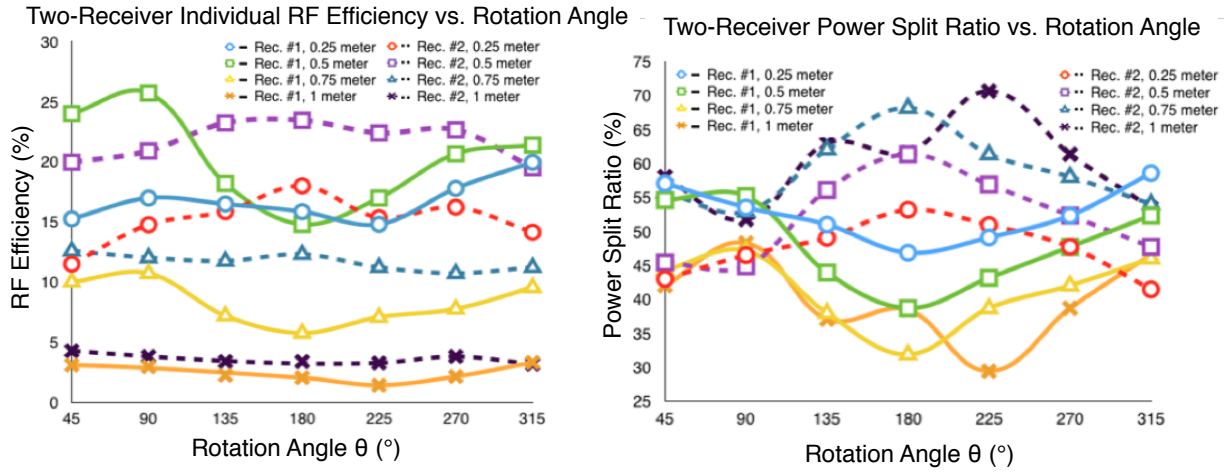

(a) (b)

Fig. 5.11: (a) Two-receiver RF efficiency and (b) power split ratio with respect to rotation angle at 233 MHz.

From Fig. 5.11, it can be seen that the receiver efficiencies vary as a function of rotation angle, but not by more than approximately 10%. While the power to receiver #2 is kept somewhat constant, the power to receiver #1 falls markedly when the rotation angle is between 90 and 270°. This is attributed to the transmitter position relative to the walls of the room it is place in. When receiver #2 is placed between the center conductor and these walls, both the field distribution and impedance matching are perturbed, dropping the effective coupling. This is supported by the fact that power transfer is maximized when receivers #1 and #2 are placed at 0° and 90° respectively, as these positions have no walls or pipes at the GLine outer perimeter. Even so, it is clear that the GLine distribution does not contain any cylindrical nulls and has a high degree of cylindrical symmetry.

5.5.3 Multi-Receiver Data

Theoretically, the amount of receivers that can couple to the GLine at once is unlimited. To demonstrate this principle, a multi-receiver experiment wherein 5 receivers of different sizes and positions were placed around the GLine and measured. Each had the bow-tie antenna structure but with varying dimensions. They included the two antennas from the experiments above, as well as three antennas fashioned using FR4 substrates and copper foil. Fig. 5.12 details this set-up.

The IM network of each antenna was tuned such that the return loss looking into each receiver output was at least 10 dB while each other receiver and the transmitter were terminated with 50 Ω loads. Additionally, the transmitter IM network was modified slightly to match the 50 Ω input port to the input impedance of the transmitter when all receivers were placed and terminated with 50 Ω loads. Below is a table detailing the efficiency, size, and position of each receiver. Like with the two receiver experiment, the efficiency of each receiver was determined by measuring the S-parameters from the transmitter to each receiver while all the others were terminated.

Fig. 5.12: Multi-receiver test setup.

Table 5.1
Multi-receiver experiment data

Receiver #	Size (cm^2)	Distance (m)	θ	RF Effic. (%)	Combined RF Effic. (%)
1	450	0.66	0	4.7	-
2	260	0.36	45	11.75	-
3	450	0.44	135	13.5	-
4	90	0.2	225	2.4	-
5	320	0.47	315	5.9	-
All	-	-	-	-	38.25

From the table, it can be seen that the antennas received different degrees of power and the efficiency of each was highly dependent on position and size, but with varying importance placed on each parameter. For instance, receiver #3 was large, relatively isolated from the other receivers, and placed not too far away from the transmitter center, so it collected the most power out of all the receivers. On the other had, receiver #1 was placed farther away and had two other receivers competing for power in its coupling area, each positioned closer to the middle than itself, so it received substantially less power. All of these factors need to be accounted for if an equal power

split is desired for instance, but the in-depth examination of these factors is beyond the scope of this work. Nevertheless, as can be seen from the table, a 38% combined efficiency was achieved, which is an improvement over the single receiver case at .5 m.

5.6 Mesh Launcher Analysis

While the discs that make up the GLine transmitter launchers are solid, it is feasible to create them by using wire meshes instead. Using wire meshes instead of solid discs decreases the amount of necessary material, meaning system cost is also reduced. Further, using this method decreases construction complexity as well. However, using a wire mesh instead of a solid disc increases the amount of scattering leakage, as the launcher interface has a conductive sheet replaced with an aperture. We may conduct a simulation analysis to determine the effects of this and the feasibility of this kind of launcher construction. This study is done using HFSS. Below, Fig. 5.13 shows the design of such a structure with a shorted termination. Here, the launchers are formed by a series of concentric rings connected by a star formation of conductive strips. In the study, the spacing between the rings was swept between 15 and 100 cm. If the radius of a ring exceeded 2 m, the ring was omitted from the launcher. The inner-most ring had a radius that was twice the ring spacing, meaning that fewer and fewer rings were included as the ring spacing increased. For each configuration, RlTL at 225 MHz was extracted. In Fig. 5.14, the simulated RlTL for each ring spacing is plotted compared to the RlTL value of the constructed prototype, which was approximately 3.5 Ω. Fig. 5.15 shows the number of rings included for each ring spacing.

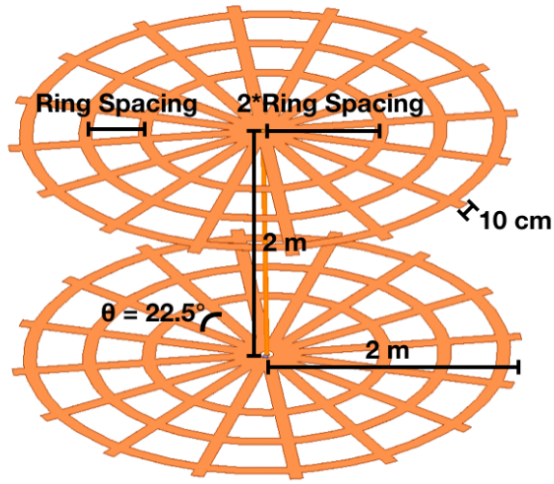

Fig. 5.13: GLine Transmitter with mesh launchers; three rings shown.

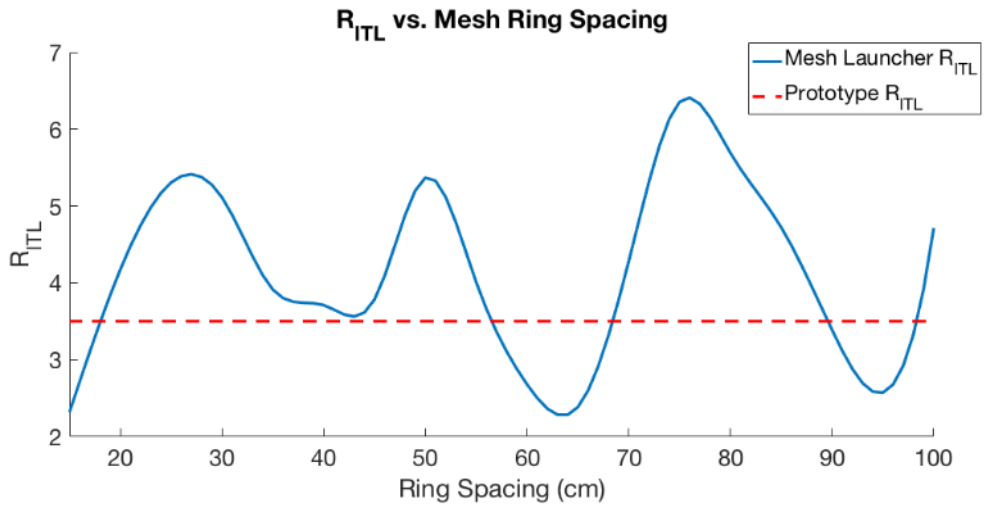

Fig. 5.14: Mesh launcher transmitter R_{ITL} as a function of ring spacing for 225 MHz excitation.

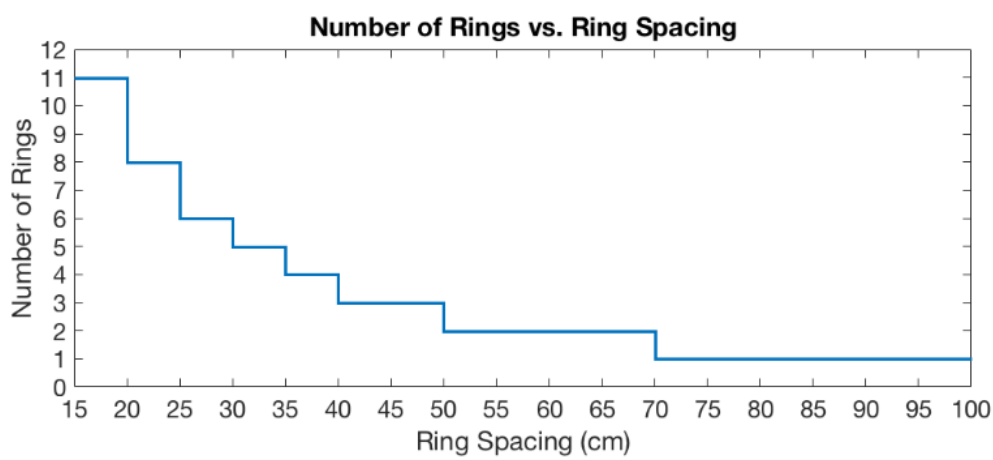

Fig. 5.15: Number of rings in mesh launcher as a function of ring spacing.

It is evident from Fig. 5.14 that R_{ITL} is a somewhat periodic function of ring spacing. This is because the apertures created by the space between conductive surfaces lead to interference patterns that either facilitate or cancel field leakage. Because of this, there are distinct regions where R_{ITL} is minimized. Two such regions are around when the ring spacing is 65 cm with two rings and when the ring spacing is 95 cm with only one ring. In both of these regions, the simulated R_{ITL} is lower than the measured value of the prototype above, showing feasibility. A more in-depth analysis is beyond the scope of this work, but this study shows that mesh launchers serve as a tenable solution for GLine launcher design.

5.7 SAR Simulation

Since many potential GLine applications involve humans standing within the transmitter area, the question of electromagnetic safety arises. To address this on a base level, simulations were conducted in HFSS at 225 MHz to determine the Specific Absorption Rate (SAR) characteristics of the system. A homogeneous human phantom made up of a head and body was constructed in HFSS using parameters derived from the contents of IEEE Std 1528-2013 [33]. The parameters are given in the table below.

Table 5.2
HFSS Human Phantom Dielectric Parameters

Phantom Section	ε_r	σ (S/m)
Head	48	0.83
Body	59.75	0.867

Note that the table in [33] does not list values at 225 MHz. The values above were extrapolated from the given data.

To characterize the SAR, the human phantom, pictured in Fig. 5.16, was placed at set distances from the center conductor of a GLine transmitter while the input power was swept between -30 and 10 dB (1 mW-10 W). The height of the phantom is 1.74 m, the radius of the head is 12 cm, and the radius of the body's trunk region is 18 cm. The distance from the center conductor is defined from the center axis of the phantom. The local SAR was measured for each

case and the peak values in both the head and body are plotted in Fig. 5.17 against the 1.6 W/kg limit mandated by the FCC. Note that the local SAR provides a more conservative metric for this study since it will always be larger than the SAR averaged over a region greater than a single mesh cell.

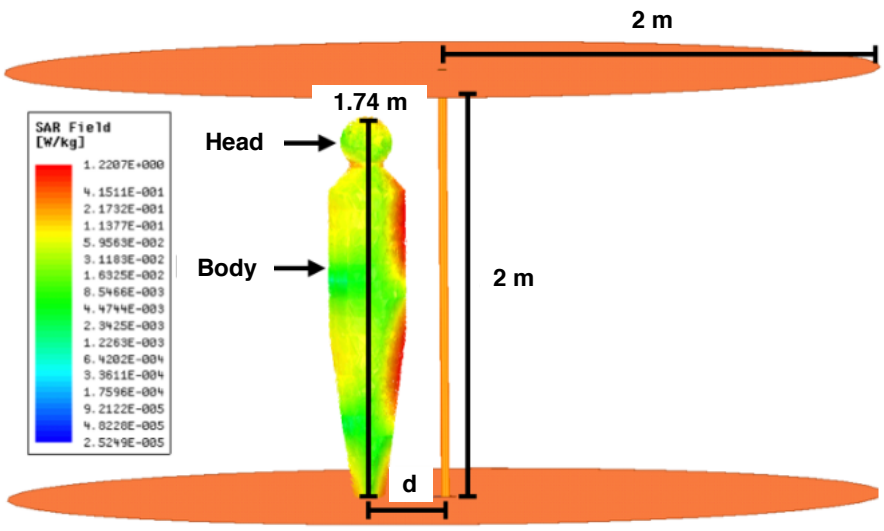

Fig. 5.16: Human phantom positioned inside GLine transmitter for SAR simulation.

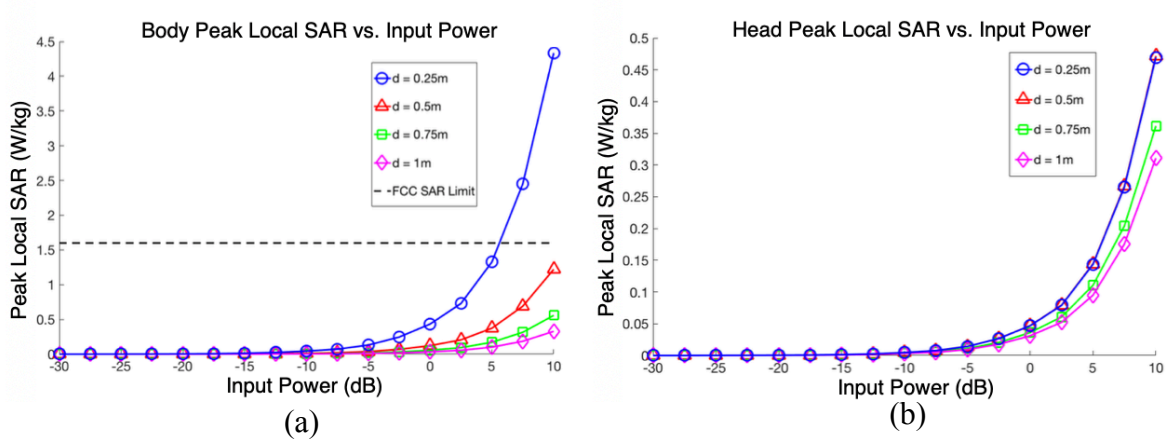

Fig. 5.17: (a) Simulated peak local SAR in phantom body as a function of input power and (b) simulated peak local SAR in phantom head as a function of input power.

5.8 Conclusions

In this chapter, the second GLine prototype was laid out and multiple performance experiments were realized. It was shown that the prototype was capable of achieving a 38% RF efficiency for one receiver and a 48% combined RF efficiency for two receivers when all receivers are positioned at .5 m away from the center conductor for a 233 MHz signal. It was also shown that the transmitter can deliver power to a rectifier load at a total efficiency of 25% for the same case as stated above, and that the transmitter has a high degree of cylindrical symmetry. Finally, it was shown that the GLine can support 5 receivers simultaneously and the combined RF efficiency for this case was 38%. This marks the current state-of-the-art for GLine WPT technology. In the next chapter, a method for miniaturizing receivers without the use of a matching network will be given in order to create topologies more appropriate for smaller electronics such as wearables and medical implants.

6. METAMATERIAL-BASED MINIATURIZED RECEIVERS

In this chapter, a design technique for creating miniaturized, intrinsically-matched receiver topologies that are more conducive to small electronics WPT such as wearable electronics, sensors, and general Internet of Things applications. Using wireless power transfer for small form-factor energy harvesting has indeed attracted interest from the research community as evidenced by [9], [34]-[36], and should be pursued to increase the ubiquitousness of such systems. The technique herein is primarily based on field coupling to metamaterial-inspired planar geometries that compensate for the highly reactive impedances of electrically-short structures to create an impedance-matched receiver. This type of technique was chosen due to the extensive past success other researchers have had in using metamaterials to create electrically short antennas [37]-[39]. It should be noted that other work that uses metamatrial and electrically-small antenna (ESA) concepts to enhance WPT systems has been conducted previously [35], [40]. However, this worked involved resonant coupling and more complex manufacturing processes than would be ideal for the purposes This method is detailed further below.

6.1 Metamaterial-Based Antenna Design

The structures designed for this work apply the techniques developed by Erentok et al. to design matched electrically-short antennas [37]. The so-called “EZ Antennas” of their work use metamaterial (MTM) loading to achieve miniaturization. While both 2D and 3D topologies are discussed in [37], for our purposes, only 2D planar implementations are of interest. Further only magnetic variants were considered for this work, as their performance is less sensitive to environmental factors.

Magnetic planar MTM topologies consist of three components; an electrically-short loop, a feed structure to excite the loop, and an MTM loading geometry, all printed on a substrate. The MTM loading is implemented by including a capacitive MTM unit cell topology that is closely coupled to the loop. This can be implemented with interdigital capacitor sections surrounding the electrically-short loop or even by lumped elements connected to an outer loop that surrounds the

electrically-short loop. It should be noted that the planar magnetic implementations given in [37] also include a ground plane. This is to improve the radiation characteristics of the antennas. However, for a coupled WPT application, this is unnecessary and disadvantageous, as it increases the overall antenna profile considerably. Fortunately, the ground plane may be omitted by invoking image theory and mirroring the geometry about the ground plane's would-be position. The figure below illustrates this concept, along with an example implementation that uses interdigital capacitive loading and a feed that taps the electrically-short loop directly.

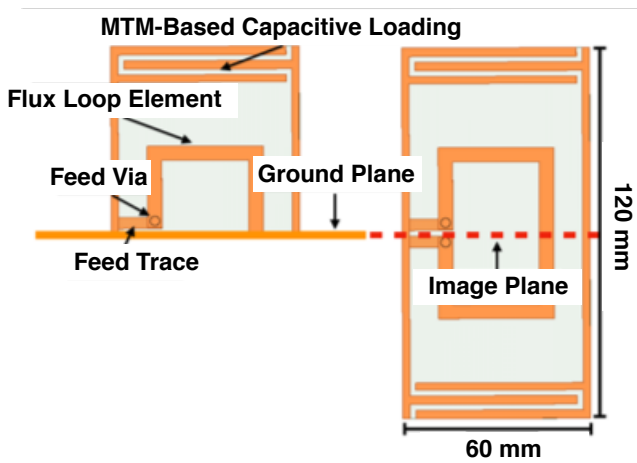

Fig. 6.1: Metamaterial-loaded loop image theory extrapolation.

In Fig. 6.1, the feed connects directly to the excitation loop. This is acceptable if a ground plane is used. However, the image theory version of the design constitutes an unbalanced-balanced interface if a coaxial connector is used for feeding. To remedy this, the designs herein will be fed through a transformer structure implemented by coupling the feed signal electromagnetically from the side of the substrate opposite that of the electrically-short loop. The transformer section exact geometry is flexible, but for the work here, these sections are implemented as two open-circuited traces (one connected to the feed probe and one to ground) that form a dipole-looking section. In the figure below, this type of feed is pictured next to a direct-tap feed.

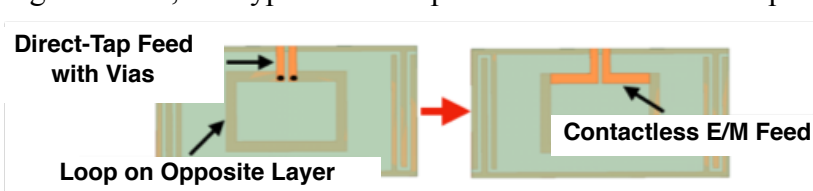

Fig. 6.2: (Left) Direct-tap loop feed and (right) electromagnetically-coupled feed.

It should be noted that the degree of miniaturization can be pushed further by maximizing the capacitive loading for a certain geometry. There are two ways to do this that go beyond the designs illustrated above. The first is to apply lumped elements to whatever MTM structure is in place, lowering the frequency at which the antenna is matched. Another way to do this without lumped elements is to generate capacitance between the upper and lower layers of the substrate. Figs. 6.1 and 6.2 show scenarios where the layer that houses the feed contains nothing else but the feed. However, is is possible to design the antenna such that the electrically-short loop and the feed share a substrate surface, while the MTM loading is relegated to the opposite layer. By doing this, one may widen the copper surface of the loop and create a high capacitance between the loop and MTM topology through the substrate, which augments capacitive loading and pushes the miniaturization further. In addition, this technique can be combined with lumped elements to facilitate more miniaturization.

It should be noted, however, that there is a trade-off between miniaturization and WPT efficiency. For the magnetic case, the coupling between the transmitter and receiver is limited by the available flux-linkage. For a given field strength, this linkage is determined by the physical size of the electrically-short loop. As such, the maximum efficiency of the link will be inversely-proportional to the loop area. This should be kept in mind during the design process. In the next section, the antennas developed and fabricated for this work will be presented.

6.2 Fabricated Miniaturized Antennas

For this work, three electrically-small receivers were constructed, all using the techniques described above. The designs were optimized for operation frequencies centered around 233 MHz, as with the implementations of the previous chapters. All loops were fabricated on FR4 substrates using standard PCB processes. They are illustrated below, along with a table detailing the design dimensions. Note the numbering of the loops in the figure, as they will be referred to as such in the following discussions. The matching and GLine WPT performance of each receiver was tested to evaluate the antennas. These results are given in the proceeding section.

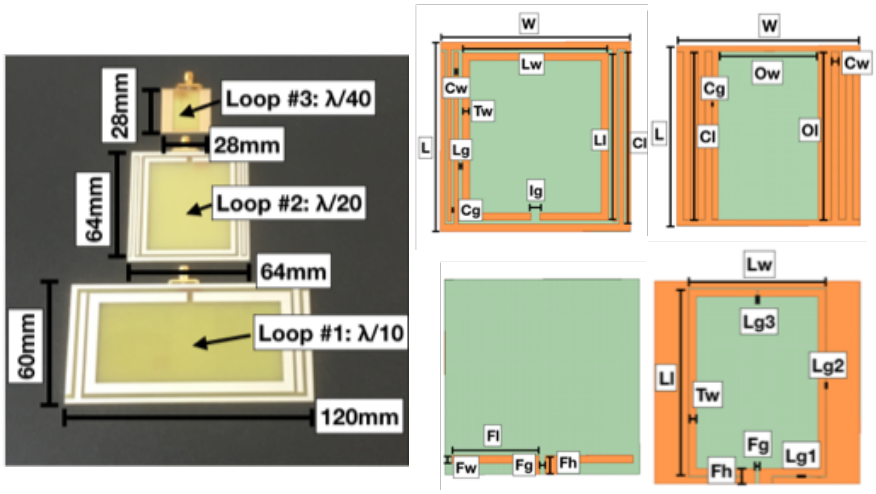

Fig. 6.3:(Left) Fabricated loops, (middle top) 1-layer top, (middle bottom) 1-layer bottom, (right top) 2-layer top, (right bottom) 2-layer bottom.

Table 6.1
MTM loop dimensions (mm)

Loop #	Loop Class	L	W	Ll	Lw	Cl	Cw	Tw	Lg	Cg	Ig	Fl	Fw	Fg	Fh	Ol	Ow	Lg1	Lg2	Lg3
1	1	60.45	120.9	51.15	102.3	53.8	3	5	1.44	1.86	3	9	5	2	9.65	-	-	-	-	-
2	1	64.4	64.4	57	49.5	58.6	1.49	2.48	1.39	0.79	3	29	2.48	2	6.2	-	-	-	-	-
3	2	27.72	28.16	25.56	18.73	25.86	1	1	-	0.1016	-	-	-	0.5	2.078	25.96	15.36	0.198	0.0833	0.15

To begin, the S_{11} performance of each antenna was measured with a VNA to ensure proper matching. A special note should be given to Loop #3, as it was designed to be optimally matched at a frequency considerably higher than 233 MHz so that the efficacy of applying lumped elements to alter the matching could be demonstrated. Further, a reference loop with an area between those of Loop #1 and Loop #2 was implemented with its own impedance-matching network for comparison. In Fig. 4.4, the return loss performance of all the loops is given, as well as an image of the lumped element augmentation of loop #3.

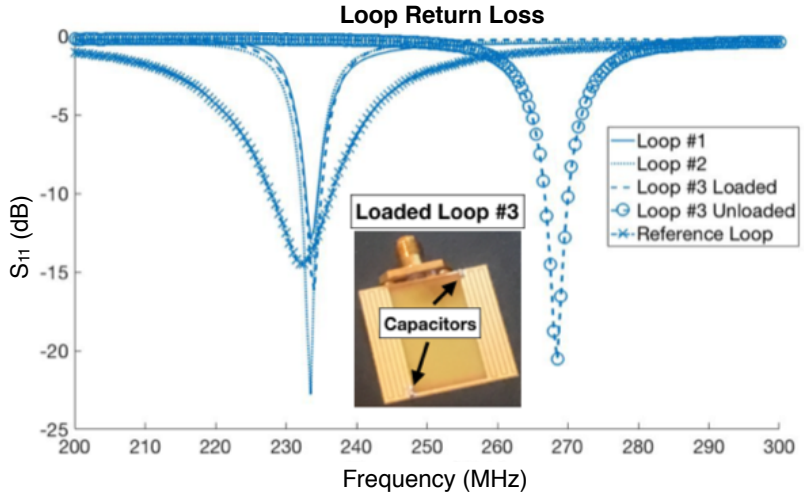

Fig. 6.4: Fabricated loop S_{11} and loaded loop #3 chip capacitor placement.

Next, GLine WPT tests were conducted very similarly to those of the previous chapter. As before, each loop was placed roughly halfway up the line (higher than with the electric coupling case due to the standing wave distribution) and moved a set distance away from the center conductor, recording the RF efficiency (S_{21}) at each position for a 233 MHz input signal. Note that the transmitter required an input impedance matching network designed using the techniques described in the previous chapter. Additionally, the RF efficiency of Loop #1 was evaluated while mounted to an armband to simulate a wearable electronics application. Note that the arm-mounting disrupted the matching of Loop #1, so it required its own impedance-matching network in this configuration. If this was the primary application of the antenna, a design could be created to compensate for this matching condition without an external network, but such a design is not presented here. For the arm-mounted test, the loop was evaluated in both horizontal and vertical orientations to cover both potential cases. Below, in Figs. 6.5-6.7, the experimental setup and the RF efficiency results of all antennas are given, along with the matching of Loop #1 when it is mounted on an armband connected through an external matching network.

From Fig. 6.4, it can be seen that the matching is excellent in all cases. For Loop #3, it is also seen that good matching was preserved even when the frequency was shifted, demonstrating potential tunability of the designs. The data in Fig. 6.6 shows that the RF efficiencies of Loops #1 and #2 vary from 20%-5% and 16%-3% respectively in the distance range between .125m and .5m from the center conductor.

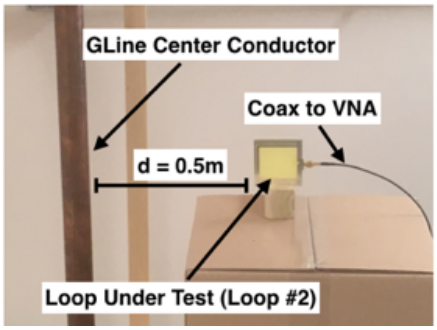

Fig. 6.5: MTM loop efficiency measurement setup inside GLine transmitter.

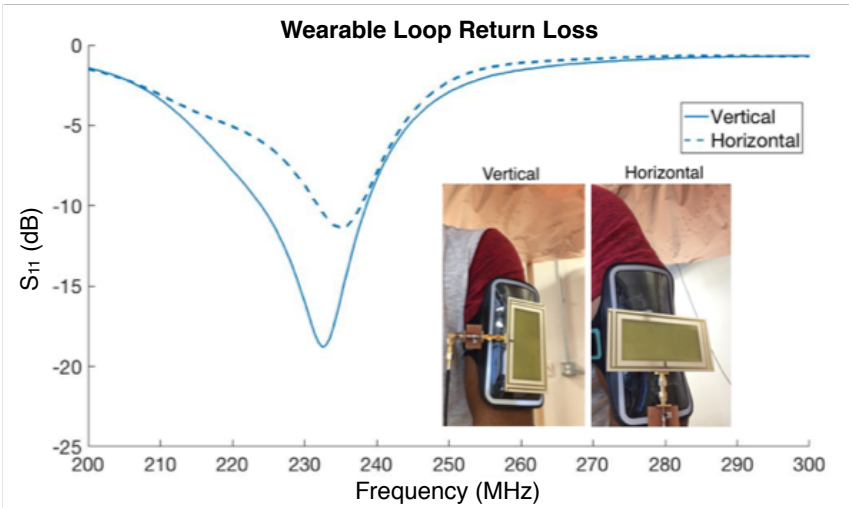

Fig. 6.6: Wearable loop return loss.

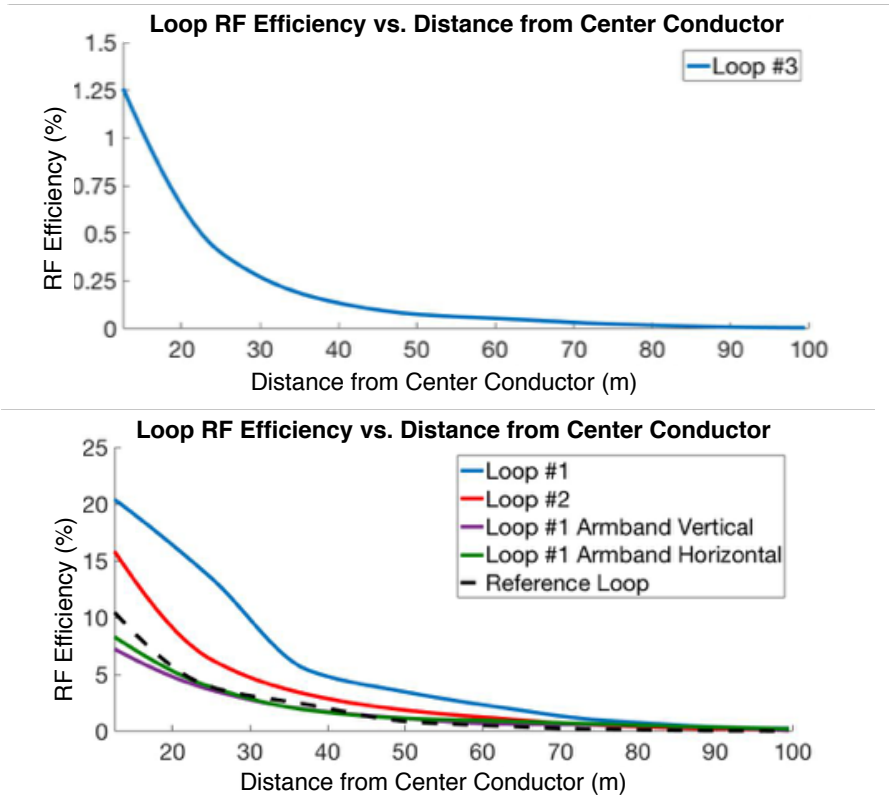

Fig. 6.7: Fabricated loop RF efficiency as a function of distance from GLine center conductor.

Each loop is seen to outpace the performance of the reference loop even though it is larger than Loop #2. This is attributed to impedance-matching network loss not present in the MTM topologies and lower degrees of scattering. When worn, the RF efficiency of Loop #1 decreases due to the field disruption caused by the human body and impedance-matching network loss. Despite this, the RF efficiency is still high enough to handle small mW power electronics. The efficiency of Loop #3 is notably small due to its limited flux linkage, with an RF efficiency of < 2%. For the reason, this design should be reserved for very small powering applications such as medical implants.

6.4 Conclusions

In this chapter, a technique for designing intrinsically-matched MTM-based loop receivers geared toward small electronics WPT was presented. Designs utilizing this method were realized and results of the fabricated topologies were given. In the next chapter, future open-line WPT will be discussed regarding an alternate transmission line choice, the twin lead line.

7. TWIN-LEAD LINE WIRELESS POWER TRANSFER

In this chapter, the conceptualization, design, and proof-of-principle experimentation of a twin-lead transmission line WPT system will be discussed. This discussion will begin with an analytical and computational analysis of the twin-lead line geometry. Following this, the design workflow for choosing twin-lead line parameters will be laid out, followed by a presentation of experimental results. Note that one aspect of the twin-lead line system presented herein that was not explored for the GLine geometry is the idea of incorporating a tunable termination. Given the applications that the twin-lead line is appropriate for, a variable termination is quite valuable. These applications as well as the effects of a tunable termination will be discussed further below.

7.1 Twin-Lead Power Rail Applications

As shown previously, the GLine's field distribution fall-off rate with distance makes it appropriate for mid-range applications. While the twin-lead fields do indeed extend to infinity, they do not share this inherent fall-off characteristic (this will be explained further in the following twin-lead theory section). This is a disadvantageous from a range perspective. However, the twin-lead line does provide a distinct benefit over the GLine in that it does not require large launchers to excite its mode, which is a quasi-TEM mode rather than a TM mode. This does mean that the twin-lead wires carry current and the ohmic loss associated with that, but it also means the use cases for a twin-lead system have more versatility. In particular, a WPT application that does not require very much range but would still benefit from a transmission line WPT scheme is that of a power rail, particularly regarding electric automobiles and UAVs. Using WPT to charge electric cars is not a new concept and it has received a good deal of attention in the research community. However, the techniques that have been investigated typically center around resonant or inductive wireless power transfer [5], [36], [41]-[53]. In these cases, the systems presented thus far must rely on either a static receiver ([41]-[44], [47]), have a transmitter topology that is untenable for vehicles or that must include many separate Tx coupling elements ([5], [48]-[52]), have a tiny transfer efficiency ([36]), or even have a whole separate vehicle for WPT

([45]). [53] does not have these drawbacks, but its topology is not appropriate for wide-area charging applications. These aspects restrict vehicle mobility and increase the cost and complexity of such systems dramatically. While this is possible, it is clear that a unified power rail that can cover a much wider area with one transmitter would be preferable. The twin-lead line is a viable candidate for such a system given its geometry. In the case of UAVs, the twin-lead line is even more appropriate given that the WPT transmitter would be elevated if the UAV was to charge during travel, an aspect of the system that would cause problems if an array of resonant coil transmitters were used. In the figure below, concepts of the power rail applications described above are depicted.

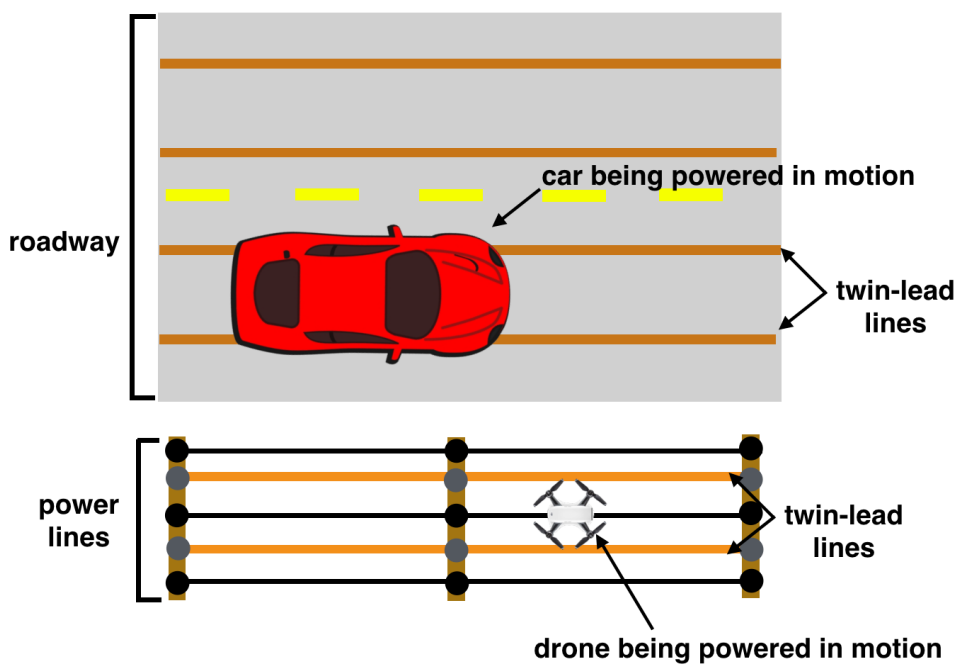

Fig. 7.1: Concept of a car and drone being powered wirelessly by twin-lead transmission lines.

In the next section, the analytical electromagnetic theory of the twin lead line will be discussed.

7.2 Twin-Lead Transmission Line Analytical Solution

The twin-lead transmission line is treated as a quasi-TEM structure with each wire carrying equal and opposite current. The radiation from one wire, if the wire spacing is small enough, is cancelled out by the radiation of the other wire, so for most conventional twin-lead applications, radiation need not be considered. As such, each wire may be modeled as an infinitesimally thin, infinitely-long line of charge. These equivalent lines are positioned such that the surfaces of the finite wires are equipotentials. Once the correct positioning is found, the superposition of the potentials due to these lines is evaluated and the resultant E and H-fields are found. These fields are expressed as follows in cylindrical and cartesian coordinates:

$$E_\rho = -\frac{Q'}{2\pi\varepsilon}\left[\frac{\rho - ag\cos\varphi}{\rho^2 - 2ag\rho\cos\varphi + a^2g^2} - \frac{\rho g^2 - ag\cos\varphi}{\rho^2 g^2 - 2ag\rho\cos\varphi + a^2}\right] \tag{7.1a}$$

$$E_\varphi = -\frac{Q'}{2\pi\varepsilon}\left[\frac{\rho - ag\cos\varphi}{\rho^2 - 2ag\rho\cos\varphi + a^2g^2} - \frac{\rho g^2 - ag\cos\varphi}{\rho^2 g^2 - 2ag\rho\cos\varphi + a^2}\right] \tag{7.1b}$$

$$H_\rho = -\frac{E_\varphi}{\eta} \tag{7.1c}$$

$$H_\varphi = \frac{E_\rho}{\eta} \tag{7.1d}$$

$$E_x = E_\rho\cos\varphi - E_\varphi\sin\varphi \tag{7.1e}$$

$$E_y = E_\rho\sin\varphi + E_\varphi\cos\varphi \tag{7.1f}$$

$$H_x = H_\rho\cos\varphi - H_\varphi\sin\varphi \tag{7.1g}$$

$$H_y = H_\rho\sin\varphi + H_\varphi\cos\varphi \tag{7.1h}$$

A detailed derivation may be found in [20]. In Fig. 7.2 below, the E and H-field distributions are visualized in HFSS

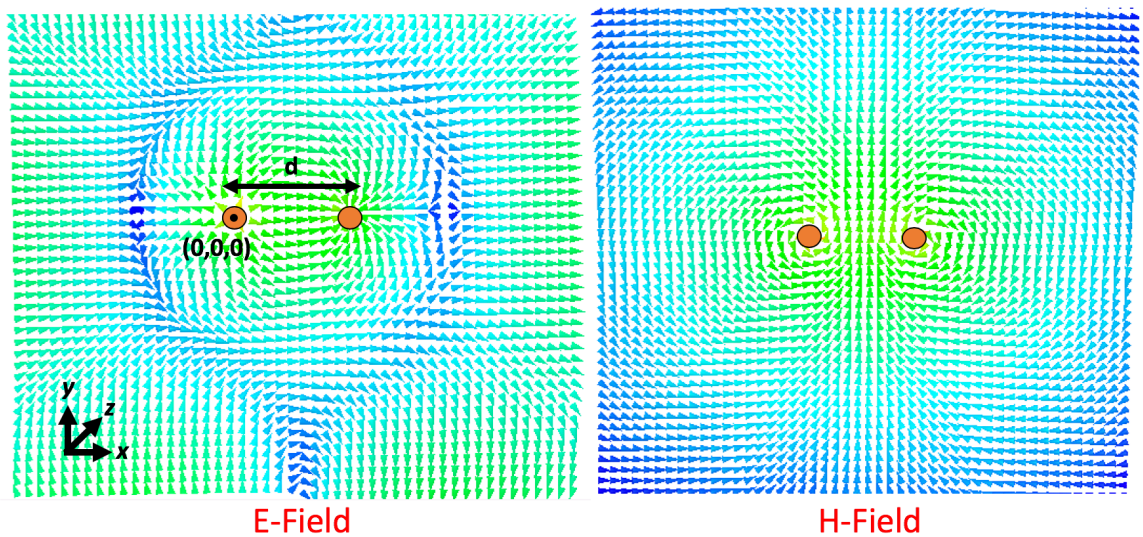

Fig. 7.2: E and H-field visualization for a twin-lead line with wire separation *d*.

This formulation holds for small wire separation distances, but since it assumes a quasi-static approximation (no radiation), some aspects of the formulation (e.g. radiaiton line loss) will break down if the wires are separated by a large enough distance. As such, a Hertzian Aggregation script was written in MATLAB to determine the field characteristics for an infinitely long line with arbitrary separation distance. The next section details the technique of this script.

7.3 Twin-Lead Line Hertzian Aggregation

It is known that the fields due to any current distribution may be evaluated as a superposition of Hertzian dipoles, which are infinitesimal current elements whose fields may be solved directly in a straightforward manner. By replacing the the twin-lead line by two lines of Hertzian dipoles and summing their fields, we may compute the twin-lead line field distribution. An illustration of this process is shown below:

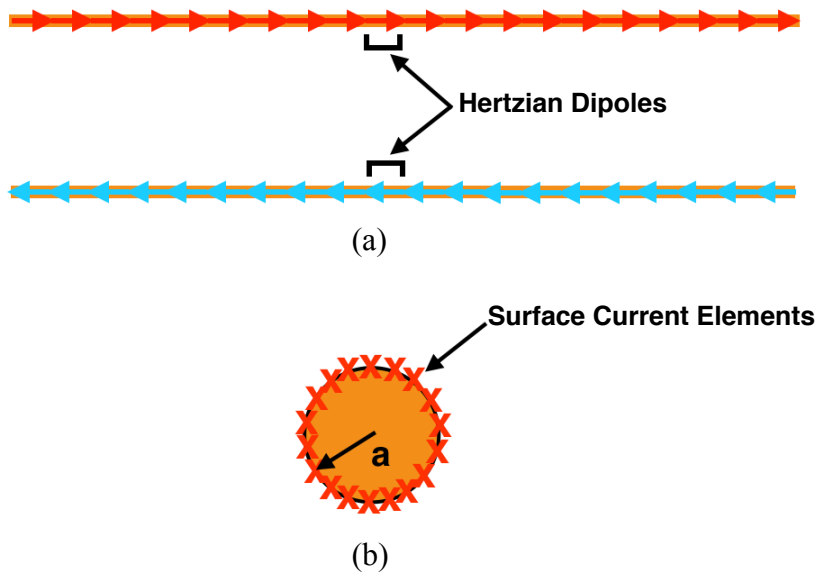

Fig. 7.3: (a) Twin-Lead line Hertzian dipole division viewed from the side and (b) visualization of dipoles on the surface of a wire with finite radius a.

Note that the current on wires of finite radius are assumed to be sheet currents here and are thus represented as a sheet of Hertzian dipoles outlining the wire surface as depicted in Fig. 7.3b. Given a z-directed Hertzian dipole current element, the fields of each individual dipole may be expressed as follows:

$$E_r = jk\eta_o I_o dl \frac{e^{-jkr}}{4\pi r}\left[\frac{1}{jkr} + \left(\frac{1}{jkr}\right)^2\right] 2\cos\theta \tag{7.2a}$$

$$E_\theta = jk\eta_o I_o dl \frac{e^{-jkr}}{4\pi r}\left[1 + \frac{1}{jkr} + \left(\frac{1}{jkr}\right)^2\right] \sin\theta \tag{7.2b}$$

$$H_\varphi = jkI_o dl \frac{e^{-jkr}}{4\pi r}\left[1 + \frac{1}{jkr}\right] \sin\theta \tag{7.2c}$$

where r is the magnitude of the vector extending from the dipole's location to the point of observation. Before solving for the fields, an appropriate current distribution must be chosen. It is assumed that, since the currents are sustained on straight wires with no terminations, that the currents will be sinusoidal regardless separation distance. This assumption is consistent with the sinusoidal nature of straight wire antennas [54]-[55]. Another factor we must account for is signal

degradation with propagation, primarily from radiation loss. Since we are modeling an arbitrary geometry, we will not assume that this loss is negligible, meaning that the current sinusoid will be damped. However, this presents a difficult computational problem, as the degradation must be known in order to model the correct current distribution. To get around this, the current will be expressed using the following equation:

$$I(z) = I_0 e^{\gamma z} \tag{7.3}$$

where γ is a propagation constant described as

$$\gamma = \sqrt{(j\omega L + R_o + R_{rad})(j\omega C)} \tag{7.4a}$$

$$L = \frac{\mu}{\pi} a\cosh\frac{d}{2a} \tag{7.4b}$$

$$C = \frac{\pi}{\varepsilon} a\cosh\frac{d}{2a} \tag{7.4c}$$

$$R_o = \frac{\sqrt{\frac{\pi f \mu}{\sigma}}}{\pi a} \frac{d}{\sqrt{d^2 - 4a^2}} \tag{7.4d}$$

where d is the wire separation distance, a is the wire radius, C and L are the capacitance and inductance per unit length (the computation of which are not limited by the quasi-static approximation), and R_{rad} is the equivalent radiation resistance per unit length. Note here that the conductance per unit meter G is neglected since the dielectric is air for this work. Using Poynting's Theorem, we may define R_{rad} as follows:

$$R_{rad} = \frac{1}{I_o^2} \int_0^{2\pi} \mathrm{Re}(E_{tot} \times H_{tot}^*) \rho_o d\varphi \tag{7.5}$$

where ρ_o is the radial of the power flow surface distance from the origin. To elaborate, the radiation resistance per unit meter is taken by evaluating a line integral about the contour of a cylinder containing the twin-lead line, one of sufficient radius such that the Hertzian near-fields are negligible. However, again, the field in the expression cannot be known without first knowing R_{rad}. To

get around this, an iterative algorithm was written. The algorithm, for a certain wire separation, guessed a value for R_{rad}, and then carried out the Hertzian aggregation. It then used the resultant fields to compute a new R_{rad} value. If the computed R_{rad} did not match the guess, the guess was modified up or down based on whether the guess was lower or higher than the computed value respectively. This process was repeated until the difference between the guess and the computed value was below an established margin of error (< .1 Ω), then the fields were computed one final time to evaluate the correct fields. This process was coded in MATLAB and the code is given in Appendix I.

Once a computational model was established, the computed fields were compared to the analytical fields for different wire separations for a 225 MHz signal (the frequency used for the experiments of previous chapters). In the figure below, for x = d/2 (see Fig. 7.2 above for coordinate system), the Ex field fall-off is plotted for both the analytical and computational cases regarding several wire separations. Note that the fields are normalized about the point where y = 0.1.

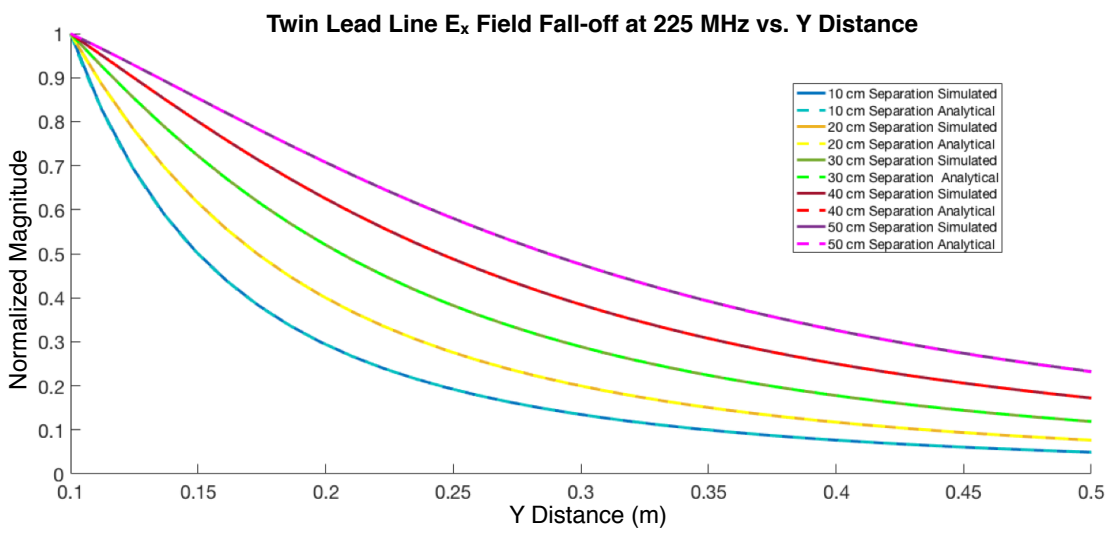

Fig. 7.4: Twin-lead Ex field fall-off calculated analytically compared to the Ex field fall-off simulated through Hertzian Aggregation.

The plot above indicates excellent agreement between the theory and the computational method. It also indicates that the theory holds for much larger separation distances than what is typically used for twin-lead transmission line applications. Additionally, since the computational method

has been verified, we may use it to characterize the propagation loss due to radiation. In the figures below, the radiation resistance per unit meter and the radiation attenuation in dB per 100m is given for the twin-lead line as a function of wire separation.

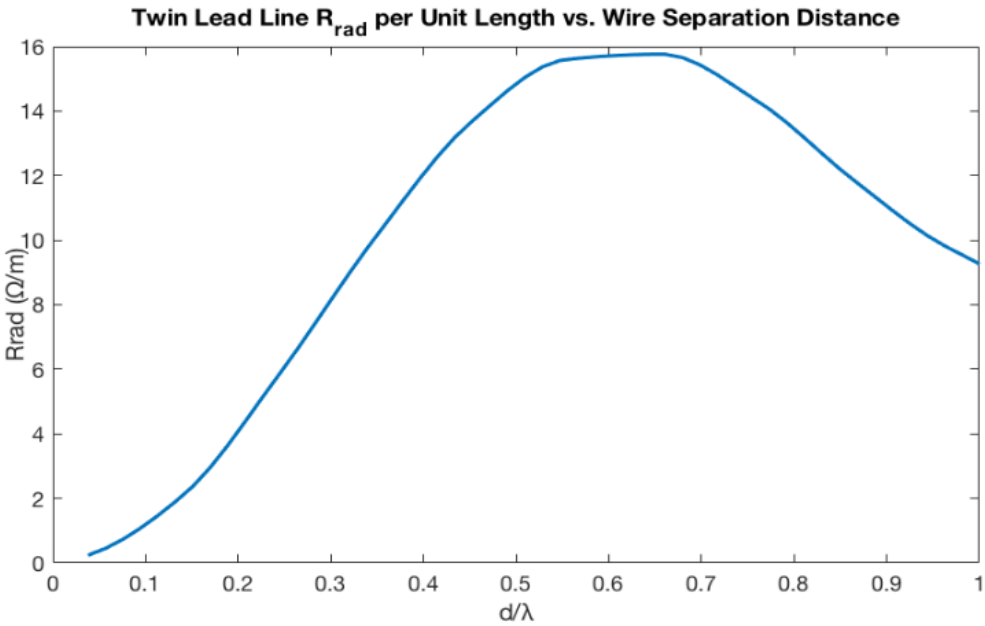

(a)

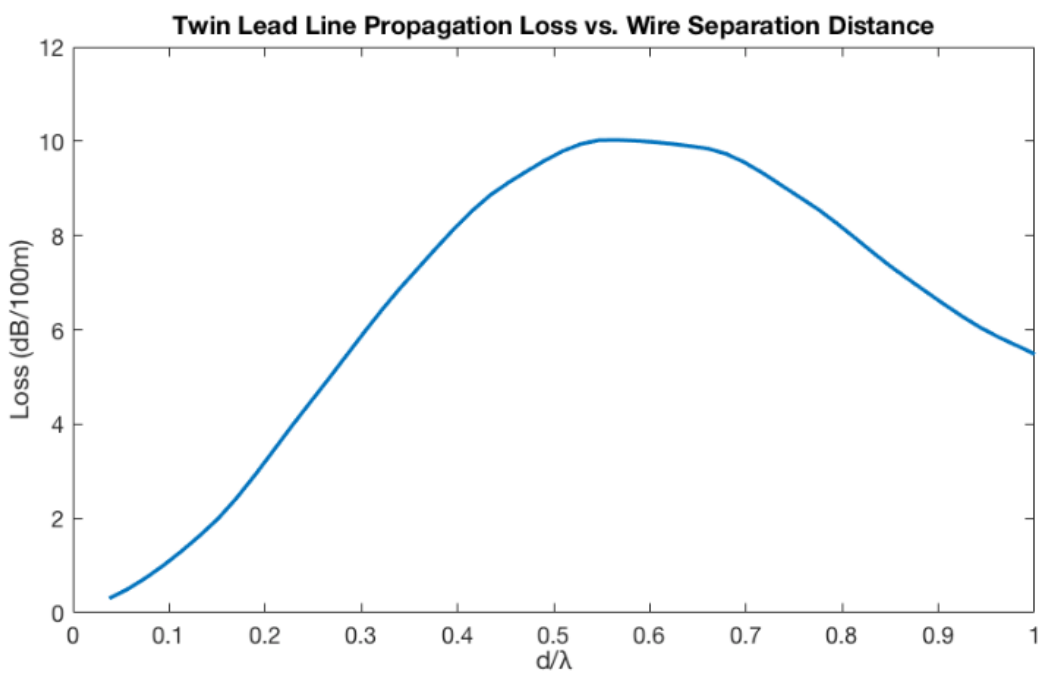

(b)

Fig. 7.5: (a) Twin-lead R_{rad} as a function of wire separation and (b) twin-lead loss as a function of wire separation.

As is shown above, the radiation loss is quite manageable for the wire separations investigated. These separations are also useful for WPT applications. Referring back to Fig. 7.4, it can be seen that the field fall-off rate is inversely proportional to the wire separation. It would seem then that larger separations are superior from a range perspective. However, this is not the whole story, as the geometries modeled thus far have had no terminations or excitations. In the next section, practical implementations of wide-separation twin-lead lines will be investigated.

7.4 Finite Length Wide Separation Twin-Lead Line Excitation

The cases shown in Fig. 7.4 in the last section were for wire separations on the order of tens of centimeters, much larger than most transmission lines. As such, the feeding and termination schemes must be conducive to these separation distances. To accomplish efficient twin-lead excitation and termination, linear tapers will be applied to the ends of the twin lead line. In the figure below, such an implementation is shown:

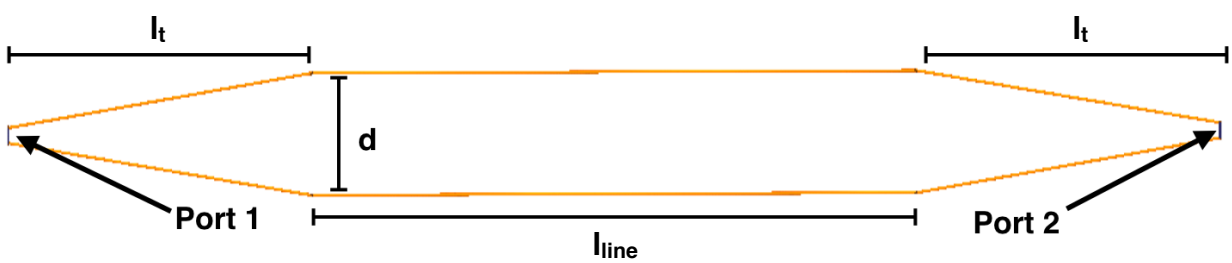

Fig. 7.6: Linear taper-fed twin-lead line.

Note that the length of the taper is dependent on the frequency of operation. For this study, we will stick to 225 MHz. As alluded to above, twin-lead lines with wider separations have slower field fall-off rates. However, notice that, for the same overall length, larger wire separations require larger taper flare angles. This, in turn, will lead to radiation loss at the taper sites. The reason is that the radiation from one taper arm is cancelled less and less by the radiation from the other arm if the flare angle is increased. To demonstrate this, an HFSS simulation study was conducted at frequencies around 225 MHz to characterize the radiation loss related to the taper flare. In the study, a 1m twin-lead line was simulated with two half-meter long tapers attached to the

ends. The line was terminated with a 50 Ω load. The insertion loss and return loss were then measured while sweeping the wire separation. For each wire separation, the input impedance was matched to the value that minimized the insertion loss at the optimal frequency (not necessarily 225 MHz since the increased wire flare increased the effective length of the line). In the figures below, the S-parameter data for the study is shown, as well as the radiation loss as a function of the wire separation.

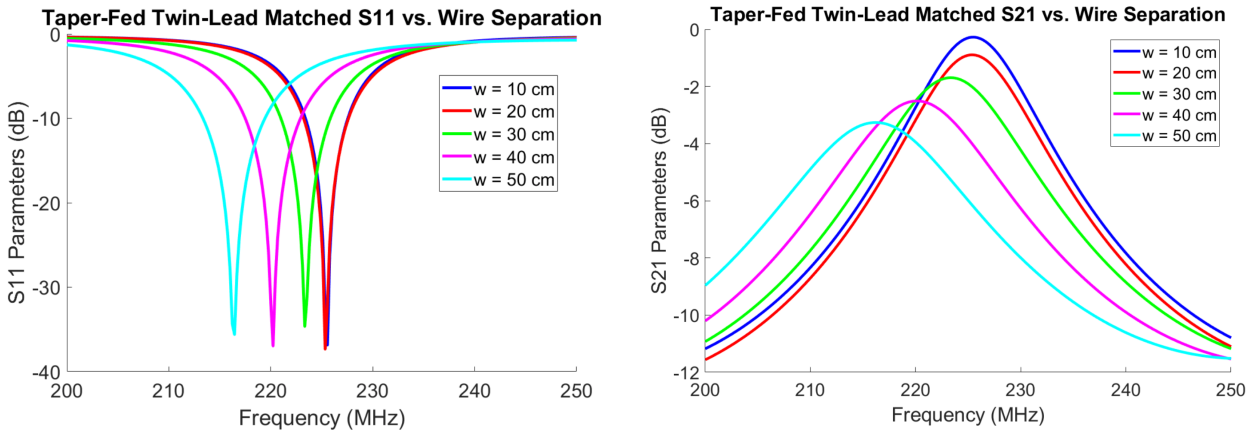

(a) (b)

Fig. 7.7: Taper-Fed twin-lead S-parameters for different wire separations.

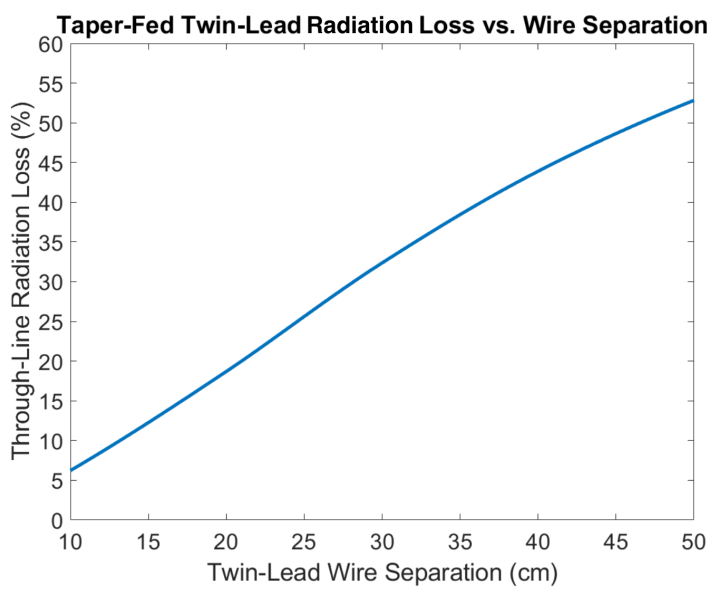

Fig. 7.8: Taper-Fed twin-lead through-line radiation loss as a percentage of input power for different wire separations.

As the plots indicate, the radiation loss is directly proportional to the flare angle of the feed and termination tapers, meaning that, for a practical implementation, the separation is more of a limiting factor than is indicated by Fig. 7.4. This information will be used in the proceeding sections when determining WPT system parameters. In the next section, the effects of a variable line termination will be explored.

7.5 Tunable Termination

The transmission line WPT systems discussed in previous chapters rely on the generation of a standing-wave distribution on the line. The twin-lead line is no different in this respect. However, as alluded to above, the twin-lead termination will not be limited to a static short. Instead, a variable reactive termination will be attached to the end of the twin-lead line. This will force a boundary condition at the end of the line that will tune the overall field distribution, ie, the locations of the field peaks and nulls. Referring to the tapered excitation section implementation of the previous section, we may use HFSS to visualize the effect of differing terminations on the field distribution. In the figure below, the electric field standing wave distributions on a tapered excitation twin lead line that result from terminations ranging between -500j Ω and 500j Ω are shown. This is for a 225 MHz signal on a 1m long line with .5m long end tapers. Note the wire separation is 20 cm here.

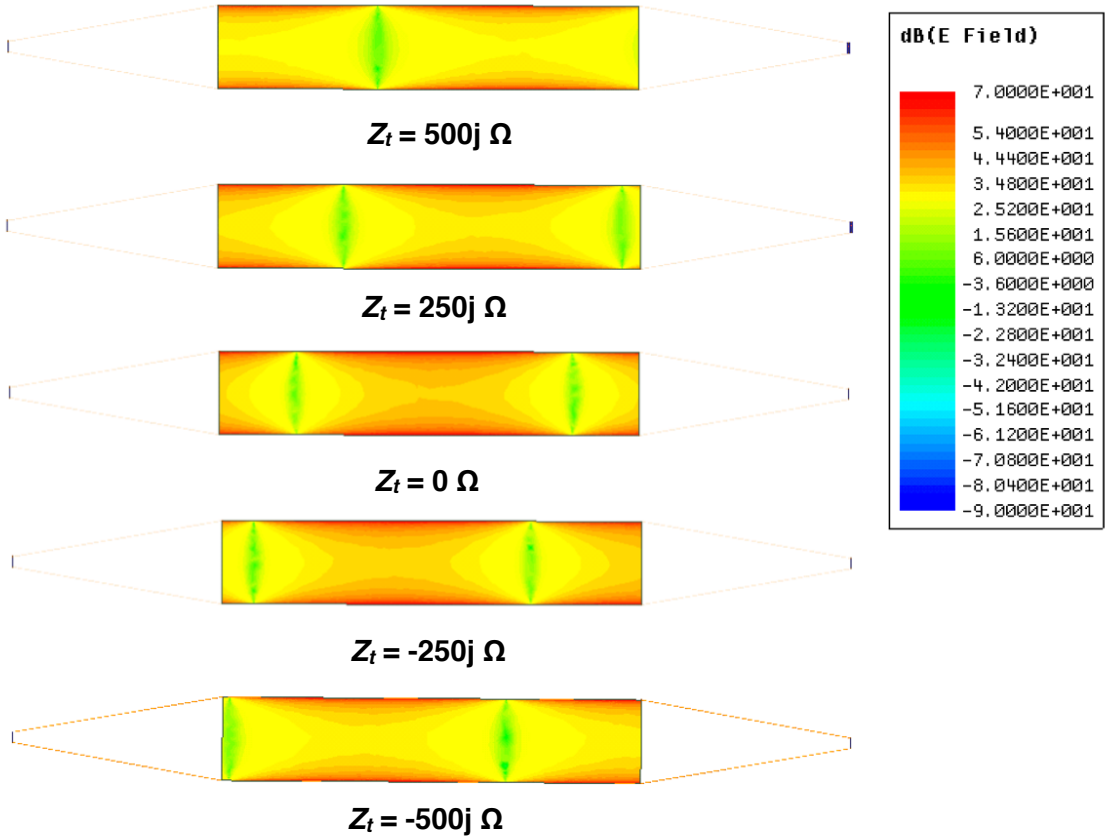

Fig. 7.9: Twin-Lead standing wave distributions for differing terminations with a 1 W excitation.

As the plots above indicate, the electric field peaks shift in position in relation to the termination impedance, as expected. We may use this property to tune the distribution according to a receiver position in a WPT system, as will be demonstrated below. In the next section, the design considerations of a twin-lead line WPT system will be presented.

7.6 Twin-Lead Line WPT System Design

The twin-lead line system presented here will be quite similar to the systems shown in previous chapters, but with a few important variations. Firstly, as mentioned before, the termination of the transmission line will be variable, providing flexibility in the receiver position along the line. Additionally, because of this, the input impedance matching network for the transmitter side must be variable as well since the impedance profile of the system is dependent on the standing wave distribution and receiver coupling. This also calls into question the receiver impedance

matching network. In fact, for the twin-lead system, this impedance matching network is not necessarily needed and will be omitted from the design. The reason lies in the coupling strength of the system. Since the twin-lead system range (in terms of distance from the line) is not the emphasis of this design as much as the power rail aspect is, the receiver position will be much closer to the line for most use cases in contrast to the GLine system. As such, the loading of the receiver on the transmitter impedance is more pronounced for this system and receiver-side scattering is less significant, so all of the impedance-matching may be relegated to the input network. With these changes in mind, Fig. 7.10 below illustrates a modified block diagram for the system.

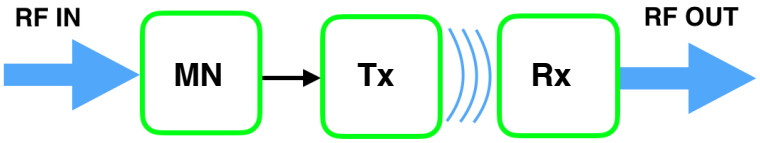

Fig. 7.10: Twin-Lead WPT system modified block diagram.

Next, the design procedure will be presented. Note that in this procedure, the transmission line coupling theory shown in Chapter 3 will not be used. This is to demonstrate a more heuristic design approach that is more efficient for this system given its complexity. Nevertheless, the theory still applies for all who want to use it for this line topology. In the next sub-section, design constraints for this work will be listed and discussed.

7.6.1 Design Constraints

By opening up the transmission line WPT system to include variable wave distributions and tunable impedance-matching, the potential complexity of the system has been increase dramatically. As such, some design constraints for the system presented in this work will be established for the sake of simplicity for the proof-of-principle experiments. These constraints are given as follows:

i.) All tunable elements in the system will be capacitive; any inductive elements used will be static for all cases.

ii.) The line's lateral coupling area will be divided into 3 "zones", which will be the po -sitions of focus during experimentation.

iii.) The impedance-matching network will be a standard LC circuit.

iv.) The impedance-matching network will be optimized for the case where the termina -tion is a short and the receiver is positioned halfway between the source and termi -nation, after which the network's capacitive element will be modified to accommo -date other positions and terminations.

The first constraint is applied due to the current dearth of efficient, inexpensive, commercially-available tunable inductive lumped elements in the VHF range. Tunable capacitors, on the other hand, are readily available and highly developed. Any inductive elements used in this work will be high-Q static air-core inductors. It is possible to implement switching circuits for adaptive matching such that inductors would not need to be tuned directly, but this is beyond the scope of the work presented here.

The second constraint places the experiment into a regime that is appropriate for a proof-of-principle scenario. In theory, it is possible to investigate the field distribution for every single possible use case along the line. This is, however, unnecessarily complicated for our purposes, which are more foundational than exhaustive. Therefore, in order to provide more focus to the current work, the line's lateral area will subdivided into five zones, each of a certain size, and these zones will be used to drive the design so as to not overcomplicate the initial investigation. Below, the subdivision scheme that will be used is illustrated:

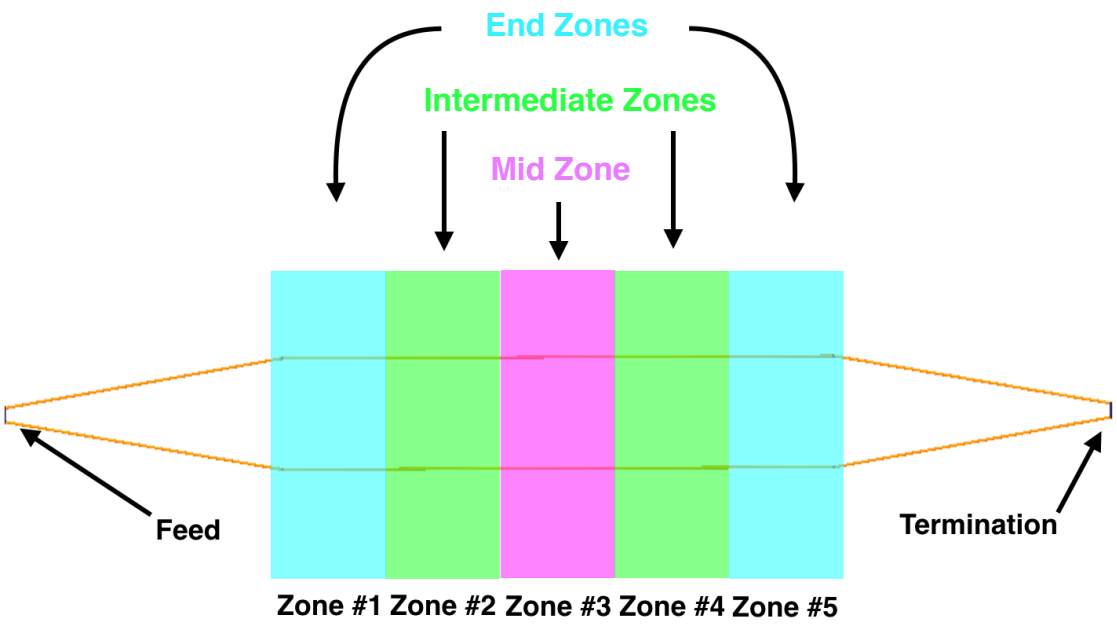

Fig. 7.11: Twin-Lead Zone subdivisions.

As the figure above shows, there will be one mid zone, two intermediate zones, and two end zones. The system will be designed such that there is a mode of operation for each zone class. More specifically, there will be one mode for the mid zone, one for both intermediate zones together, and one for both end zones together.

The third constraint is again applied in the name of initial simplicity. More complex impedance-matching schemes can be realized, and this can be the topic of future work, but the impedance-matching networks here will be standard LC networks.

The final constraint is made with the knowledge of the impedance-matching network limitations. Again, changing the standing wave on the line and the receiver position will shift the input impedance of the twin-lead line. As such, a circuit topology that works best for one operation mode may not be optimal for another. Because of the, the mid-position, short termination operation mode, which is a mode analogous to the GLine system distributions shown in previous chapters, will be treated as the base case that the system impedance-matching network will be optimized for. Then, without changing any topologies or inductors, the capacitive elements of the twin-lead circuits will be modified to accommodate other modes of operations. This is an appropriate procedure for a proof-of-principle case and can be readily expanded upon in future work.

Now that the design constraints have been explained, we may discuss the other aspects of the twin-lead design process. In the following section, the transmitter design process will be laid out.

7.6.2 Twin-Lead Transmitter

From the analysis in Sections 7.3 and 7.4, it is clear that there is a tradeoff between the range and the radiation loss as a function of wire separation. While the range is not a factor that can be neglected, since the applications being targeted with this technology do not require long range, radiation loss will be given more weight than field fall-off. As such, for the experiments herein, a twin lead line with a wire separation of 20 cm will be used. For a through-line case, as indicated in Fig. 7.7, the tapers account for approximately 1 dB of insertion loss between them for this separation. Further, the detuning from 225 MHz for this geometry is minimal. In the next section, the receiver geometry will be presented.

7.6.3 Twin-Lead Receiver

Since the base operation case involves a standing wave distribution that has an E-field peak at the center of the line, the receiver must be an electric structure. As it happens, the dipole receiver used for the improved GLine system prototype detailed in Chapter 5 is an appropriate receiver geometry for this case. Therefore, the same receiver that was used there will be used for the twin-lead system to couple off of its electric fields. Please refer to Chapter 5 for details of its design. It the next section, the termination circuit will be considered.

7.6.4 Termination Circuit

Clearly the termination circuit must be able to present a wide range of impedances in order to tune the standing wave effectively. Since any tunable elements for this work must be capacitive, this indicates the need for a variable capacitor with a wide range of tunability. However, a capacitor alone may have a difficult time covering the necessary impedances since it must vary between very low and very high values to maximize distribution diversity. To remedy this, we

will use a shunt resonator with a tunable capacitance instead of a capacitor alone. To understand why, consider the equations below that describe the rate of change of a single capacitor impedance and a shunt resonator impedance with respect to capacitance:

$$Z_{cap} = \frac{1}{j\omega C} \Rightarrow \frac{dZ_{cap}}{dC} = -\frac{1}{j\omega C^2} \tag{7.6a}$$

$$Z_{res} = \frac{1}{j\omega C + \frac{1}{j\omega L}} \Rightarrow \frac{dZ_{res}}{dC} = -\frac{j\omega}{(j\omega C + \frac{1}{j\omega L})^2} \tag{7.6b}$$

As can be seen, the inductor value for the shunt resonator can be used to influence the impedance variation such that a wider range of impedances can be obtained for a given capacitance range, meaning that a resonator termination should be used. For this work, such a resonator termination was implemented using a Knowles Voltronics AP55HV trimmer capacitor in parallel with two 65 nH CoilCraft air-core inductors. Both the circuit and the impedances it presents when the capacitor is swept are given in the figures below:

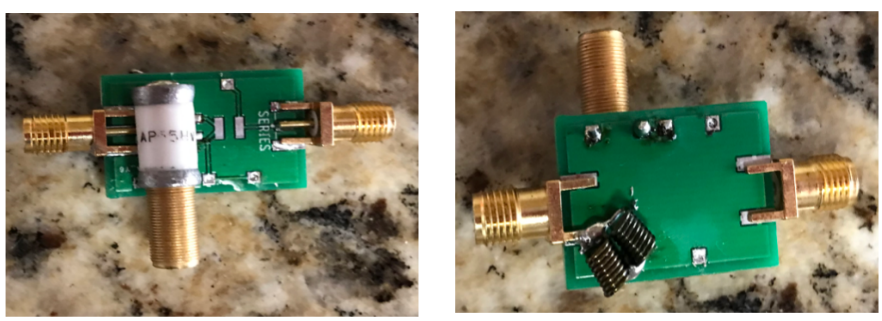

(a) (b)

Fig. 7.12: (a) Termination circuit topside view showing trimmer capacitor and (b) bottomside view showing parallel inductors.

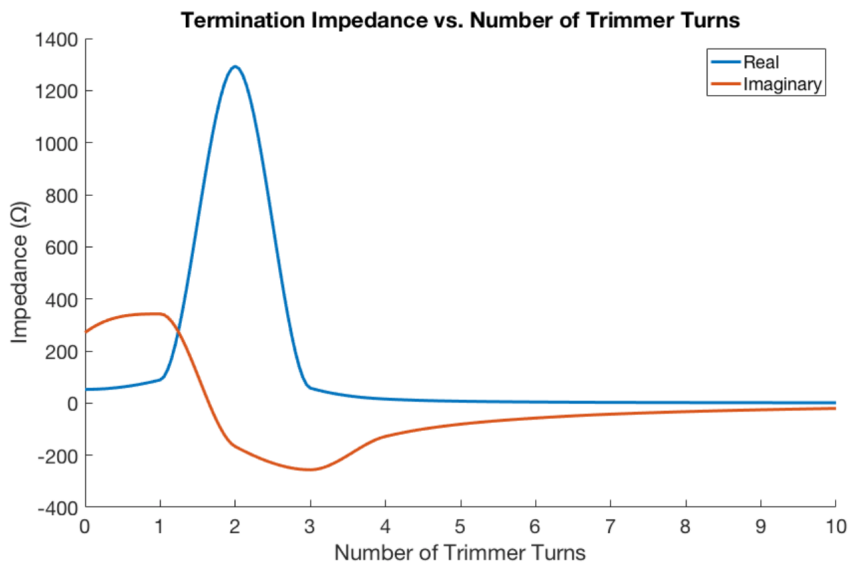

(a)

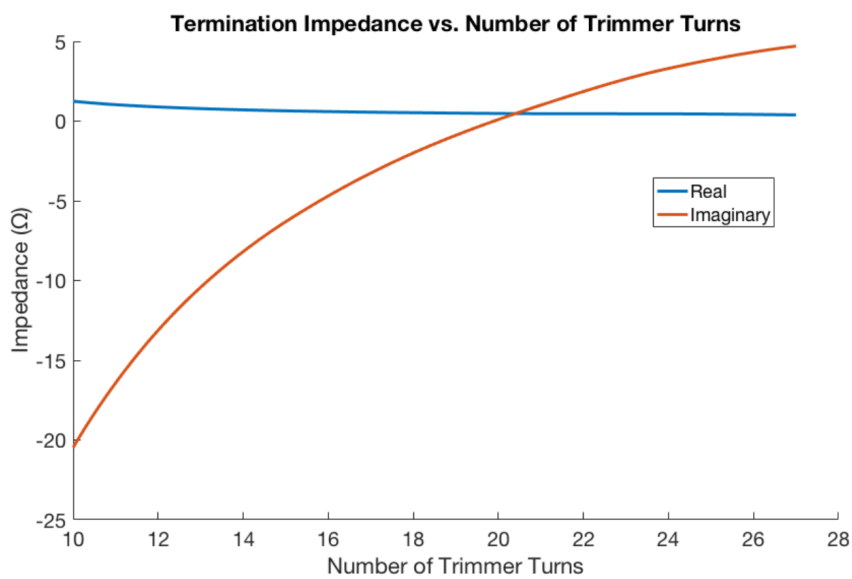

(b)

Fig. 7.13: (a) Termination impedance as a function of first 10 trimmer turns and (b) termination impedance as a function of trimmer turns 10 through 27.

In the next sub-section, the impedance-matching design procedure will be discussed.

7.6.5 Twin-Lead Impedance Matching

In order to determine the necessary impedance matching, the receiver needs to be coupled to the transmitter in a use-case scenario. To do this, the 20cm separation twin-lead transmitter was

constructed using bare copper 14 AWG wire with SMA connectors applied to the ends. The transmitter was then affixed to platforms to elevate it above a flat table. The receiver was also given its own platform and positioned 2.5 cm below the wire plane at the center of the line. The input impedance at 225 MHz was then measured while the receiver was terminated with a 50 Ω resistance and while the termination impedance was minimized. From this, it was found that this impedance (which will be shown in the next section) is well matched when connected to a series capacitor shunt inductor LC network. This network is shown below with KEMET chip capacitors and a CoilCraft inductor, the values of which will be given for each zone mode in proceeding sections.

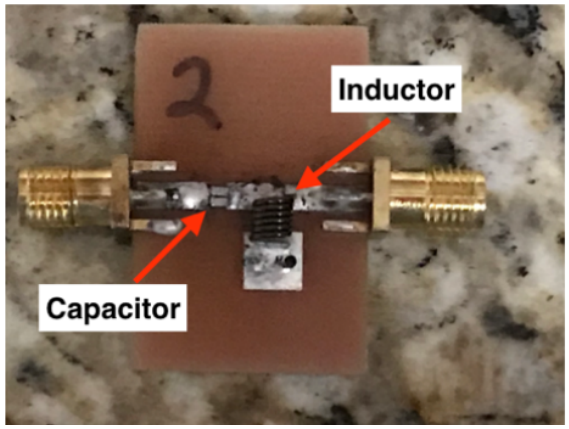

Fig. 7.14: Impedance-matching circuit topology.

Each alternative mode will be sustained by switching out the series capacitor value while keeping the inductance the same. A more detailed explanation of the impedance measurement procedure will be given in the section below. In the next section, the testing and experimental results of the twin-lead WPT system will be presented.

7.7 Twin-Lead WPT System Prototype and Experimental Results

Again, the mid-zone is taken as the base case mode of operation, so it will be analyzed first. First, the RF efficiency of the system (i.e., the S21 from the transmitter impedance-matching network to the receiver output) was measured at 225 MHz under several conditions. Namely, while the receiver was placed in the mid-zone, receiver rotation, vertical displacement, and hori-

zontal displacement were varied to deduce their effects on the system. The figures below describe the measurement setup as well the parameter variation.

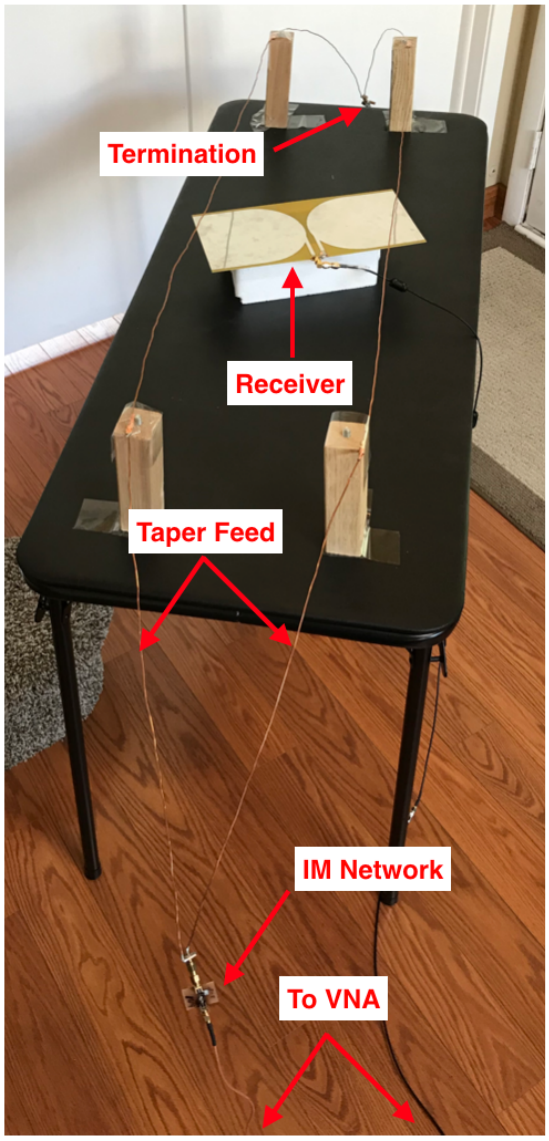

(a)

Fig. 7.15: (a) Twin-lead WPT measurement setup and (b) alternate setup view.

Fig. 7.15 continued

(b)

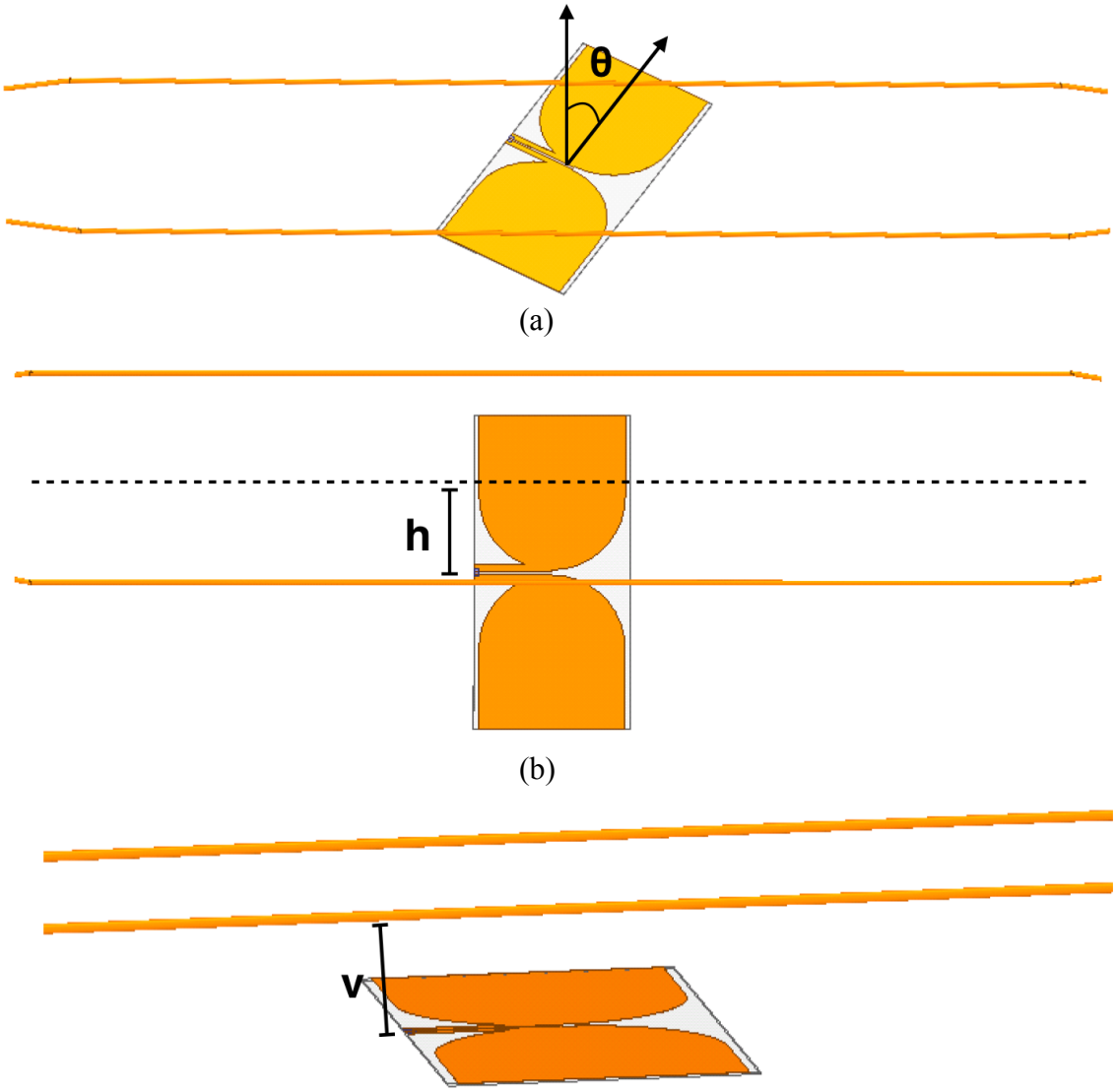

(a)

(b)

(c)

Fig. 7.16: (a) Twin-lead receiver rotation visualization, (b) horizontal displacement visualization, and (c) vertical displacement visualization.

To test the effects of these variations, one parameters was varied while the others were kept static at their optimum values. In the figure below, the RF efficiency as a function of each individual parameter is shown for a receiver located in the mid zone of the transmission line.

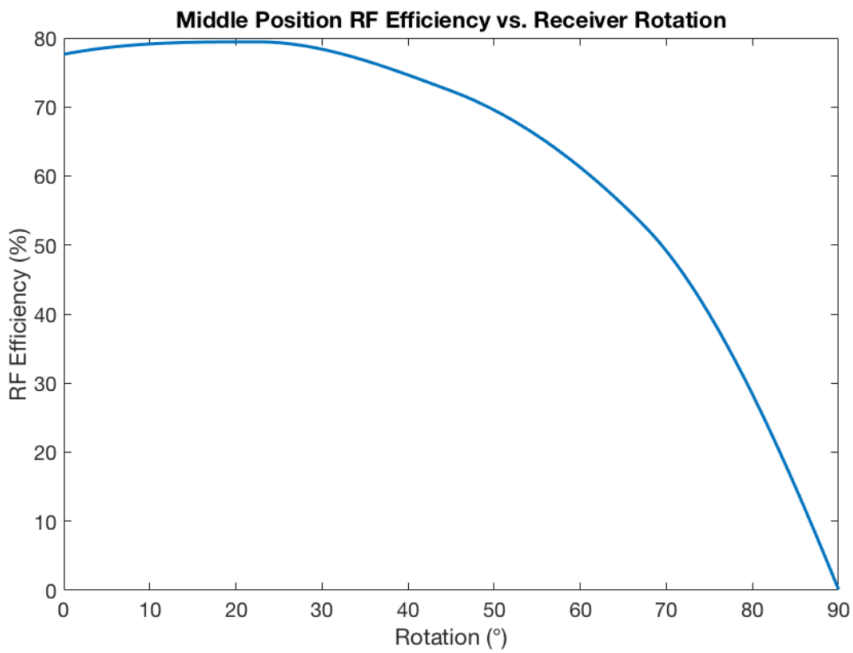

(a)

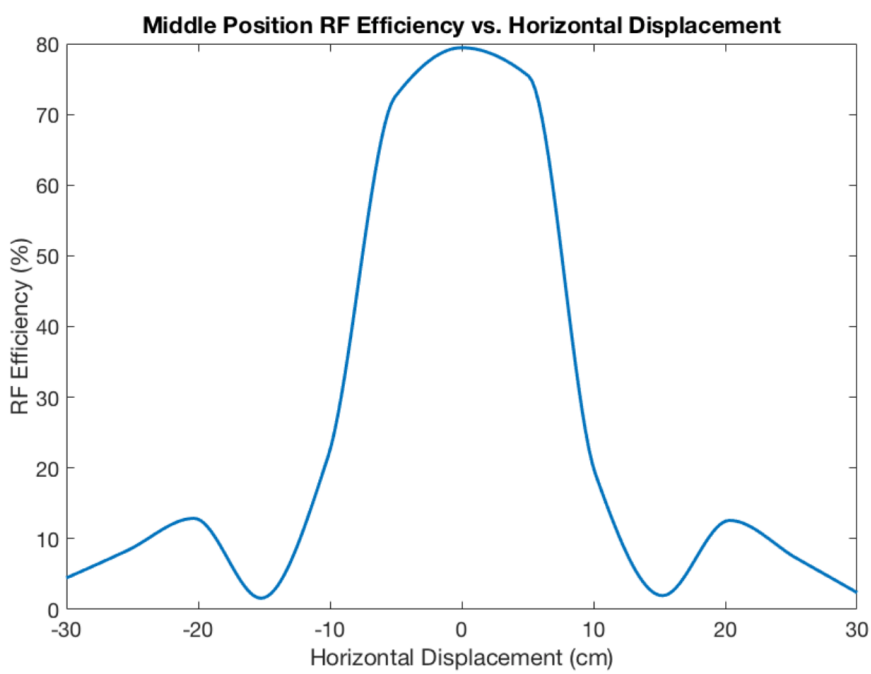

(b)

Fig. 7.17: (a) Twin-lead receiver rotation data, (b) horizontal displacement data and (c) vertical displacement data.

Fig. 7.17 continued

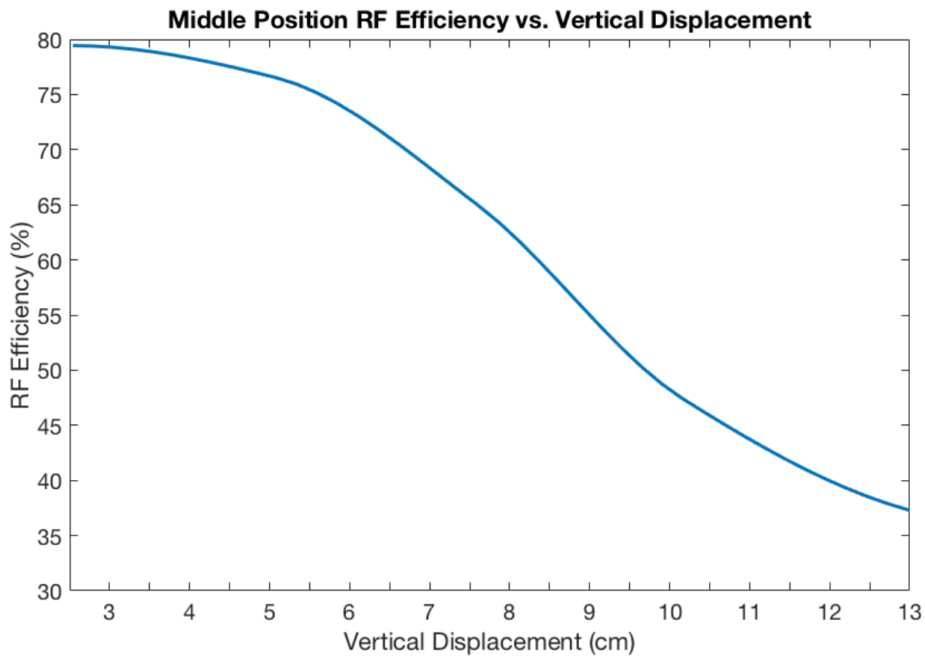

(c)

After this, experiments were conducted to characterize the system tunability under the constraints laid out in previous sections. To recap, only the capacitive elements of the system were varied. Regarding impedance matching, the procedure that was alluded to in sub-section 7.6.5 was taken. Specifically, the input impedance of the transmitter (with no IM network) was measured for each zone by placing the receiver in the zone and sweeping the termination impedance. Note that for each data-point, the receiver was placed at a vertical distance of 2.5 cm from the line with no horizontal displacement and a rotation of 22.5° (the optimal rotation according to Fig. 7.17a). Below, the input impedance data for each zone is plotted:

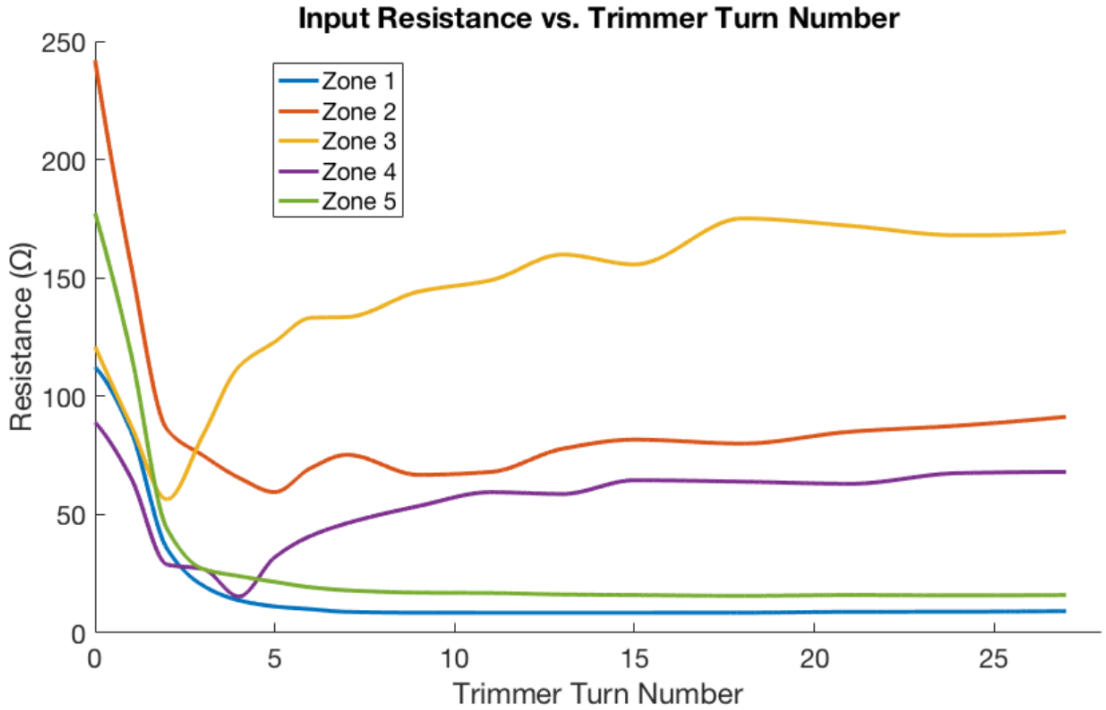

(a)

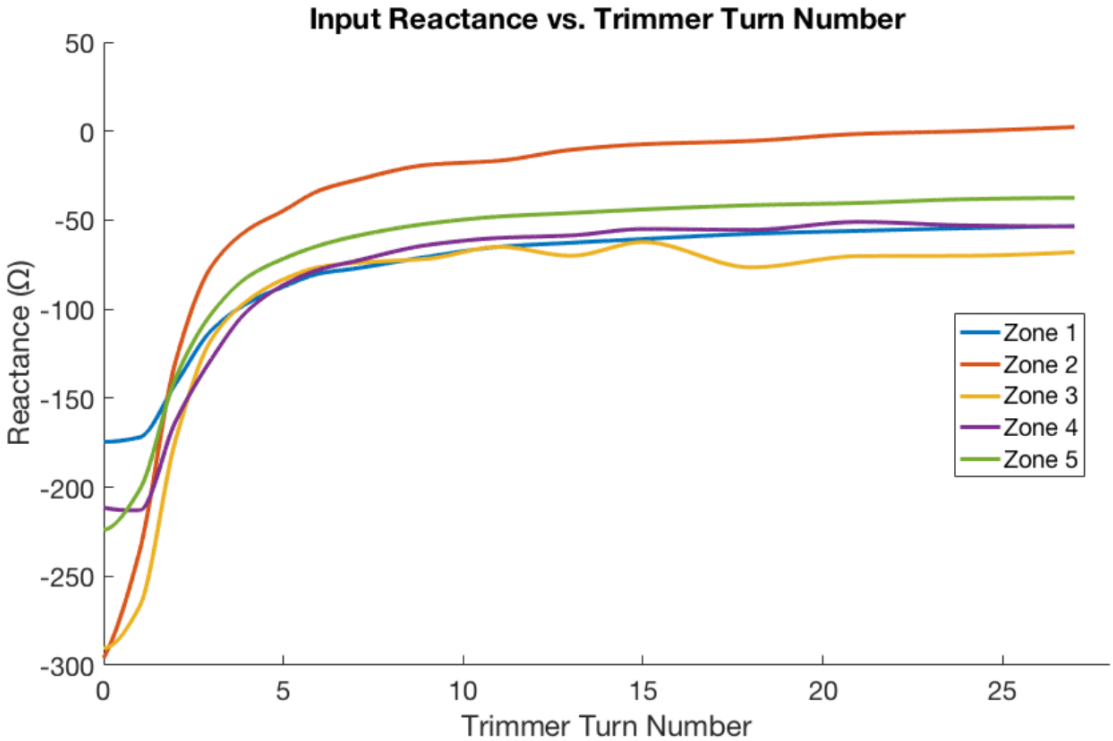

(b)

Fig. 7.18: (a) Twin-lead input resistance vs. trimmer turn number and, (b) input reactance vs. trimmer turn number.

The mid zone impedance-matching network was designed using this data (specifically the data-point where the trimmer turn number is maximized), and the matching for the other zone classes, keeping in mind that the IM circuit topology and inductor were not to be changed, was determined analogously with this empirical data. However, since both the termination (and thus, the wave distribution) and the matching must be compatible for each zone placement, a systematic procedure that was used to determine them needs to be described. The procedure is laid out thusly:

1.) Place the receiver in the desired zone class.

2.) Sweep the termination impedance while noting where an unmatched S21 maximum occurs (note the maximum for, say, zone 1 may be different than the one for zone 5 (both end zones), in which case the "max point" will be the point where the S21 for both is maximized under the condition that they are both about equal).

3.) At this maximum point, check if the input impedance is adequately matchable with the chosen topology and inductor value (with a return loss of < -7 dB).

4.) If yes, choose this matching point for the zone class. If not, vary the termination until the return loss condition can be met.

Using this procedure and the data in Fig. 7.18, the matching and terminations for each mode were determined. The parameters that were used for each mode are listed below:

Table 7.1
Twin-Lead Mode Parameters

Mode	Matching Series Capacitor (pF)	Matching Shunt Inductor (nH)	Termination Impedance (Ω)
Mid	5.95	65	0.387+4.7j
Intermediate	24	65	1.65-27.24j
End	5	65	21+178j

Finally, the RF efficiency as a function of lateral distance along the line was measured for each mode. More specifically, the IM network and termination were set to the desired mode values and the RF efficiency was tracked while moving the receiver from one end of the line to the other. Additionally, for the same termination and IM network, the system was simulated in HFSS and ADS to obtain the same RF efficiency data[1]. The simulated and measured RF efficiency for this experiment are plotted below, as well as a Smith chart showing the variation of the system matching when the termination impedance is swept for differing receiver zone positions and transmitter modes. Specifically, the Smith chart depicts the matching condition of each mode's matching network. It was generated by placing the receiver in one of the zones, applying the matching network that corresponds to that zone, and sweeping the termination impedance to create an impedance curve.

[1] There was a shunt 34.6 nH inductor and series 13.87 pF capacitor included in the simulation to compensate for receiver impedance differences in a free-space simulation with no connectors. This compensation network was determined empirically.

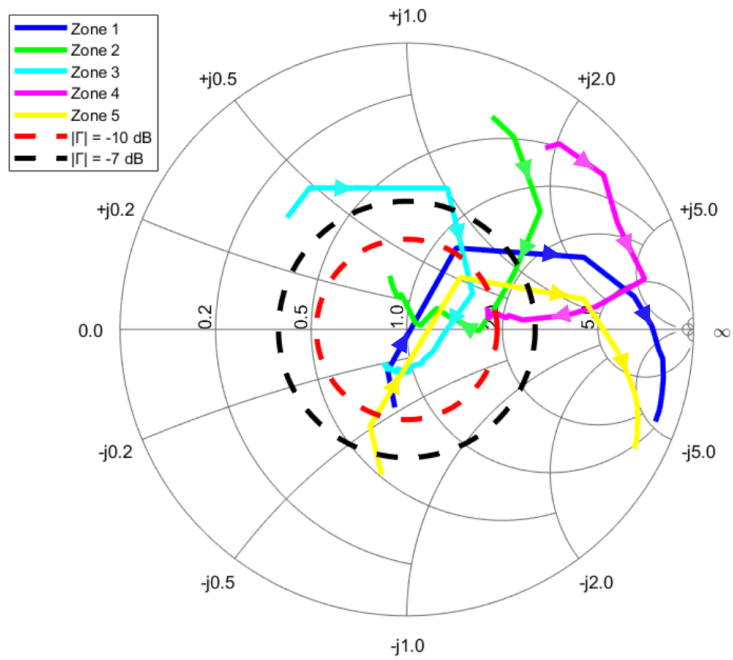

Fig. 7.19: Smith chart impedance curves showing the matching conditions for each mode. Note that the arrows on each curve indicate the direction of increasing trimmer turn number.

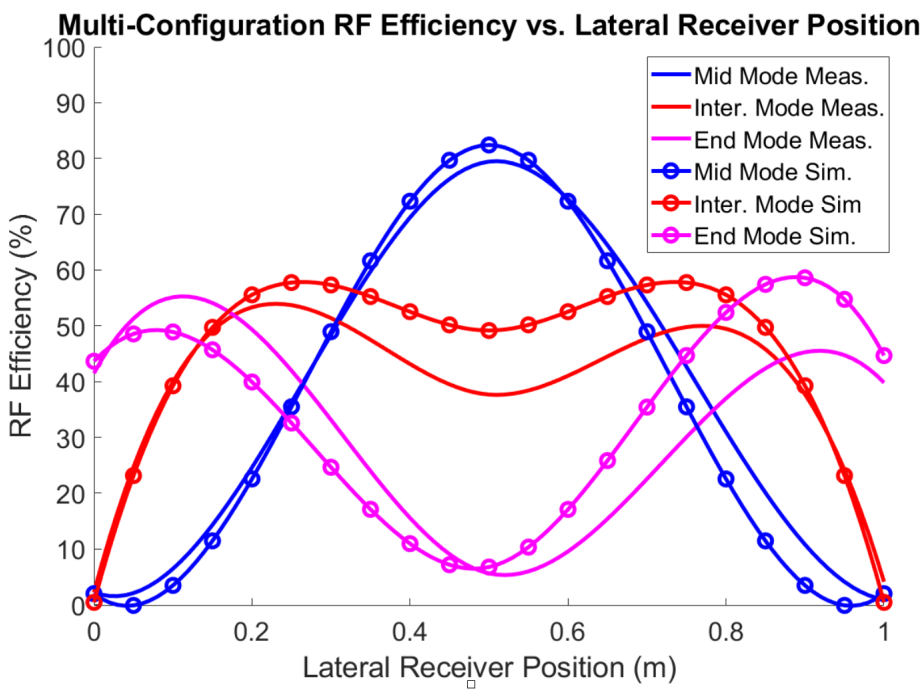

Fig. 7.20: Twin-lead RF efficiency as a function of lateral position for each mode. Note that the 0 m position is at the end of the feed taper from left to right and the 1 m position is at the start of the termination taper from left to right.

In the next section, the results presented above will be discussed in more detail.

7.8 Results Discussion

Fig. 7.17a indicates, perhaps surprisingly, that the optimal rotation of the receiver is not 0°, but 22.5°. The difference in efficiency between these two angles is not particularly large, bit it is notable. The reason behind this effect is likely that some lateral phase difference in the current excitation on each arm of the receiver surface increases coupling to an extent. This effect is quickly overtaken by the cross-polarization effect as the receiver is rotated further, however, as shown by the drop-off in efficiency that begins once 30° has been exceeded.

The vertical displacement data shown in Fig. 7.17c shows that approximately 9.5cm of vertical distance results in an RF efficiency that is half the max value observed for this wire separation (i.e. 9.5 cm is the 3 dB vertical distance). While this distance is less than a tenth of a wavelength, since the applications of the twin-lead power rail do not require much vertical range, this performance is more that adequate. As discussed above, this range can be increased by widening the wire gap, but this results in a radiation loss trade-off. Alternatively, the frequency can be lowered and the system can be scaled accordingly. For instance, the ground clearance for many conventional automobiles is 4-7” or 10-17.5 cm. Taking the highest clearance in that range, the system could be scaled to 120 MHz in order to make the 3 dB vertical distance 17.5 cm without compromising loss. This is not prohibitive.

The data in Fig. 7.17b is consistent with the data in Fig. 7.2, which shows field nulls and polarization reversals along the x-axis. All in all there is some horizontal displacement freedom in the receiver position, but the efficiency fall off is steep after a 6 cm shift is exceeded. This is due to destructive interference of the receiver arm currents. At approximately 15 cm of displacement, the fields being coupled to each arm are 180° out of phase, which creates a coupling null. This indicates that the receiver should be as centered as possible during operation.

Fig. 7.20 indicates that a high degree of tunability has been achieved. With mode switching, the RF efficiency at every point along the line is higher than 40% for each zone target and symmetry about the line center was obtained. This was also done while maintaining a < -7dB return loss while the receiver was placed in the zones that corresponded to the operation mode. This data also shows the route to performance improvement for future iterations of the technology. If the termination and impedance-matching network constraints are lifted or relaxed to accommo-

date more receiver positions, higher efficiencies in the outer zones may be achieved. Nevertheless, the work presented here is foundational for the inclusion of field distribution tuning in open-line WPT.

7.9 Receiver Size Study

The receiver used in the experiments above, as mentioned, had the same dimensions as the receiver used in Chapter 5. It can be seen, however, that the length of this receiver, 30 cm, is larger than the separation distance between the wires of the twin-lead transmitter designed for the study. It is important to determine both if this length is necessary and how large the receiver length must be in order to achieve high RF efficiencies. This section will explore the effects of the dipole receiver length more fully.

Designing the receiver to be large or small presents tradeoffs regarding impedance matching, profile, and coupling. To illustrate this, a brief, free-space simulation study will be conducted using HFSS. Consider the twin-lead 20 cm wire separation WPT system case detailed in Section VI wherein the receiver was placed in the center of the line at the mid-zone lateral distance of 0.5m from the feed (see Fig. 20a). Let the rotation of the line be 0°, the horizontal displacement be 0, and the vertical displacement be 2.5cm (see Fig. 17). Note from Fig. 10 that the length of the receiver used in this work is 30 cm. In this study, for this receiver position, we will sweep the receiver length l_w between 5cm and 30cm while keeping the 15cm width the same. We will then plot the resultant optimal RF efficiency obtainable for both two-sided and one-sided matching conditions. For the two-sided case, two lossless, optimal impedance-matching networks will be applied at both the feed and receiver terminals. For the one-sided case, only the feed will have a matching network and the receiver will be terminated with a 50 Ω load only. The impedance-matching networks were computed using the same MATLAB optimization methods discussed in [18]. Below, the maximum RF efficiency as a function of receiver length for both matching cases is depicted. Note that the receiver length scale is given relative the wire separation, d, which again, is 20cm here:

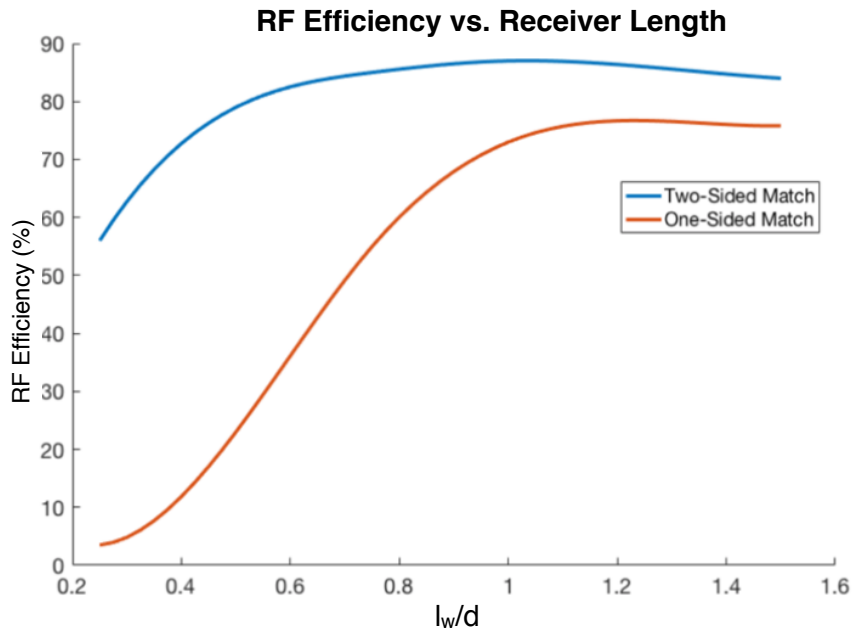

Fig. 7.21 Simulated optimal mid-zone RF efficiency as a function of dipole receiver length.

As Fig. 22 indicates, the dipole receiver length need not exceed the wire separation distance in order to extract the best possible RF efficiency. In fact, the plot above demonstrates diminishing returns when the receiver length is extended beyond the wire separation, as this results in the RF efficiency decreasing slightly for both the one-sided and two-sided matching cases. As expected, since the matching networks in this study are lossless, the RF efficiency is higher when two matching networks are used. However, the efficiency difference decreases significantly when the receiver length, and thus the coupling strength, is increased, confirming the claims of Section III. With this, it is easy to see that, if network losses are incorporated, the one-sided matching can close the efficiency gap between the two matching cases. However, if the receiver is small, the two-sided match is vastly superior. This is because of both lower coupling and a higher receiver reactance due to its smaller electrical length. The latter effect exacerbates the impedance mis-match and necessitates a second network.

The primary takeaway of this study is that, while a smaller receiver does result in a smaller RF efficiency, high efficiencies can be obtained using receivers that are shorter than the wire

separation distance whether one or two-sided matches are used. This demonstrates a high degree of receiver profile flexibility for the system, increasing its application value.

7.10 Conclusions

In this chapter, the concept of a twin-lead transmission line WPT transmitter was introduced and dissected. The design considerations for a system based on the twin-lead line were laid out, culminating in the implementation of a twin-lead WPT system, which was evaluated. Additionally, the work in this chapter introduced the concept of field distribution tuning in open-line WPT designs and linked this idea to the use of twin-lead lines in power rail applications for powering vehicles while they are in motion. Future work will expand on this concept to include feedback systems so the distribution can follow the receiver regardless of lateral position along the line. Even so, the proof-of principle work has been completed.

8. FUTURE WORK AND THESIS SUMMARY

While the work presented thus far has established a solid foundation for OWL WPT system design and implementation, there is still a great deal of work to be done before the technology can become widespread. This chapter will outline the most important set of next steps to be taken in the pursuit of the OWL technology's development. These steps primarily focus on the extension of the technology's applicability by circumventing current shortcomings. Additionally, outlines of future design iterations will be given. Details are given in the sections below, and following that, the contributions of the work presented herein will be given.

8.1 GLine Room Integration

The implementations of the GLine system in previous chapters were standalone in that they were placed in the center of the rooms where testing was conducted and the upper and lower launchers were elevated above the floor and placed below the ceiling respectively. However, use of the GLine WPT system in real-world applications would involve embedding the launchers within the floor and ceiling so that they are not invasive. Further, the study in Section 6 of chapter 5 shows that the launcher discs need not be solid. Therefore, a next step in the development of the GLine will be to integrate the launcher structures within the room that the transmitter is placed in and replace the solid disc launchers with a wire mesh variant. Doing both of these things will be significant in moving the GLine WPT system to a readily usable state.

8.2 Feedback Circuit Control

The system presented in Chapter 7 required different circuitry for each mode setting. Changing the circuitry was done manually in this work, but this is not practical for a full real-world implementation. Therefore, some type of feedback control will be required in order to change the circuitry wirelessly and autonomously according to the receiver position along the line. There is a precedent for how this would be done, as can be found in [56]. The primary difference between that system and a future OWL WPT system that the feedback would require a low-power wire-

less transceiver and an impedance lookup-table, but otherwise, the idea is the same. This is certainly a necessity if vehicles are to be charged using such a system, as manual control will be impossible and impractical in this application.

8.3 Full Device Charging

The rectification results of Chapter 5 demonstrated that usable DC power can be extracted from the GLine for wearable and IoT applications. This conclusion can be extrapolated as well to the twin-lead line since the RF efficiencies for those experiments were higher in general. As such, a critical next step for the technology will involve using such systems to power a complete device. This will show the OWL WPT systems' applicability for real-world applications and move them toward commercial development.

8.4 Environmental Considerations

While touched upon, the effects of the surrounding environment on OWL systems has not be fully investigated. It is known that the surrounding environmental effects are not negligible, however, so a systematic study of these effects must be conducted, especially if these systems are to be integrated into existing structures and unpredictable locations. Specifically, the effect of walls is critical to the GLine if a potential implementation involves the center conductor being embedded into the corner of a room as shown in Fig. 4.3. For the twin-lead line, regarding car-charging applications, simply placing the twin-lead wires on the ground will likely not result in acceptable performance. Therefore, a suitable material environment must be determined in order to realize car-charging applications.

8.5 Summary of Contributions

The original contributions of this work are laid out as follows:

Chapter 2: Open-Wire Line Circuit Theory

- An OWL WPT equivalent transmission line circuit model was developed for both electric and magnetic coupling.
- The Z-parameters and power efficiency of the circuit were solved for both cases.
- Impedance-matching methods were discussed for maximum power transfer.
- An efficiency study was conducted to create a baseline for one-sided vs. two-sided matching.

Chapter 3: GLine Distribution Updated Theory

- An updated GLine mode solution was presented that replaces the previous graphical method for determining GLine mode parameters.
- The ohmic current dynamics of the GLine mode were developed.
- The zero-radiation condition of the GLine mode was mathematically proven.
- The effective capacitance and inductance per unit meter were conceptualized, solved, and verified, along with the GLine's effective TEM characteristic impedance.

Chapter 4: GLine WPT Prototype #1

- The first ever GLine WPT system was designed, constructed, and measured.
- A 10% RF efficiency at 0.5m from the center conductor was achieved.

Chapter 5: GLine WPT Prototype #2

- An updated, reduced-size GLine WPT transmitter was constructed.
- An improved receiver was created that extracted a 35% RF efficiency from the system at 0.5m from the transmitter center.
- A rectifier was applied to the system that resulted in a 25% total efficiency at 0.5m from the transmitter center.
- Multi-receiver and receiver rotation experiments were conducted to verify design flexibility.

Chapter 6: Metamaterial-Based Miniaturized Loop GLine Receiver

- The EZ Antenna concept was used to design electrically-small metamaterial VHF loop antennas that are intrinsically-matched and tunable using lumped-elements.
- These loops were tested as GLine receivers both by themselves and while affixed to the arm of a test subject in order to show their viability in wearable energy-harvesting applications.

Chapter 7: Twin-Lead Line WPT System

- The loss of wide-separation twin-lead lines were defined beyond the results of the quasi-static approximation by using a Hertzian Aggregation simulation method.
- The radiation loss resulting from twin-lead linear taper feeds was quantified.
- A twin-lead line WPT transmitter with reconfigurable standing-wave distribution and impedance matching was constructed and tested, yielding RF efficiencies between 40-80% across the coupling surface of the system.

8.6 Conclusions

In this chapter, the contributions of this work and the future directions of the OWL WPT field have been laid out. The future directions include integrating the GLine into a room, applying a feedback circuit control system to tune transmitter circuitry autonomously, charging a full device, and investigating environmental effects more closely. With these directions in mind, the future potential of OWL WPT is clear.

This concludes the foundational work in OWL WPT. It is the hope of the author that this dissertation has been informative.

LIST OF REFERENCES

[1] A. M. Jawad, R. Nordin, S. K. Gharghan, H. M. Jawad, and M. Ismail, “Opportunities and Challenges for Near-Field Wireless Power Transfer: A Review,” *Energies*, vol. 10, no. 7, p. 1022, 2017.

[2] G. A. Covic and J. T. Boys, "Inductive Power Transfer," in *Proceedings of the IEEE*, vol. 101, no. 6, pp. 1276-1289, June 2013.

[3] Z. Zhang, H. Pang, A. Georgiadis and C. Cecati, "Wireless Power Transfer—An Overview," in *IEEE Transactions on Industrial Electronics*, vol. 66, no. 2, pp. 1044-1058, Feb. 2019.

[4] N. Garraud, D. Alabi, S. Chyczewski, J. D. Varela, D. P. Arnold, and A. Garraud, “Extending the Range of Wireless Power Transmission for Bio-Implants and Wearables,” *Journal of Physics: Conference Series*, vol. 1052, p. 012023, 2018.

[5] A. Gercikow, A. Fuchs, and H.-P. Schmidt, “Wireless Power and Data Transfer for Electric Vehicle Charging at Car Parks,” *2016 IEEE 2nd Annual Southern Power Electronics Conference (SPEC)*, 2016.

[6] A. Costanzo and D. Masotti, “Energizing 5G,” *IEEE Microwave Magazine*, IEEE, 07-Apr-2017.

[7] A. Costanzo, M. Dionigi, D. Masotti, M. Mongiardo, G. Monti, L. Tarricone, and R. Sorrentino, “Electromagnetic Energy Harvesting and Wireless Power Transmission: A Unified Approach,” *Proceedings of the IEEE*, vol. 102, no. 11, pp. 1692–1711, 2014.

[8] Q. Xu, H. Wang, Z. Gao, Z.-H. Mao, J. He, and M. Sun, “A Novel Mat-Based System for Position-Varying Wireless Power Transfer to Biomedical Implants,” *IEEE Transactions on Magnetics*, vol. 49, no. 8, pp. 4774–4779, 2013.

[9] T. Campi, S. Cruciani, F. Palandrani, V. D. Santis, A. Hirata, and M. Feliziani, “Wireless Power Transfer Charging System for AIMDs and Pacemakers,” *IEEE Transactions on Microwave Theory and Techniques*, vol. 64, no. 2, pp. 633–642, 2016.

[10] N. Tesla, U.S. patent 1,119,732 (1914).

[11] W. C. Brown, “The History of Power Transmission by Radio Waves”, *IEEE Transactions on Micorwave Theory and Techniques*, vol. 32, no. 9, pp. 1230-1242, Sep. 1984.

[12] A. Kurs, A. Karalis, R. Moffatt, J.D. Joannopoulos, P. Fisher, and M. Soljacic, “Wireless Power Transfer via Strongly Coupled Magnetic Resonances,” *Science*, vol. 317, no. 5834, pp. 83-86, 2007.

[13] Wei, X.,Wang, Z., and Dai, H., “A Critical Review of Wireless Power Transfer via Strongly Coupled Magnetic Resonances,” *Energies* 2014, 7, 4316-4341.

[14] X. Lu, P. Wang, D. Niyato, D. I. Kim and Z. Han, "Wireless Charging Technologies: Fundamentals, Standards, and Network Applications," in IEEE Communications Surveys & Tutorials, vol. 18, no. 2, pp. 1413-1452, Secondquarter 2016.

[15] Z. Popović, E. A. Falkenstein, D. Costinett and R. Zane, "Low-Power Far-Field Wireless Powering for Wireless Sensors," in Proceedings of the IEEE, vol. 101, no. 6, pp. 1397-1409, June 2013.

[16] R. M. Dickinson, "Performance of a High-Power, 2.388-GHz Receiving Array in Wireless Power Transmission Over 1.54 km," 1976 IEEE-MTT-S International Microwave Symposium, Cherry Hill, NJ, USA, 1976, pp. 139-141.

[17] M. Xia and S. Aissa, "On the Efficiency of Far-Field Wireless Power Transfer," in *IEEE Transactions on Signal Processing*, vol. 63, no. 11, pp. 2835-2847, June, 2015.

[18] A. Sommerfield, “Ueber die Fortpflanzung Elektrodynamischer Wellen Längs eines Drahtes,” *Ann. Phys.*, vol. 303, issue 2, pp. 233-290, 1899.

[19] G. Goubau, “Surface Waves and Their Application to Transmission Lines,” *Journal of Applied Physics,* vol. 21, issue 11, pp. 1119-1128, 1950.

[20] S. J. Orfanidis, “Transmission Lines,” *Electromagnetic Waves and Antennas*, New Brunswick, New Jersey: Rutgers University, 2016, pp. 551-553.

[21] J.-S. Hong, Microstrip filters for RF/microwave applications. Hoboken, NJ: Wiley, 2011.

[22] D. M. Pozar, *Microwave engineering*. Hoboken, NJ: John Wiley & Sons, Inc., 2012.

[23] S. Roberts, “Conjugate-Image Impedances,” Proceedings of the IRE, vol. 34, no. 4, 1946.

[24] D. Frickey, “Conversions Between S, Z, Y, H, ABCD, and T Parameters Which Are Valid for Complex Source and Load Impedances,” IEEE Transactions on Microwave Theory and Techniques, vol. 42, no. 2, pp. 205–211, 1994.

[25] R. M. Corless G. H. Gonnet D. E. G. Hare D. J. Jeffrey D. E. Knuth, “On the Lambert W Function,” Advances in Computational Mathematics, vol. 5, issue 1, pp. 329-359, 1996.

[26] C. Carathéodory, Theory of functions of a complex variable. Rhode Island: AMS Chelsea Pub., 2001.

[27] D. K. Cheng, Field and wave electromagnetics. Essex, CM.: Pearson, 2014.

[28] B. Vaughn, D. Peroulis, and A. Fisher, “Mid-Range Wireless Power Transfer Based on Goubau Lines,” presented at The International Microwave Symposium, Philedelphia, PA, USA, 2018.

[29] G. Elmore.“Introduction to the Propagating Wave on a Single Conductor.,” Corridor Systems Inc., Jul. 27, 2009.

[30] J. S. Besnoff and M. S. Reynolds, "Single-Wire RF Transmission Lines for Implanted Devices," 2013 IEEE Biomedical Circuits and Systems Conference (BioCAS), Rotterdam, 2013, pp. 222-225.

[31] B. Vaughn, A. Fisher, and D. Peroulis, “Electrically-Coupled Goubau-Line-Based Wireless Power Transfer System,” *IEEE Access*, vol. 7, Aug. 2019.

[32] A. Fisher and D. Peroulis, “Efficient Rectifier for Wireless Power Transfer in the VHF Band,” presented at The IEEE Wireless and Microwave Technology Conference, Sand Key, FL, USA, 2018.

[33] "SAR Measurement Requirements for 100 MHz to 6 GHz," Federal Communications Commission Office of Engineering and Technology Laboratory Division, 865664 D01 v01r04, Aug. 2015. [Online]. Available: https://apps.fcc.gov/kdb/GetAttachment.html?id=RUMcMDL7fmDLsdRSsbCNoA%3D%3D&desc=865664%20D01%20SAR%20Measurement%20100%20MHz%20to%206%20GHz%20v01r04&tracking_number=28242 [Accessed: 29 Jan. 2019].

[34] S. Mao, K. Song, C. Zhu, G. Wei, and J. Zhang, “Wireless Power Transfer using a Field-Enhancing Coil and a Small-Sized Receiver with Low Coupling Coefficient,” *IET Power Electronics*, vol. 9, no. 7, pp. 1546–1552, 2016.

[35] W. Lin and R. W. Ziolkowski, “Electrically Small Huygens Antenna-Based Fully-Integrated Wireless Power Transfer and Communication System,” *IEEE Access*, vol. 7, pp. 39762–39769, 2019.

[36] J. L. Gomez-Tornero, M. Poveda-Garcia, R. Guzman-Quiros, and J. C. Sanchez-Arnause, “Design of Ku-band Wireless Power Transfer System to Empower Light Drones,” 2016 IEEE Wireless Power Transfer Conference (WPTC), 2016.

[37] A. Erentok and R. W. Ziolkowski, "Metamaterial-Inspired Efficient Electrically Small Antennas," in IEEE Transactions on Antennas and Propagation, vol. 56, no. 3, pp. 691-707, March 2008.

[38] J. Wen et al., "Planar Electrically Emall Folded Dipole Antenna," 2016 IEEE International Workshop on Electromagnetics: Applications and Student Innovation Competition (iWEM), Nanjing, 2016, pp. 1-3.

[39] G. Bertin, B. Piovano, R. Vallauri, F. Bilotti and L. Vegni, "Metamaterial-Inspired Antennas for Telecommunication Applications," 2012 6th European Conference on Antennas and Propagation (EUCAP), Prague, 2012, pp. 2739-2740.

[40] L. Li, H. Liu, H. Zhang and W. Xue, "Efficient Wireless Power Transfer System Integrating With Metasurface for Biological Applications," in IEEE Transactions on Industrial Electronics, vol. 65, no. 4, pp. 3230-3239, April 2018.

[41] Y. Song, X. Sun, H. Wang, W. Dong, and Y. Ji, “Design of Charging Coil for Unmanned Aerial Vehicle-Enabled Wireless Power Transfer,” 2018 8th International Conference on Power and Energy Systems (ICPES), 2018.

[42] T. M. Mostafa, A. Muharam, and R. Hattori, “Wireless Battery Charging System for Drones via Capacitive Power Transfer,” 2017 IEEE PELS Workshop on Emerging Technologies: Wireless Power Transfer (WoW), 2017.

[43] Z. Li, C. Zhu, J. Jiang, K. Song, and G. Wei, “A 3-kW Wireless Power Transfer System for Sightseeing Car Supercapacitor Charge,” IEEE Transactions on Power Electronics, vol. 32, no. 5, pp. 3301–3316, 2017.

[44] Z. Chen, W. Jing, X. Huang, L. Tan, C. Chen, and W. Wang, “A Promoted Design for Primary Coil in Roadway-Powered System,” IEEE Transactions on Magnetics, vol. 51, no. 11, pp. 1–4, 2015.

[45] D. Vincent, P. S. Huynh, L. Patnaik, and S. S. Williamson, “Prospects of Capacitive Wireless Power Transfer (C-WPT) for Unmanned Aerial Vehicles,” 2018 IEEE PELS Workshop on Emerging Technologies: Wireless Power Transfer (Wow), 2018.

[46] M. Lu, M. Bagheri, A. P. James, and T. Phung, “Wireless Charging Techniques for UAVs: A Review, Reconceptualization, and Extension,” IEEE Access, vol. 6, pp. 29865–29884, 2018.

[47] Y. Nagatsuka, N. Ehara, Y. Kaneko, S. Abe, and T. Yasuda, “Compact Contactless Power Transfer System for Electric Vehicles,” The 2010 International Power Electronics Conference - ECCE ASIA -, 2010.

[48] W. Zhang, S.-C. Wong, C. K. Tse, and Q. Chen, “A Study of Sectional Tracks in Roadway Inductive Power Transfer System,” 2011 IEEE Energy Conversion Congress and Exposition, 2011.

[49] G. Elliott, G. Covic, D. Kacprzak, and J. Boys, “A New Concept: Asymmetrical Pick-Ups for Inductively Coupled Power Transfer Monorail Systems,” IEEE Transactions on Magnetics, vol. 42, no. 10, pp. 3389–3391, 2006.

[50] S. Lee, J. Huh, C. Park, N.-S. Choi, G.-H. Cho, and C.-T. Rim, “On-Line Electric Vehicle using inductive power transfer system,” 2010 IEEE Energy Conversion Congress and Exposition, 2010.

[51] W. Zhang, S.-C. Wong, C. K. Tse, and Q. Chen, “An Optimized Track Length in Roadway Inductive Power Transfer Systems,” IEEE Journal of Emerging and Selected Topics in Power Electronics, vol. 2, no. 3, pp. 598–608, 2014.

[52] A. Pacini, A. Costanzo, S. Aldhaher, and P. D. Mitcheson, “Load- and Position-Independent Moving MHz WPT System Based on GaN-Distributed Current Sources,” *IEEE Transactions on Microwave Theory and Techniques*, vol. 65, no. 12, pp. 5367–5376, 2017.

[53] S. Assawaworrarit, X. Yu, and S. Fan, “Robust Wireless Power Transfer using a Nonlinear Parity–Time-Symmetric Circuit,” Nature, vol. 546, no. 7658, pp. 387–390, 2017.

[54] W. L. Stutzman and G. A. Thiele, *Antenna theory and design.* Hoboken, NJ: Wiley, 2013.

[55] C. A. Balanis, *Antenna theory: analysis and design*. Chichester, West Sussex: Wiley Blackwell, 2016.

[56] O. Rostbakken, “Adaptive Feedback Frequency Tuning for Microstrip Patch Antennas,” Ninth International Conference on Antennas and Propagation (ICAP), 1995.

APPENDIX A: MATLAB CODE

I. R_{rad} Iterative Algorithm

%%%%%%%Code that handles twin-lead R_{rad} calculation iteration algorithm

```
close all

f = 226.5E6; %define frequency

lambda = 3E8/f; %wavelength

sep = linspace(.05, 2.65, 20); %array of wire separation distances of interest

a = .0025; %wire radius in meters

u = 1.25664E-6; %permeability of free space

e = 8.854E-12; %permittivity of free space

o = 5.96E7; %conductivity of copper

Rrad_sep_plot = []; %array that holds final Rrad values

for n = 1:20 %loop that obtains Rrad for all sep points

   d = sep(n); %current wire separation

   if n < 2 %guess at initial Rrad depending on current sep point

      Rrad_guess = (8)*d;

   else

      Rrad_guess = 6.5;

   end

   Rrad_guess_save = 0; %variable that stores current guess (after first iteration)
```

```
Rrad_change = Rrad_guess/10; %variable that defines how much the guess will
                                %change per iteration

error_save = 100; %variable to store smallest error

max_error = .1; %raw maximum error

it_num = 1; %iteration number

plus = 0;

minus = 0;

error_save_array = [];

Rrad_save_array = [];

%%%%while loop calls "twin_lead_Rrad_fitness" to compute the error of the current %%%%
%guess, the error of the guess+Rrad_change, and the error of the
%%%%guess-Rrad_change. Depending on which error is the smallest, the code will
%%%%increase or decrease the current guess. If the current guess is optimal, but the     %%%
%margin of error has not been reached, Rrad_change is halved and the process is %%%%repeat-
ed until convergence.

while error_save >= max_error

    if plus == 0 && minus == 0 && it_num == 1

        error_mid = twin_lead_Rrad_fitness(f, d, a, Rrad_guess, u, e, o, it_num+.1, n)

        error_plus = twin_lead_Rrad_fitness(f, d, a, Rrad_guess+Rrad_change, u, e, o, it_num+.
2, n)

        error_minus = twin_lead_Rrad_fitness(f, d, a, Rrad_guess-Rrad_change, u, e, o, it_num+.
3, n)

        error_save = error_mid;

    elseif plus == 0 && minus == 0 && it_num ~= 1

        error_mid = twin_lead_Rrad_fitness(f, d, a, Rrad_guess, u, e, o, it_num+.1, n)
```

```
        error_plus = twin_lead_Rrad_fitness(f, d, a, Rrad_guess+Rrad_change, u, e, o, it_num+.
2, n)

        error_minus = twin_lead_Rrad_fitness(f, d, a, Rrad_guess-Rrad_change, u, e, o, it_num+.
3, n)


    elseif plus == 1

        error_mid = twin_lead_Rrad_fitness(f, d, a, Rrad_guess, u, e, o, it_num+.1, n)

        error_plus = twin_lead_Rrad_fitness(f, d, a, Rrad_guess+Rrad_change, u, e, o, it_num+.
2, n)

    elseif minus == 1

        error_mid = twin_lead_Rrad_fitness(f, d, a, Rrad_guess, u, e, o, it_num+.1, n)

        error_minus = twin_lead_Rrad_fitness(f, d, a, Rrad_guess-Rrad_change, u, e, o, it_num+.
3, n)

    end



    if error_mid <= error_save && error_mid < error_plus && error_mid < error_minus

       error_save = error_mid;

       Rrad_change = Rrad_change/2;

       plus = 0;

       minus = 0;

    elseif error_mid >= error_save && error_mid > error_plus

        error_save = error_plus;

        Rrad_guess = Rrad_guess + Rrad_change;

        plus = 1;
```

```
        minus = 0;
    elseif error_mid >= error_save && error_mid > error_minus
        error_save = error_minus;
        Rrad_guess = Rrad_guess - Rrad_change;
        minus = 1;
        plus = 0;
    end
    error_save_array(it_num) = error_save;
    Rrad_save_array(it_num) = Rrad_guess;
    close all
    figure
    plot(Rrad_save_array, error_save_array)
    drawnow

    it_num = it_num+1;


  end

  Rrad = Rrad_guess
  error = error_save
  Rrad_sep_plot(n) = Rrad_guess
end
```

```
close all

figure

plot(sep./lambda, Rrad_sep_plot) %plot the Rrad data


save twin_lead_Rrad %save the dataset
```

II. R_{rad} Error Computation

%%%%%%Code that calculates the error between the R_{rad} guess and the R_{rad} %%%%%% %value apparent from Poynting's Theorem given that guess.

```
function [Rrad_fit] = twin_lead_Rrad_fitness(f, d, a, Rrad, u, e, o, it_num, n)

lambda = 3E8/f;

eta = 120*pi; %intrinsic impedance of free space

w = 2*pi*f; %radial frequency

k = 2*pi/lambda; %free space wavenumber

L = (u/pi)*(acosh(d/(2*a))); %inductance per unit meter

C = pi*e/(acosh(d/(2*a))); %capacitance per unit meter

Rs = sqrt(pi*f*u/o); %sheet resistance

Ro = (Rs/(pi*a))*(d/sqrt(d^2 - 4*a^2)); %resistance per unit length

gamma = sqrt((j*w*L + Ro + Rrad)*(j*w*C)); %prop constant

phi = 0; %global coordinate system phi

phi_prime = 0; %effective phi from source point

z_prime = -10*lambda; %initial z-position of dipoles

z = 0; %global coordinate system z

phi_step = 2*pi/101; %numerical integration delta phi

z_prime_step = 1/101; z-step between Hertzian dipoles

rho = 2*lambda; %radius of integration cylinder


%Field variables: sum variables will be added to tot variables during numerical
%integration
```

```
sum1Ex = 0;

sum1Ey = 0;

sum1Ez = 0;

sum2Ex = 0;

sum2Ey = 0;

sum2Ez = 0;


sum1Hx = 0;

sum1Hy = 0;

sum1Hz = 0;

sum2Hx = 0;

sum2Hy = 0;

sum2Hz = 0;


Etot1x = 0;

Etot2x = 0;

Etot1y = 0;

Etot2y = 0;

Etot1z = 0;

Etot2z = 0;

Htot1x = 0;
```

```
Htot2x = 0;

Htot1y = 0;

Htot2y = 0;

Htot1z = 0;

Htot2z = 0;


Rrad_cal = 0; %Calculated Rrad value variable

R1 = 0; %distance from positive dipole to observation point

R2 = 0; %distance from negative dipole to observation point

%variables to set the effective quadrant of the observation point relative to the dipoles' %local
coordinate systems

quad1 = 0;

quad2 = 0;

converge = 0; %parameter to determine improper integral convergence

%Hertzian aggregation

while phi <= 2*pi

   while converge == 0

      while phi_prime <= 2*pi

         R1 = sqrt(rho^2 + a^2 - 2*a*rho*cos(phi-phi_prime) + (z_prime)^2 +
d*(a*cos(phi_prime) - rho*cos(phi)) + (d^2)/4); %compute R1 for current z-position

         R2 = sqrt(rho^2 + a^2 - 2*a*rho*cos(phi-phi_prime) + (z_prime)^2 + d*(-
a*cos(phi_prime) + rho*cos(phi)) + (d^2)/4); %compute R2 for current z-position

         %calculate global and local dipole coordinates

         x = rho.*cos(phi);
```

```
y = rho.*sin(phi);

x_prime1 = d/2 + a.*cos(phi_prime);

y_prime1 = 0;

x_prime2 = -d/2 + a.*cos(phi_prime);

y_prime2 = 0;

xcoor1 = x-x_prime1;

ycoor1 = y-y_prime1;

zcoor1 = z-z_prime;

xcoor2 = x-x_prime2;

ycoor2 = y-y_prime2;

zcoor2 = z-z_prime;

%quadrant determination

    if xcoor1 >= 0 && ycoor1 >= 0

        quad1 = 1;

    elseif xcoor1 < 0 && ycoor1 >=0

        quad1 = 2;

    elseif xcoor1 < 0 && ycoor1 < 0

        quad1 = 3;

    else

        quad1 = 4;

    end
```

```
if xcoor2 >= 0 && ycoor2 >= 0
    quad2 = 1;
elseif xcoor2 < 0 && ycoor2 >=0
    quad2 = 2;
elseif xcoor2 < 0 && ycoor2 < 0
    quad2 = 3;
else
    quad2 = 4;
end

%effective unit vector computation
if quad1 == 1 || quad1 == 2
    phi_unit1 = acos((x-x_prime1)./sqrt(R1.^2-(z_prime).^2));
else
    phi_unit1 = -acos((x-x_prime1)./sqrt(R1.^2-(z_prime).^2));
end

if quad2 == 1 || quad2 == 2
    phi_unit2 = acos((x-x_prime2)./sqrt(R2.^2-(z_prime).^2));
else
    phi_unit2 = -acos((x-x_prime2)./sqrt(R2.^2-(z_prime).^2));
```

```
    end
sintheta1 = sqrt(R1^2-z_prime^2)/R1;
sintheta2 = sqrt(R2^2-z_prime^2)/R2;
costheta1 = -z_prime/R1;
costheta2 = -z_prime/R2;

%theta_prime unit vector parameters
x_unit_vecE1 = costheta1*cos(phi_unit1);
x_unit_vecE2 = costheta2*cos(phi_unit2);
y_unit_vecE1 = costheta1*sin(phi_unit1);
y_unit_vecE2 = costheta2*sin(phi_unit2);
z_unit_vecE1 = -sintheta1;
z_unit_vecE2 = -sintheta2;
%phi_prime unit vector parameters
x_unit_vecH1 = -sin(phi_unit1);
y_unit_vecH1 = cos(phi_unit1);
x_unit_vecH2 = -sin(phi_unit2);
y_unit_vecH2 = cos(phi_unit2);



Eo1 = (j*w*u*exp(-j*k*R1)*sintheta1*exp(-gamma*z_prime)/(8*R1*pi^2));
Eo2 = (-j*w*u*exp(-j*k*R2)*sintheta2*exp(-gamma*z_prime)/(8*R2*pi^2));
Ho1 = Eo1/eta;
```

```
Ho2 = Eo2/eta;

%E-field kernals

kernal1x = Eo1*x_unit_vecE1;

kernal2x = Eo2*x_unit_vecE2;

kernal1y = Eo1*y_unit_vecE1;

kernal2y = Eo2*y_unit_vecE2;

kernal1z = Eo1*z_unit_vecE1;

kernal2z = Eo2*z_unit_vecE2;

sum1Ex = sum1Ex + kernal1x*phi_step;

sum2Ex = sum2Ex + kernal2x*phi_step;

sum1Ey = sum1Ey + kernal1y*phi_step;

sum2Ey = sum2Ey + kernal2y*phi_step;

sum1Ez = sum1Ez + kernal1z*phi_step;

sum2Ez = sum2Ez + kernal2z*phi_step;

%H-field kernals

kernal1x = Ho1*x_unit_vecH1;

kernal2x = Ho2*x_unit_vecH2;

kernal1y = Ho1*y_unit_vecH1;

kernal2y = Ho2*y_unit_vecH2;
```

```
    sum1Hx = sum1Hx + kernal1x*phi_step;
    sum2Hx = sum2Hx + kernal2x*phi_step;
    sum1Hy = sum1Hy + kernal1y*phi_step;
    sum2Hy = sum2Hy + kernal2y*phi_step;

    phi_prime = phi_prime + phi_step;
end
%numerical integral summation step
Etot1x = Etot1x + sum1Ex*z_prime_step;
Etot2x = Etot2x + sum2Ex*z_prime_step;
Etot1y = Etot1y + sum1Ey*z_prime_step;
Etot2y = Etot2y + sum2Ey*z_prime_step;
Etot1z = Etot1z + sum1Ez*z_prime_step;
Etot2z = Etot2z + sum2Ez*z_prime_step;

Htot1x = Htot1x + sum1Hx*z_prime_step;
Htot2x = Htot2x + sum2Hx*z_prime_step;
Htot1y = Htot1y + sum1Hy*z_prime_step;
Htot2y = Htot2y + sum2Hy*z_prime_step;
%convergence check
if abs(sum1Ez+sum2Ez) < .1 || z_prime > 100
    if z_prime > 0
```

```
            converge = 1;
        end
    end
   %reset summation variables
    sum1Ex = 0;
    sum1Ey = 0;
    sum1Ez = 0;
    sum2Ex = 0;
    sum2Ey = 0;
    sum2Ez = 0;

    sum1Hx = 0;
    sum1Hy = 0;
    sum2Hx = 0;
    sum2Hy = 0;

    phi_prime = 0;



    z_prime = z_prime + z_prime_step;
end
%add last calculation to current Rrad value to continue the aggregation
```

```
    Rrad_cal = Rrad_cal + (rho)*(real(-(Etot1z+Etot2z)*conj(Htot1y+Htot2y))*cos(phi) +
real((Etot1z+Etot2z)*conj(Htot1x+Htot2x))*sin(phi))*phi_step;

    %reset dipole total field variables

    Etot1x = 0;

    Etot2x = 0;

    Etot1y = 0;

    Etot2y = 0;

    Etot1z = 0;

    Etot2z = 0;


    Htot1x = 0;

    Htot2x = 0;

    Htot1y = 0;

    Htot2y = 0;



    phi = phi + phi_step; %iterate phi

    Completion = 100*phi/(2*pi); %calculate progress

        if abs(round(100*phi/(2*pi)) - 100*phi/(2*pi)) < .5

            clc;

            disp(['Rrad Calculation Completion Percentage: ',num2str(round(100*phi/(2*pi))),'% It-
eration #',num2str(it_num), ', distance point ', num2str(n) ]) %display field
                                                                %computation
                                                            %progress

        end
```

```
    converge = 0;

    z_prime = 0;

    phi_prime = 0;

end


Rrad_fit = abs(Rrad_cal-Rrad); %calculate error output
```

III. Known R_{rad} Field Master Code

%%%%%Code that handles final calculation of twin-lead fields given R_{rad} values

```
load twin_lead_Rrad %load Rrad date

points = size(sep);

points = points(2); %determine number of Rrad points

dist = linspace(.1,lambda,101); %set wire separations corresponding to Rrad values

%field arrays

Ex = zeros(points, 101);

Ey = zeros(points, 101);

Ez = zeros(points, 101);

Hx = zeros(points, 101);

Hy = zeros(points, 101);

%for loop to compute fields for each datapoint

for n = 1:points


  [Ex(n,:), Ey(n,:), Ez(n,:), Hx(n,:), Hy(n,:)] = twin_lead_E(f, sep(n), a, Rrad_sep_plot(n), u, e,
o, dist, n);  %call field calculation function

  Completion = 100*n/(points);

  clc;
          disp(['Field Calculation Completion Percentage: ',num2str(Completion), ' %']) %display
field computation progress



end

save twin_lead_fields %save field data
```

IV. Known R_{rad} Field Computation

%%%%%Code that computes twin-lead fields given R_{rad} is known. Note that this code is almost identical to the Rrad_fitness function

```
function [Ex, Ey, Ez, Hx, Hy] = twin_lead_E(f, d, a, Rrad, u, e, o, dist, n)

lambda = 3E8/f;

eta = 120*pi; %intrinsic impedance of free space

w = 2*pi*f; %radial frequency

k = 2*pi/lambda; %free space wavenumber

L = (u/pi)*(acosh(d/(2*a))); %inductance per unit meter

C = pi*e/(acosh(d/(2*a))); %capacitance per unit meter

Rs = sqrt(pi*f*u/o); %sheet resistance

Ro = (Rs/(pi*a))*(d/sqrt(d^2 - 4*a^2)); %resistance per unit length

gamma = sqrt((j*w*L + Ro + Rrad)*(j*w*C)); %prop constant

phi = 0; %global coordinate system phi

phi_prime = 0; %effective phi from source point

z_prime = -10*lambda; %initial z-position of dipoles

z = 0; %global coordinate system z

phi_step = 2*pi/101; %numerical integration delta phi

z_prime_step = 1/101; z-step between Hertzian dipoles

rho = 2*lambda; %radius of integration cylinder


%Field variables: sum variables will be added to tot variables during numerical
%integration
```

```
sum1Ex = 0;

sum1Ey = 0;

sum1Ez = 0;

sum2Ex = 0;

sum2Ey = 0;

sum2Ez = 0;


sum1Hx = 0;

sum1Hy = 0;

sum1Hz = 0;

sum2Hx = 0;

sum2Hy = 0;

sum2Hz = 0;


Etot1x = 0;

Etot2x = 0;

Etot1y = 0;

Etot2y = 0;

Etot1z = 0;

Etot2z = 0;

Htot1x = 0;
```

```
Htot2x = 0;

Htot1y = 0;

Htot2y = 0;

Htot1z = 0;

Htot2z = 0;


R1 = 0; %distance from positive dipole to observation point

R2 = 0; %distance from negative dipole to observation point

%variables to set the effective quadrant of the observation point relative to the dipoles' %local
coordinate systems

quad1 = 0;

quad2 = 0;

converge = 0; %parameter to determine improper integral convergence

%Hertzian aggregation

while phi <= 2*pi

   while converge == 0

      while phi_prime <= 2*pi

         R1 = sqrt(rho^2 + a^2 - 2*a*rho*cos(phi-phi_prime) + (z_prime)^2 +
d*(a*cos(phi_prime) - rho*cos(phi)) + (d^2)/4); %compute R1 for current z-position

         R2 = sqrt(rho^2 + a^2 - 2*a*rho*cos(phi-phi_prime) + (z_prime)^2 + d*(-
a*cos(phi_prime) + rho*cos(phi)) + (d^2)/4); %compute R2 for current z-position

         %calculate global and local dipole coordinates

         x = rho.*cos(phi);
```

```
y = rho.*sin(phi);

x_prime1 = d/2 + a.*cos(phi_prime);

y_prime1 = 0;

x_prime2 = -d/2 + a.*cos(phi_prime);

y_prime2 = 0;

xcoor1 = x-x_prime1;

ycoor1 = y-y_prime1;

zcoor1 = z-z_prime;

xcoor2 = x-x_prime2;

ycoor2 = y-y_prime2;

zcoor2 = z-z_prime;

%quadrant determination

    if xcoor1 >= 0 && ycoor1 >= 0

        quad1 = 1;

    elseif xcoor1 < 0 && ycoor1 >=0

        quad1 = 2;

    elseif xcoor1 < 0 && ycoor1 < 0

        quad1 = 3;

    else

        quad1 = 4;

    end
```

```
if xcoor2 >= 0 && ycoor2 >= 0
    quad2 = 1;
elseif xcoor2 < 0 && ycoor2 >=0
    quad2 = 2;
elseif xcoor2 < 0 && ycoor2 < 0
    quad2 = 3;
else
    quad2 = 4;
end

%effective unit vector computation
if quad1 == 1 || quad1 == 2
    phi_unit1 = acos((x-x_prime1)./sqrt(R1.^2-(z_prime).^2));
else
    phi_unit1 = -acos((x-x_prime1)./sqrt(R1.^2-(z_prime).^2));
end

if quad2 == 1 || quad2 == 2
    phi_unit2 = acos((x-x_prime2)./sqrt(R2.^2-(z_prime).^2));
else
    phi_unit2 = -acos((x-x_prime2)./sqrt(R2.^2-(z_prime).^2));
end
```

```
sintheta1 = sqrt(R1^2-z_prime^2)/R1;

sintheta2 = sqrt(R2^2-z_prime^2)/R2;

costheta1 = -z_prime/R1;

costheta2 = -z_prime/R2;

%theta_prime unit vector parameters

x_unit_vecE1 = costheta1*cos(phi_unit1);

x_unit_vecE2 = costheta2*cos(phi_unit2);

y_unit_vecE1 = costheta1*sin(phi_unit1);

y_unit_vecE2 = costheta2*sin(phi_unit2);

z_unit_vecE1 = -sintheta1;

z_unit_vecE2 = -sintheta2;

%phi_prime unit vector parameters

x_unit_vecH1 = -sin(phi_unit1);

y_unit_vecH1 = cos(phi_unit1);

x_unit_vecH2 = -sin(phi_unit2);

y_unit_vecH2 = cos(phi_unit2);


Eo1 = (j*w*u*exp(-j*k*R1)*sintheta1*exp(-gamma*z_prime)/(8*R1*pi^2));

Eo2 = (-j*w*u*exp(-j*k*R2)*sintheta2*exp(-gamma*z_prime)/(8*R2*pi^2));

Ho1 = Eo1/eta;
```

```
Ho2 = Eo2/eta;

%E-field kernals

kernal1x = Eo1*x_unit_vecE1;

kernal2x = Eo2*x_unit_vecE2;

kernal1y = Eo1*y_unit_vecE1;

kernal2y = Eo2*y_unit_vecE2;

kernal1z = Eo1*z_unit_vecE1;

kernal2z = Eo2*z_unit_vecE2;

sum1Ex = sum1Ex + kernal1x*phi_step;

sum2Ex = sum2Ex + kernal2x*phi_step;

sum1Ey = sum1Ey + kernal1y*phi_step;

sum2Ey = sum2Ey + kernal2y*phi_step;

sum1Ez = sum1Ez + kernal1z*phi_step;

sum2Ez = sum2Ez + kernal2z*phi_step;

%H-field kernals

kernal1x = Ho1*x_unit_vecH1;

kernal2x = Ho2*x_unit_vecH2;

kernal1y = Ho1*y_unit_vecH1;

kernal2y = Ho2*y_unit_vecH2;

sum1Hx = sum1Hx + kernal1x*phi_step;
```

```
    sum2Hx = sum2Hx + kernal2x*phi_step;
    sum1Hy = sum1Hy + kernal1y*phi_step;
    sum2Hy = sum2Hy + kernal2y*phi_step;

    phi_prime = phi_prime + phi_step;
end
%numerical integral summation step
Etot1x = Etot1x + sum1Ex*z_prime_step;
Etot2x = Etot2x + sum2Ex*z_prime_step;
Etot1y = Etot1y + sum1Ey*z_prime_step;
Etot2y = Etot2y + sum2Ey*z_prime_step;
Etot1z = Etot1z + sum1Ez*z_prime_step;
Etot2z = Etot2z + sum2Ez*z_prime_step;

Htot1x = Htot1x + sum1Hx*z_prime_step;
Htot2x = Htot2x + sum2Hx*z_prime_step;
Htot1y = Htot1y + sum1Hy*z_prime_step;
Htot2y = Htot2y + sum2Hy*z_prime_step;
%convergence check
if abs(sum1Ez+sum2Ez) < .1 || z_prime > 100
    if z_prime > 0
        converge = 1;
```

```
        end
    end
   %reset summation variables
    sum1Ex = 0;
    sum1Ey = 0;
    sum1Ez = 0;
    sum2Ex = 0;
    sum2Ey = 0;
    sum2Ez = 0;

    sum1Hx = 0;
    sum1Hy = 0;
    sum2Hx = 0;
    sum2Hy = 0;

    phi_prime = 0;

    z_prime = z_prime + z_prime_step;
end
%output sum of positive and negative dipole fields
Ex = Etot1x + Etot2x;
Ey = Etot1y + Etot2y;
```

```
    Ez = Etot1z + Etot2z;

    Hx = Htot1x + Htot2x;

    Hy = Htot1y + Htot2y;

end
```